NUMERICAL INVESTIGATION OF SOLITARY WAVE INTERACTION WITH GROUP OF CYLINDERS

by Weihua Mo

NUMERICAL INVESTIGATION OF SOLITARY WAVE INTERACTION WITH GROUP OF CYLINDERS

A Dissertation

Presented to the Faculty of the Graduate School

of Cornell University

in Partial Fulfillment of the Requirements for the Degree of

Doctor of Philosophy

by

Weihua Mo

August 2010

NUMERICAL INVESTIGATION OF SOLITARY WAVE INTERACTION WITH GROUP OF CYLINDERS

Weihua Mo, Ph.D.

Cornell University 2010

A numerical model is developed to solve the three dimensional wave-structure interaction problem. This model is based on the filtered Navier-Stokes equations or Eulers equation for incompressible flow. A two-step projection finite volume scheme is adopted to solve the N-S equations and the free surface movement is tracked by the piecewise linear volume of fluid (VOF) method. The large eddy sub-grid model is used for the turbulence calculation. In the large eddy simulation (LES), the small scale eddies are modeled by the sub-grid scale model, and the large eddies are explicitly solved. Traditional Smagorinsky LES model and RNG LES model are implemented in this study.

The numerical model has been validated by using non-breaking waves. Non-breaking solitary wave or periodic Stokes wave propagating in a constant water depth are numerically simulated. The numerical solutions are compared with the analytical theory or laboratory measurements. The conservative property of the numerical model is also inspected. In general, the numerical model gives satisfactory results for the wave kinematics, such as the free surface displacement, phase speed and fluid velocity.

The numerical model is then used to simulate solitary waves and their interaction with a group of slender vertical piles in a constant water depth. The Eulers equation is numerically solved since the waves are non-breaking. The numerical results are compared with laboratory data in terms of free surface

displacements, fluid particle velocity and wave forces. The relatively less satisfactory agreement is observed in the dynamic pressure on the cylinder, but this could be due to the measurement errors. The complex three-dimensional flow patterns, the velocity and pressure fields are presented and discussed.

Later, the breaking solitary waves on a slanted beach and their interaction with a slender cylinder are studied. The large eddy simulation (LES) is used for the turbulence calculation. The numerical results show reasonably good agreements with the laboratory data. Discussion about the choice of LES subgrid model is also presented.

BIOGRAPHICAL SKETCH

The author was born in a small town in China in October 1977. He received his Bachelor of Science degree and Master of Science in Hydraulic Engineering from Tsinghua University in 2000 and 2003. Then he got a great oppurtunity to enroll in the Graduate School of Civil and Environmental Engineering of Cornell University in 2004 to pursue his Ph.D. degree focusing on the study of Coastal Dynamics and Computational Fluid Mechanics.

To my family.

ACKNOWLEDGEMENTS

I'd first like to express my sincere appreciation to my adviser, Professor Philip L.-F. Liu, for his advice and continued support during this research at Cornell. I am also grateful for his kindness and patience during these years. The thesis would have never been possible without him.

I'd also like to thank the committee members, Professor James T. Jenkins at School of Theoretical and Applied Mechanics and Professor Lance R. Collins at School of Mechanical and Aerospace Engineering, for their assistance, suggestions and helpful comments on my thesis study. I express my special thanks to Professor Zellman Warhaft at School of Mechanical and Aerospace Engineering for his kindness and attendance of my thesis defense.

I extends my special thanks to the researchers from whom the thesis has benefited. The numerical model is modified from Truchas, which is developed by Telluride group at Los Alamos National Laboratories. The experimental data used in this study come from many sources. I would like to thank Professor Hocine Oumeraci and Dr. Kai Irschik at Coastal Research Centre (FZK) of Universty Hannover, Professor Harry Yeh and Dr. In-Mei Sou at Oregon State University, and Professor Atle Jensen at University of Oslo, for their excellent laboratory work.

I am happy to thank my fellow graduate students Drs. Qinghai Zhang, Xiaoming Wang and Tso-Ren Wu for their help in my study and life at Cornell. Special thanks to Dr. Tso-Ren Wu for his helpful assistance in my learning of the numerical model. I also thank all the friendly fluid people who made my stay at Cornell a pleasant time.

Finally, I would like to thank my friends and family for their support and love. I thank my uncle Jinxin Luo and aunt Surong He for their encouragement

to me; I also thank Rong Wu for her support and care. And I express my sincere gratitude to my parents, who have been giving my invaluable support and love in my life. I could not finish my thesis without their kind support.

TABLE OF CONTENTS

LIST OF FIGURES

LIST OF TABLES

CHAPTER 1

INTRODUCTION

1.1 Numerical Study of Wave-Structure Interaction

Over the past few decades, offshore structures, such as oil platforms, offshore wind-power plants, have been in rapid growth in coastal and deep ocean regions, and wave-structure interaction has long been a strong interest in coastal and offshore engineering. A thorough understanding of the interaction of waves with offshore structures is vital in the safe and design of such structures. In addition, the flow field near the structures is helpful to understand the scour, sediment transport process in the coastal regions.

Among the offshore structures, vertical cylinders are one of the most commonly used structures in coastal and offshore engineering. In the nearshore region they are used for jetties or piers and in deepwater for offshore platforms and windmill farms. In designing these structures, it is critical to be able to calculate wave forces acting on each individual cylinder and, in some cases, a group of cylinders. For a slender cylinder, where the diameter of the cylinder (D) is small in comparison with the design wavelength (λ), the Morison formula [52] is a good approximation for calculating the wave forces:

$$F_H = \int_0^{h+\eta} \left(\frac{1}{2} \rho C_D D |u| u \right) dz + \int_0^{h+\eta} \left(\rho C_M V_0 \frac{\partial u}{\partial t} \right) dz \tag{1.1}$$

where C_D and C_M are force coefficients, ρ is the water density, u is the horizontal particle velocity, D is the cylinder size, and V_0 is the water volume occupied by the cylinder. On the other hand, if the diameter of the cylinder or the distance between two adjacent cylinders is not sufficiently small, the presence of

the cylinders will generate significant scattered waves and the wave forces can be accurately calculated only if the interactions between waves and cylinder are fully considered [65].

Information on wave forces can be obtained by means of laboratory experiments or numerical simulations. Even when the Morison formula is employed, the dependency of two coefficients, C_D (drag coefficient) and C_M (mass coefficient), on the design wave conditions and the geometry of the cylinder must be determined based on the experimental data or numerical simulations. Since laboratory experiments are usually constrained by the physical dimensions of laboratory facilities, it is not very often feasible to perform extensive parameter studies (e.g., variation of water depth, diameter and inclination of cylinders, wave parameters, breaker type, and configuration of cylinders in a group) even if the costs are of no concern. The alternative is to use numerical simulations as supplements to laboratory experiments. In other words, a limited numbers of experiments can be designed so that the laboratory data can be effectively used to validate numerical models. The validated numerical models are then used to simulate scenarios with much wider range of physical parameters of interest. Moreover, accurate numerical simulations will also provide much more detailed insights into the physical processes that could not be achieved by experimental approach. Nowadays, with rapid advances in computer power, more researchers and engineers are using numerical simulations to study the wave-structure interactions. In this study, a robust three dimensional Navier-Stokes equation solver will be presented to numerically study the interaction between waves and a group of cylinders.

Modeling the interaction between waves and a group of cylinders faces

many challenges similar to other wave-structure interaction problems. First of all, the flow is a complex three-dimensional free surface flow with moving runup boundaries on the cylinders. For large incident waves, breaking might occur in front of the cylinder and flow separation on the lee side of the cylinder. Therefore, local, but strong, turbulence in the vicinity of the cylinder and near the free surface need to be considered. The numerical implementation of the fully nonlinear free surface condition is also a major difficulty in the numerical simulations.

So far, most of the numerical simulation models developed for three-dimensional wave propagation have been built upon the potential flow theory. Using integral equation methods, highly accurate numerical models have been developed for wave propagation over varying bathymetry in shallow water and for wave-body interaction in deep water [81, 45, 25]. However, the potential flow assumption limits these models applications to irrotational flow.

Alternatively, to consider the rotational flows the three-dimensional Eulers equations or Navier-Stokes (N-S) equations can be employed to describe flow motions. Theoretically, the direct numerical simulation (DNS) can always be performed to resolve the entire spectrum of motions ranging from large eddy motions to the smallest turbulence (Kolmogorov) scale motions. Clearly, the DNS requires very fine spatial and temporal resolutions and most of DNS applications can only be applied to relatively low Reynolds number flows within a small computational domain [30]. With the currently available computing resources, the DNS is still not a feasible approach for investigating wave-body interaction problems if wave breaking and flow separation are important.

The alternatives to the DNS approach for computing the turbulent flow

characteristics include the Reynolds Averaged Navier-Stokes (RANS) equations method and the Large Eddy Simulation (LES) method. In the RANS equations method, only the ensemble-averaged (mean) flow motion is resolved. The turbulence effects appear in the momentum equations for the mean flow and are represented by the Reynolds stresses, which are often modeled by an eddy viscosity model. The eddy viscosity can be further modeled in several different closures [56]. For example in the closure model, the eddy viscosity is hypothesized as a function of the turbulence kinetic energy (TKE, k) and the turbulence dissipation rate (ϵ), for which balance equations are constructed semi-empirically. Lin and Liu [39] have successfully applied the turbulence model in their studies of wave breaking and runup in the surf zone, in which the mean flow is primarily two dimensional. Lin and Lius model has been extended and applied to many different coastal engineering problems, including the wave-structure interaction (e.g., Liu, Lin and Chang 1999 [43]). In the LES method, the three-dimensional turbulent motions are directly simulated and resolved down to a pre-determined scale, and the effects of smaller-scale motions are then modeled by closures, which are still not well understood for complex flows [57]. In terms of the computational expense, LES lies between RANS and DNS. Compared to DNS in solving high-Reynolds-number flows, LES avoids explicitly representing small-scale motions and therefore, the computational costs can be greatly reduced. Compared to RANS models, because the large-scale unsteady motions are computed explicitly, LES can be expected to provide more statistical information for the turbulence flows in which large-scale unsteadiness is significant [56, 57]. Therefore, large eddy simulation is employed to model the turbulence in this study.

The flow governing equations for LES are filtered N-S equations by applying

a low-pass spatial filter. Similar to the RANS approach, a term related to the residual-stress tensor or the sub-grid-scale (SGS) Reynolds stress tensor appears in the filtered N-S equations. Thus, a closure model is also required to relate the residual-stress tensor to the filtered velocity field. The traditional Smagorinsky model [67] is probably the simplest LES-SGS model and has been used in several breaking wave studies [75, 38, 9, 44].

Much work has been done in the numerical modeling of wave-cylinder interaction. Liu [43] developed a two-dimensional model for the wave-structure interaction problem, treating the cylinders as porous structures. However, the flows in practical problems are three-dimensional, thus a three-dimensional model is highly recommended. Ma [46] studied the three-dimensional interaction between waves and fixed bodies based on a fully nonlinear potential flow theory, which is not valid in rotational flow. Li [37] proposed a numerical N-S solver of solving the flow around structures with arbitrary shapes by employing a σ-coordinate transformation. The coordinate transformation, however, is cumbersome when the geometry is very complex. For example, a group of cylinders is inside the computational domain. In addition, the numerical studies of wave-structure interaction so far involve one cylinder only and the cylinder is fixed on a flat bottom, to the author's knowledge. In this study, a three-dimensional numerical model, which was originally designed for studying landslide generated tsunamis[44], is presented to solve the wave-structure interaction problem based on the full Navier-Stokes equations. The irregular mesh is employed so that it can handle the complex geometries with high accuracy.

Recently, Mo, Irschik, Oumeraci and Liu [51] applied the model to calculate

the wave forces acting on a single slender pile, in which the breaking is insignificant. On the other hand, using the same model, Wu and Liu [80] calculated the impact forces acting on a vertical cylinder by a broken bore. The LES model as also described in Wu and Liu [79] solves the filtered NS equations using a two-step projection algorithm with finite volume formulation. The Volume-of-Fluid (VOF) method [27] is employed to track free surface motions. The Smagorinsky SGS model is employed in the model.

1.2 Interface Tracking

In the study of wave-structure interaction problem, the water-air interface (free surface) always poses itself as an important issue. The position of the free surface is part of the solution of the flow, thus it is not known a priori except at the initial time when the free surface is prescribed. However, we need to know the free surface location prior to solving the Navier-Stokes equation to obtain the flow field with a sharp interface present. In the literature, various approaches to track the free surface have be developed, and they are in general divided into two categories [31]: interface tracking methods and interface capturing methods.

The interface tracking methods are essentially Lagrangian. The points on the free surface are tracked by integrating the kinematic equation

$$\frac{d\mathbf{x}_i}{dt} = \mathbf{u}_i \tag{1.2}$$

where $\mathbf{u}_i$ is the velocity of the moving interface point. The interface points can be represented either by mesh grid points or by additional computational markers. One of the interface tracking methods is called moving-mesh method,

which represents the free surface by a moving mesh boundary. The mesh thus is updated in each time step so that its grid points fit with the new free surface position. Liu and Li [38] developed a σ-coordinate transformation model to solve the propagation of surface waves. The σ-coordinate transformation is used to map the irregular physical domain with free surface to the regular computational domain. However, this method only works if the free surface is a single-valued function of the horizontal plane. Therefore, it does not apply to the problems with complex surface topology or highly distorted surface, such as surface reconnecting of plunging-breaker wave on a beach. In addition, this method cannot solve the flow of lighter fluid, such as air flow in the water-air interface flow.

Another tracking method called Marker-and-Cell (MAC) method was first proposed by Harlw and Welch [26] to solve free surface problems, and further developed by Daly [11] to deal with two-fluid flow. The free surface are denoted discretely by massless Lagrangian particles. The particles moves with the free surface within the computational domain which is discretized by a stationary Eulerian mesh. MAC method can in principle deal with arbitrarily free surface topology and does not suffer from numerical diffusion of free surface representation. However, in order to achieve mass conservation in complex free surface situation, MAC method requires a daunting computing efforts, especially in three dimensions, because it has to solve the motion of a large number of Lagrangian markers.

Zhang [83, 84] recently developed a new interface tracking method called polygonal area mapping method (PAM) for two dimensional incompressible free-surface flows. In contrast to the MAC method, PAM method tracks poly-

gons which represent the material areas, and the free surface are represented by the polygonal lines. It has the advantage of little numerical diffusion as MAC method does, but it requires less computation cost. The extension to three dimensional flow and unstructured mesh is not yet articulated, but it is argued to be straightforward. PAM method is more difficult to implement than volume tracking method (VOF method) does.

Interface capturing methods do not "track" the interface explicitly, but rather represent the interface by some color function f that denotes the existence or absence of each fluid material in a computational cell. The transportation of the color function f is numerically solved either by a high resolution continuum advection scheme or by geometrical calculation based on the knowledge of interface position which is "reconstructed" from the color function distribution. Then, the flow is treated as a single continuum flow with a jump in properties, such as density and viscosity.

The use of high resolution continuum advection scheme suffers from the discontinuous nature of color function f because these schemes are in principle designed for continuous functions. Therefore, the discontinuous color function f is usually transformed into a smooth function ϕ as the Level set method [55] does. Level set method defines a smoothly varying distance function $\phi(\mathbf{x}, t)$ as the distance from $\mathbf{x}$ to the interface, and the interface is the zero set of ϕ.

Volume tracking methods, on the other hand, approximate the advection term in the transport equation of f geometrically. The volume tracking method is probably the most popular method for modeling free surface flows mainly because of its relatively easy implementation and incorporation of other physics, such as surface tension. VOF method, first proposed by Hirt and Nichols [27],

is a widely used volume tracking method. In VOF method, a VOF function f is defined in each computational cell as volume fraction of the fluid materials. For example, in water-air flow, $f = 1$ in cells fully filled with water, $f = 0$ in cells without any water, and $0 < f < 1$ denotes a cell containing a free surface. VOF method suffers not only from the numerical diffusion arisen from the spatial representation of the interface used in the interface reconstruction, but also from extreme interface topology, such as high curvature surface regions where the radii of interface curvature is less than a mesh spacing and the thin film cells that contain two water-air interfaces. Lin and Liu [39, 40] successfully applied the VOF method to the simulation of overturning free surfaces. In their model, the free surface is represented as either a horizontal or a vertical line which is a spatially first-order volume tracking scheme. In this study, a spatially second-order volume tracking scheme [60] is used, and details will be discussed in Chapter 3.

1.3 Scope of Present Study

The purpose of this study is to discover the physical phenomena of solitary wave interaction with group of cylinders through the numerical simulation. The wave force and run-up on the structures are studied as well. The numerical results are compared with the laboratory data, and greatly supplement the laboratory measurements by providing a detailed three-dimensional flow field information, the extensive parameter study, etc.

The numerical code is developed from Telluride 2.0 (internal name "Truchas") which is orgiginally written by D. Kothe, J. Sicilian and their Tel-

luride team in Los Alamos National Laboratory. The original Telluride provides a framework to solve the incompressible flow with multi-fluid interfaces. It is further developed to deal with coastal and ocean problems by introducing various wave modules and turbulence models.

In this dissertation, the mathematical model of the incompressible flow will be presented in Chapter 2. Its numerical implementation of finite volume method and interface tracking will be discussed in Chapter 3. Then we will discuss various boundary conditions, such as wall boundary and free surface boundary, and some special techniques used in numerical wave tank, such as the numerical sponge layer. Two numerical wave tests will then be used to evaluate the performance of the numerical algorithm.

In Chapter 4, a non-breaking solitary wave is numerically simulated to impinge on a group of fixed rigid circular cylinders. The free surface elevation, the fluid particle velocity, the pressure around the cylinder and the total wave force will be compared with the laboratory measurements. More cases with extensive wave parameters will be later discussed to supplement the incompleteness of laboratory experiments.

Chapter 5 will discuss a breaking solitary wave on a slanted slope and its impact force on a rigid circular cylinder fixed on the beach. The LES model will be used to model the turbulence effect. The choice of Smagorinsky coefficient will be discussed in the spilling breaker solitary wave case. The simulation of a plunging breaker solitary wave will be compared with the laboratory measurements in terms of free surface profile and velocity field.

CHAPTER 2

MATHEMATICAL FORMULATION OF NUMERICAL MODEL

In this chapter, we first introduce the governing equations describing the wave-structure interaction problems, as well as its initial and boundary conditions. When the wave is breaking, a turbulence model is needed to make feasible the solution of Navier-Stokes equations. Here we introduce a turbulence model called Large Eddy Subgrid Model.

2.1 Governing Equations

We choose an Eulerian methodology to describe the present flow problem. The motion of incompressible Newtonian fluid can be described by classical Navier-Stokes equations derived from the Newton's second law and the condition of incompressibility.

$$\nabla \cdot \mathbf{u} = 0 \tag{2.1}$$

$$\frac{\partial(\rho \mathbf{u})}{\partial t} + \mathbf{u} \cdot \nabla(\rho \mathbf{u}) = -\nabla p + \nabla \cdot \tau + \rho \mathbf{g} \tag{2.2}$$

where $\mathbf{u}$ denotes the velocity field vector, p the pressure, $\mathbf{g}$ the gravity vector, t the time, ρ the density, and τ the stress tensor.

Equation (2.1) is called the condition of incompressibility, representing the conservation of mass. Equation (2.2) represents the conservation of momentum, and the stress tensor τ is a function of the molecular viscosity μ and the rate of strain $\nabla \mathbf{u}$:

$$\tau = \mu(\nabla \mathbf{u} + \nabla^T \mathbf{u}) \tag{2.3}$$

2.1.1 Initial and Boundary Conditions

A typical wave-structure problem setup is shown in Figure 2.1. The most seen boundaries are solid boundary, water-air interface, incident wave boundary and outflow boundary.

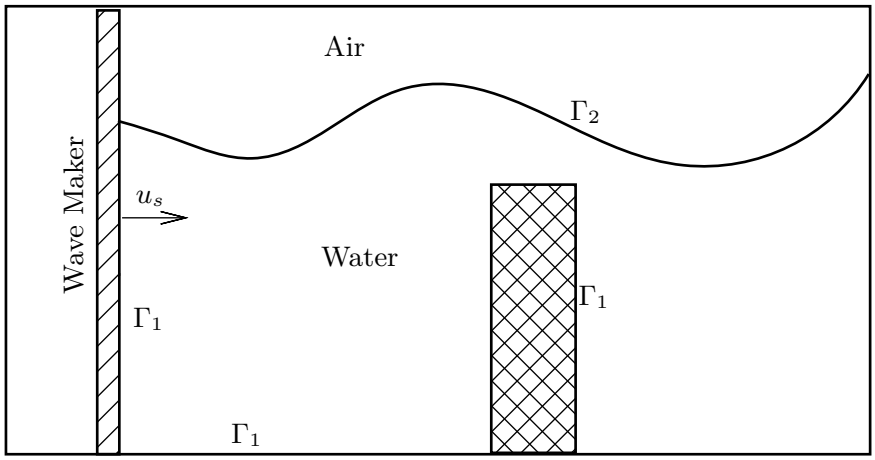

Figure 2.1: Sketch of the flow domain and boundaries. Shaded areas indicate solid materials.

On the solid boundary, whether it is fixed, such as the seabed, or moving, such as the wave maker, the fluid moves at the same speed of the solid boundary, i.e.,

$$\mathbf{u} = \mathbf{u}_s \quad \text{on the solid boundary } \Gamma_1 \tag{2.4}$$

On the water-air interface, both kinematic and dynamic boundary conditions are required. The kinematic boundary condition requires that the water-air interface is a material surface and there is no flow flux across it. If the surface can be described as a function $F(\mathbf{x}, t) = 0$, the kinematic free surface condition is

$$\frac{DF(\mathbf{x}, t)}{Dt} = 0 \quad \text{on the free surface } \Gamma_2 \tag{2.5}$$

The dynamic free surface condition requires that the stresses are continuous across the free surface. Without considering the surface tension and the wind stress, the dynamic free surface condition can be expressed as

$$-p + 2\mu \frac{\partial u_n}{\partial n} = S_n \tag{2.6}$$

$$\mu \left(\frac{\partial u_{\tau_k}}{\partial n} + \frac{\partial u_{\tau_n}}{\partial \tau_k} \right) = S_{\tau_k} \tag{2.7}$$

where the subscript n indicates the outward normal direction and τ_k the two tangential directions ($k = 1, 2$) on the free surface. S_n and S_{τ_k} are the normal and tangential components of stresses produced by the air flow on the free surface.

On the incident wave boundary, the fluid velocities **u** and free surface elevation $\eta(t)$ are prescribed either from the analytical formula or from the laboratory measurements. On the outflow boundary, we can apply the radiation boundary condition:

$$\frac{\partial \phi}{\partial t} + C_g \frac{\partial \phi}{\partial n} = 0 \tag{2.8}$$

where ϕ is the physical quantity associated with the outgoing wave, such fluid velocity **u**, n the outward normal direction of the outflow boundary and C_g the group velocity of outgoing wave. The radiation boundary condition requires knowledge of the energy propagation of the outgoing wave, thus its application is limited to the long wave of which the group velocity can be estimated by

$$C_g = \sqrt{g(h + \eta)} \tag{2.9}$$

where h is the local still water depth and η the free surface elevation.

2.2 Large Eddy Simulation

In principle, the numerical solution of Navier-Stokes equations (2.1)– (2.3) gives the complete flow information of the turbulent incompressible flow. Then the discretization in space and time must be as fine as the characteristic length and time associated with the smallest dynamic scales, i.e. the Kolmogorov scales. However, even for the simplest homogeneous and isotropic turbulent flow, $O(Re^{9/4})$ degrees of freedoms in space and $O(Re^3)$ number of time steps are needed to numerically solve all the scales in a cubic volume of edge length L [64], where $Re = UL/\nu$ is the Reynolds number, U and L are characteristic length and velocity of the flow, ν is the kinematic viscosity of the fluid. Therefore, the nowadays computer capacity is far less sufficient to solve all the spatial and time scales of the turbulent flow under high Reynold number Re. The direct numerical simulation (DNS) of the incompressible flow is only constrained to relatively low Reynolds number turbulent flows within a small computational domain. In this section, the Large Eddy Simulation (LES) will be introduced to relieve the difficulty encountered in DNS.

2.2.1 Filtering

The advection term in Navier-Stokes equation (2.2) indicates that all the scales of the flow are nonlinear coupling, thus we cannot solve all the scales independently. In high Reynolds number flow, direct numerical simulation is not feasible due to the large scale separation. A common practice to overcome this difficulty is to solve the flow motion in some scales while modeling the effect from other unresolved scale motion to the resolved scale motion. For example,

the classical Reynolds average numerical simulation (RANS) solves the mean flow and model the effect of all scales to the mean flow. LES, on the other hand, solves the large eddy motions and provides a sub-grid model to describe the unresolved motion.

Mathematically, LES is to apply a low-pass filter to the velocity field. A filtered variable is defined as [36]:

$$\bar{\phi}(x,t) = \int \phi(x',t) G(x-x',t)\, dx' \tag{2.10}$$

where G is the filter function and is also called convolution kernel. The filter function G is linear, commutes with derivation and satisfies the normalization condition:

$$\int G(x-x',t)\, dx' = 1 \tag{2.11}$$

The classical filters for LES are box filter, Gaussian filter and spectral filter. In this study, we are solving the governing equations in physical space using finite volume method, thus the grid behaves as a filtering operation also called "implicit filter":

$$\bar{\phi}(x,t) = \frac{1}{V} \int_{\omega} \phi(x',t)\, dx' \tag{2.12}$$

where V is the volume of computational cell, and the integral is over the cell space Ω. Therefore, a box filter is a natural choice of the filter function G:

$$G(x-x',t) = \begin{cases} \frac{1}{V}, & \text{inside } \Omega \\ 0, & \text{otherwise} \end{cases} \tag{2.13}$$

By applying the filter operation to Navier-Stokes equations (2.1) and (2.2), we obtain the filtered continuity and momentum equations:

$$\frac{\partial \bar{u}_i}{\partial x_i} = 0 \tag{2.14}$$

$$\frac{(\partial\rho\bar{u}_i)}{\partial t} + \frac{\partial(\rho\overline{u_i u_j})}{\partial x_i} = -\frac{\partial\bar{p}}{\partial x_i} + \rho g_i + \frac{\partial}{\partial x_j}\left(\mu\left(\frac{\partial\bar{u}_i}{\partial x_j} + \frac{\partial\bar{u}_j}{\partial x_i}\right)\right) \tag{2.15}$$

where the overbar denotes the filtered variables. The filtering of momentum equation introduces an unknown quantity $\overline{u_i u_j}$ which should be modeled from the resolved velocity filed $\bar{u}_i$. We first define the residual stress as:

$$\tau^R_{ij} \equiv \rho(\overline{u_i u_j} - \bar{u}_i\bar{u}_j) \tag{2.16}$$

which is also called sub-grid scale Reynolds stress. And the anisotropic residual stress is defined by:

$$\tau^r_{ij} \equiv \tau^R_{ij} - \frac{2}{3}k_r\delta_{ij} \tag{2.17}$$

where k_r is the residual kinetic energy $k_r \equiv \tau^R_{ii}/2$. The modified filtered pressure is defined by incorporating the isotropic residual stress:

$$\bar{p}\prime \equiv \bar{p} + \frac{2}{3}k_r \tag{2.18}$$

therefore, the filtered momentum equation (2.15) can be expressed as:

$$\frac{(\partial\rho\bar{u}_i)}{\partial t} + \frac{\partial(\rho\bar{u}_i\bar{u}_j)}{\partial x_i} = -\frac{\partial\bar{p}}{\partial x_i} + \rho g_i + \frac{\partial}{\partial x_j}\left(\mu\left(\frac{\partial\bar{u}_i}{\partial x_j} + \frac{\partial\bar{u}_j}{\partial x_i}\right)\right) - \frac{\partial\tau^r_{ij}}{\partial x_j} \tag{2.19}$$

where $\bar{p}$ is the modified filtered pressure.

2.2.2 Turbulent Viscosity Assumption

It assumes that the residual stress aligns with the resolved local strain rate **S**:

$$\tau^r_{ij} = -\rho\nu_t\left(\frac{\partial\bar{u}_i}{\partial x_j} + \frac{\partial\bar{u}_j}{\partial x_i}\right) = -2\rho\nu_t\bar{S}_{ij} \tag{2.20}$$

where ν_t is called turbulent viscosity or subgrid-scale viscosity of the residual motion in LES context.

2.2.3 Smagorinsky sub-grid model

Smagorinsky sub-grid model is most popular model in LES application because of its simplicity. The subgrid-scale viscosity is modeled as a function of local grid size and magnitude of rate of strain:

$$\nu_t = (C_s \Delta)^2 \bar{S} \tag{2.21}$$

where C_s is called Smagorinsky coefficient, Δ is the characteristic filter size, and $\bar{S}$ is the magnitude of strain rate:

$$\bar{S} = (2\bar{S}_{ij}\bar{S}_{ij})^{1/2} \tag{2.22}$$

The Smagorinsky coefficient C_s is not a constant in general. It varies from 0.1 to 0.2 in different flow regions, for example, $C_s \simeq 0.2$ in isotropic turbulent flow and $C_s = 0.065$ for shear flow. The characteristic filter size is proposed by Deardoff [14, 13]:

$$\Delta = (\Delta x \Delta y \Delta z)^{1/3} \tag{2.23}$$

on regular orthogonal mesh, or on irregular mesh:

$$\Delta = V^{1/3} \tag{2.24}$$

where V is the volume of computational cell.

2.2.4 RNG Smagorinsky sub-grid model

An obvious drawback of Smagorinsky sub-grid model is that the turbulent viscosity always exists as long as the resolved velocity field has spatial variations. In a typical coastal problem, the ocean wave is usually a laminar flow. As it

reaches the coastal beach or impinges the coastal structures, the wave eventually breaks and generates a complex turbulent field. It is obvious that the classical Smagorinsky model cannot describe the transition from laminar to turbulent flow.

Yakhot [82, 68] developed a sub-grid model based on renormalization group theory:

$$\nu_t = \nu_0 \left[1 + \mathrm{H}\left(\frac{(Cs\Delta)^4(\nu_t + \nu_0)}{\nu_0^3} |S|^2 - 75 \right) \right]^{1/3} - \nu_0 \tag{2.25}$$

where ν_0 is the laminar viscosity, $H(x)$ denotes the Heaviside function defined as:

$$H(x) = \begin{cases} x, & x > 0 \\ 0, & \text{otherwise} \end{cases} \tag{2.26}$$

Therefore, the effect of sub-grid scale turbulence can only arise in high strain fields, which is represented by the Heaviside function. In low strain flows, the turbulent viscosity tends to zero so that the total viscosity $\nu = \nu_0 + \nu_t$ is the laminar kinematic viscosity. It is also noted that, equation (2.25) approaches asymptotically to the classical Smagorinsky model. The eddy viscosity ν_t in equation (2.25) is evaluated at each time step and can be solved by Newton-Raphson iteration.

2.2.5 Near Wall Treatment

In the near-wall region, there exists a viscous sublayer which is usually unresolved in LES application, and the Smagorinsky coefficient C_S is reduced very much. However, this cannot be reflected in Smagorinsky-type subgrid models, and the turbulent eddy viscosity does not vanish near the wall as a result.

Therefore, a near-wall model is required to solve the grid resolution and model error issues. Cabot and Moin [4] proposed a near-wall damping function in the cell adjacent to the wall:

$$\frac{\nu_t}{\nu} = \kappa y^+ (1 - \exp^{-y^+/A})^2 \tag{2.27}$$

where $y^+ = y_w u_\tau / \nu$ is the dimensionless distance from the cell centroid to the wall, $\kappa = 0.41$ and $A = 19$.

2.2.6 Choice of grid size

In the theoretical derivation of LES sub-grid model, the filter size is always assumed to be well inside the inertial range of the turbulent flow, which is such a range of scales of turbulent motion that viscous effects are negligible. In turbulence literature, a length scale L_{EI} is defined as the demarcation between the anisotropic large eddies and the isotropic small eddies, and experiments for isotropic turbulence show that 80% of the total flow energy is within the motions of length scales [56]:

$$L_{EI} = \frac{1}{6} L_{11} < l < 6 L_{11} \tag{2.28}$$

where L_{11} is the longitudinal integral length and $L_{11} = l_0$ at high Reynolds number (l_0 is the characteristic length scale of the eddies in the largest size range).

In our numerical model, the grids are used as a box filter, therefore proper grid resolution is required to resolve all the "large" turbulent scales. In other words, 80% of the total flow energy will be resolved on proper grids. And the large eddy simulation requires that the grid size should be smaller than L_{EI} [56]:

$$\Delta < L_{EI} \tag{2.29}$$

and at high Reynolds number, we have

$$\frac{\Delta}{l_0} < \frac{1}{6} \tag{2.30}$$

Since LES model assumes the filter width is well inside the inertial range, it is reasonable to use

$$\frac{\Delta}{l_0} < \frac{1}{10} \tag{2.31}$$

as an estimation of proper grid size. Therefore, the determination of local largest eddy size l_0 is important in the mesh generation before the numerical LES simulation. In this study, the local largest eddy size l_0 is estimated from the laboratory data.

CHAPTER 3

NUMERICAL IMPLEMENTATION OF NUMERICAL MODEL

Analytical solutions of coastal problems are not always available due to the flow complexity. One effective way to study the coastal problems is to numerically modeling the physics phenomena and to use numerical methods to obtain the solution of the Navier-Stokes equations of multi-phase flows with strong material interfaces deformation.

In the present study, a numerical code, Telluride (or Truchas), developed in Los Alamos National Laboratory (LANL), is utilized and it is further developed to include turbulence models and wave modules to study coastal problems with complex flow conditions. Thus, the scope of this chapter is to discuss the numerical methods developed in Telluride.

We will first discuss the discretization of the governing equations. Then, the VOF technique which is to capture the free surface will be discussed. A solution algorithm called projection method is later presented, followed by the numerical implementation of boundary conditions. At last, a test case is presented to show the performance of the numerical code.

3.1 One-Field Model

In coastal problems, we often encounter more than one fluid, such as water, air and mud. To solve their flows in a unified frame, a one-field model is introduced as an assumption. Consider k incompressible, immiscible Newtonian fluids, each fluid is assumed to move with a single velocity field at any point in space:

$$\mathbf{u}_k = \mathbf{u} \tag{3.1}$$

where **u** is the representative velocity of the computational cell. In finite volume method, it is the local integrally averaged velocity defined at the cell centroid:

$$\mathbf{u} = \frac{1}{V}\int \mathbf{u} dV \tag{3.2}$$

where V is the volume of each computational cell.

With this one-field model, k Navier-Stokes equations are replaced by one mass and momentum equations. Therefore, solutions are sought for the incompressible Navier-Stokes equations of the one-field model. In other words, we are solving a flow of the equivalent fluid whose density and viscosity are some averaged value of the k fluids. The average quantities will be discussed in later sections.

3.2 Discretization Method

There are four categories of discretization methods in Computational Fluid Dynamics (CFD): finite difference method (FDM) [59, 70], finite volume method (FVM) [17, 74], finite element method (FEM) [86] and spectral method [20].

Spectral method has advantages in its high order approximation of derivatives of physical variables. However, its application is mostly limited to periodic domains with structure meshes. The finite element method is effectively applied to solve the parabolic or elliptic partial differential equations on complex unstructured meshes. The finite difference method is the most popular method and usually used in orthogonal structure meshes. Its implementation on general non-orthogonal unstructured mesh needs great efforts [66].

The finite volume method is quite close to FEM since its discretization be-

gins with the integral form of the partial differential equations. It reduced to FDM on a structure orthogonal mesh, thus it is often loosely said to be synonymous with FDM, which is fundamentally untrue. The most appealing feature of FVM is that the conservation of discrete physical quantities (such as mass and momentum) is inherent in its implementation. It can be also easily applied to general unstructured meshes, which makes it well suitable for complex computational geometries. In the present study, we use finite volume method to discretize the governing equations.

The governing equation (2.2) can be rewritten in a general conservation equation:

$$\frac{\partial \phi}{\partial t} + \nabla \cdot (\mathbf{u}\phi) = S(\phi) \tag{3.3}$$

where ϕ is a general variable, such as passive scalar or velocity components, and $S(\phi)$ is a source function of ϕ. The finite volume method first integrate the general equation (3.3) over the computational cell (control volume):

$$\int \left[\frac{\partial \phi}{\partial t} + \nabla \cdot (\mathbf{u}\phi) \right] dV = \int S(\phi) dV \tag{3.4}$$

and applying the Gauss divergence theorem it can be expressed as:

$$\int \frac{\partial \phi}{\partial t} dV + \int_A \mathbf{n}_f \cdot (\mathbf{u}\phi) dA = \int S(\phi) dV \tag{3.5}$$

where $\mathbf{n}_f$ is the outward unit normal vector of the cell faces.

Since the flow domain is partitioned into a number of computational cells, we need to approximate the continuous PDE (3.5) in the discrete point of view:

$$\phi_i^{n+1} - \phi_i^n + \frac{1}{V_i} \sum_f \delta t [\mathbf{n} \cdot \mathbf{u}^n]_f A_f \phi_f^n = \frac{\delta t S_i^n}{V_i} \tag{3.6}$$

where the subscript i denotes the computational cell, subscript f the cell face, superscript n the n^{th} time step, V_i the control volume of computational cell i, A_f the cell face area, and $\mathbf{n}$ the outward unit normal vector of the cell face.

In the discrete algebraic equation (3.6), we approximate the face integral in (3.5) as a sum over all the computational cell faces, and ϕ_i, S_i are local integrally averaged value:

$$\phi_i = \frac{\int \phi dV}{\int dV} = \frac{\int \phi dV}{V_i} \tag{3.7}$$

and

$$S_i = \frac{\int S dV}{\int dV} = \frac{\int S dV}{V_i} \tag{3.8}$$

Another issue of discretization is the placement of the physical variables. In this study, all the fluid variables, such as velocity, pressure and density, are stored at the geometric centroid of each computational cell (cell centroid), which is usually referred to as colocated positioning. The colocated positioning makes the implementation of discretization in three dimensional and on general unstructured meshes less complex than the staggering positioning does.

3.3 Interface Tracking Algorithm

As stated before, we are dealing with interfacial flows with more than one fluid. However, the location of the interfaces is unknown a priori except at the initial time when the interfaces are prescribed. Thus, an interface tracking algorithm is needed to solve the interface locations. As stated in [60, 53, 32], the volume tracking algorithms work effectively in both structured and unstructured meshes. With the assumption of one-field model, a volume tracking algorithm [33] was implemented due to its robustness and computational efficiency. It reconstructs piecewise linear (planar) fluid interfaces from discrete fluid volumes in each computational cell, having at least second order accuracy in space. The details of the algorithm will be presented in the following.

3.3.1 Volume-of-Fluid Function

Considering k incompressible, immiscible fluids of constant fluid density ρ_k^0, we define a Volume-of-Fluid (VOF) function as volume fraction of a cell volume V occupied by fluid k:

$$f_k = \frac{V_k}{V} \tag{3.9}$$

The VOF function f_k are bounded by $0 \leq f_k \leq 1$, and it defines the presence or absence of each fluid in the computational cell:

$$f_k = \begin{cases} 0, & \text{outside fluid } k, \\ > 0, < 1, & \text{at the fluid } k \text{ interface}, \\ 1, & \text{inside fluid } k. \end{cases} \tag{3.10}$$

The interface position of fluid k is thus defined as the transition region with $0 < f_k < 1$ which has a finite width on the order of mesh spacing. The sum of the volume fraction must be unity, $\sum_k f_k = 1$, since fluid volumes are volume-filling. The fluid density ρ_k is then defined as the mass M_k of fluid k per unit total volume V:

$$\rho_k = \frac{M_k}{V} = \frac{V_k}{V}\frac{M_k}{V_k} = f_k \rho_k^0 \tag{3.11}$$

and it satisfies the mass conservation equation for each fluid k:

$$\frac{\partial \rho_k}{\partial t} + \nabla \cdot (\rho_k \mathbf{u}) = 0 \tag{3.12}$$

Substituting (3.11) into (3.12) and considering that ρ_k^0 is constant, we obtain an evolution equation for f_k:

$$\frac{\partial f_k}{\partial t} + \nabla \cdot (f_k \mathbf{u}) = 0 \tag{3.13}$$

Equation (3.13) is called VOF equation which describes the evolution of the location of each fluid. Therefore, the system of equations for the one-field model

is composed of equations (2.1), (2.2), and (3.13) for the unknowns $\mathbf{u}$, p and f_k. The average density (also called cell density) in (2.2) is defined as

$$\rho = \sum_k f_k \rho_k^0 \tag{3.14}$$

which simply represents the local mass conservation. The average viscosity, on the other hand, is not constrained by a conservation law, thus it either takes the serial average:

$$\mu = \sum_k f_k \mu_k \tag{3.15}$$

or the parallel (harmonic) average:

$$\mu_k = \left(\sum_k \frac{f_k}{\mu_k} \right)^{-1}. \tag{3.16}$$

Rudman [61] noted that use of harmonic average gives better results in calculating the average viscosity at the cell face.

3.3.2 Volume Tracking Algorithm

In order to solve equation (3.13) for f_k^{n+1}, the knowledge of interfaces inside the computational cell is needed to calculate the advection of VOF function. Thus the interface needs to be reconstructed based on the discrete VOF function values. A multidimensional PLIC (piecewise linear interface calculation) volume tracking algorithm, first developed by Rider and Kothe [60], is employed to reconstruct the interface in the computational cells. The algorithm is composed of two steps: first a planar reconstruction of interfaces inside a cell from the VOF function f_k^n and the estimation of the interface orientation; then a geometrical calculation of volume fluxes of each fluid across each cell face. The volume fluxes is then used to update the VOF function in every cell, and later for the

mass and momentum advections of other quantities. The algorithm details will be discussed in the following sections.

Estimation of Interface Orientation

The orientation of the interface between fluid k and other fluids is approximate as the gradient of VOF function f_k^n:

$$\hat{\mathbf{n}} = \frac{\nabla f_k}{|\nabla f_k|} \tag{3.17}$$

The gradient of f_k is calculated by the least squares algorithm[78]. Then the reconstructed interface which is assumed to be a plane can be given by the equation:

$$\hat{\mathbf{n}} \cdot \mathbf{x} - \lambda_p = 0 \tag{3.18}$$

where $\mathbf{x}$ is a point on the plane and λ_p the plane constant which fits the fluid volume exactly to its VOF function f_k^n. This planar approximation is good if the radii of the curvature of the interface is at least two times the local mesh spacing.

Interface Capture

The next step is to determine the plane constant λ_p in equation (3.18) so that the volumes truncated by the plane corresponds exactly to the VOF value f_k. This will be done in an iterative procedure.

Consider the reconstructed interface between fluid k and other fluids. It divides the cell into two regions either behind or before the interface plane according to the estimated interface orientation $\hat{\mathbf{n}}$ as shown in Figure 3.1. By the definition (3.17), $\hat{\mathbf{n}}$ points to the fluid k, i.e. the region behind the interface plane.

Let the truncation volume V_{tr} be the volume of the region behind the interface plane. V_{tr} is dependent on the plane constant λ_p. Its calculation is more detailed in [60] and [33].

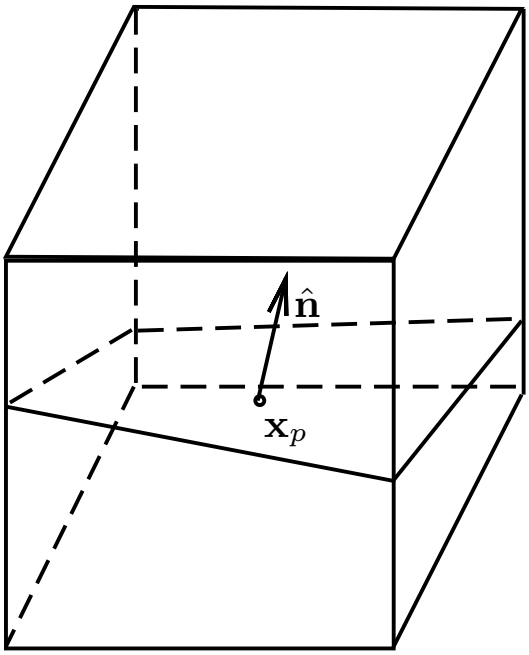

Figure 3.1: A computational cell truncated by a plane with unit normal vector $\hat{\mathbf{n}}$.

Let $F(\lambda_p)$ be the residual of the truncation volume V_{tr} and the exact volume of fluid k inside a computational cell:

$$F(\lambda_p) = V_{tr} - f_k V \tag{3.19}$$

where V is the cell volume. When $F(\lambda_p)$ is zero or smaller than a prescribed convergence criterion, the corresponding plane constant λ_p is used to reconstruct the interface plane by equation (3.18). Rider and Kothe [60] suggested Brent's method [58] to find the root of equation (3.18).

Updating VOF Function

After reconstruction of the interface within the cell, the volume fluxes of each fluid across the cell faces, such as $\delta V_{1,f}$ and $\delta V_{2,f}$ shown in Figure 3.2, are calculated based on the knowledge of interface and cell geometries. Then the VOF value at new time step $n+1$ is evaluated by the discretization formula:

$$f_k^{n+1} = f_k^n - \frac{1}{V}\sum_f \delta V_{k,f}^n = f_k^n - \frac{1}{V}\sum_f \delta t(\mathbf{n}_f \cdot \mathbf{u}_f^n) A_f f_{k,f}^n \tag{3.20}$$

where $f_{k,f}^n$ is the VOF value of fluid k at the cell face f:

$$f_{k,f} = \frac{\delta V_{k,f}}{\delta V_f} \tag{3.21}$$

where δV_f is the total volume flux across the cell face f.

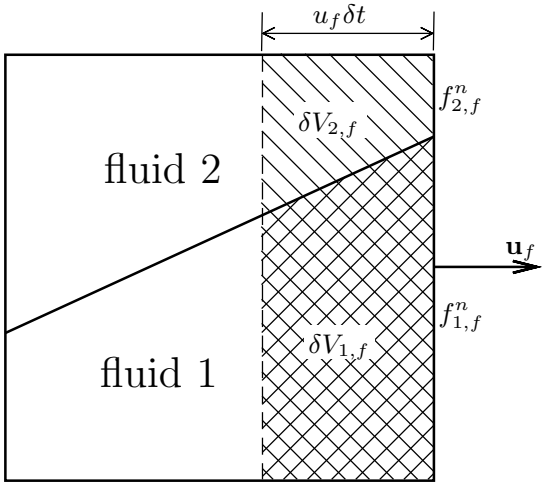

Figure 3.2: The volume fluxes across a cell face of a 2D cell containing two fluids.

The multidimensional PLIC volume tracking algorithm is now summarized as follows:

I) Estimate the interface orientation by equation (3.17).

II) Determine the plane constant λ_p by using Brent's method to find the root of equation (3.18) so that the interface within the cell is reconstructed.

III) Calculate the volume fluxes of each fluid across the cell faces.

IV) Update the VOF value of each fluid in every cell.

Void Model

Instead of solving equation for air, we treat the air as voids in our simulation to simplify the equations to be solved, since both momentum fluxes and pressure gradients are usually much smaller the air region than in the water region.

Voids are dummy fluid with zero density and viscosity, thus have zero momentum and a fixed pressure which is set to zero in practice. Therefore, Navier-Stokes equations are not necessarily to be solved in computational cells fully occupied by voids.

In mixed cells which contain a mixture of voids and other fluids, the "compressibility" of voids has to be considered so that internal void regions (bubbles) could collapse completely. The compressibility of voids can be expressed as:

$$\nabla \cdot \mathbf{u} = \xi \frac{\partial P}{\partial t} \tag{3.22}$$

where ξ is the compressibility of local fluid and can be modeled as:

$$\xi \equiv -\frac{1}{\rho C^2} \tag{3.23}$$

where C is the effective "sound speed" of the voids, and ρ is the cell density in the mixed cells.

3.4 Projection Method

Projection methods have a long history in solving Navier-Stokes equations. It was first introduced by Chorin [7, 8] and then developed by Bell and coworkers for the solution of constant-density [2] and variable-density [1] incompressible Navier-Stokes equations. In projection methods, an intermediate velocity field $\mathbf{u}^*$ is first obtained without regard for its divergence free constraint in (2.1), and then the solenoidal velocity field $\mathbf{u}^d$ is recovered by a projection operator P:

$$\mathbf{u}^d = P(\mathbf{u}^*) \tag{3.24}$$

It begins with splitting the momentum equation (2.2) into two fractions:

$$\frac{\rho^{n+1}\mathbf{u}^* - \rho^n\mathbf{u}^n}{\Delta t} = -\nabla\cdot(\rho\mathbf{u}\mathbf{u})^n + \nabla\cdot(\mu^n(\nabla\mathbf{u} + \nabla^T\mathbf{u})^n) - \nabla p^n + \rho^n\mathbf{g} \tag{3.25}$$

$$\frac{\rho^{n+1}\mathbf{u}^{n+1} - \rho^{n+1}\mathbf{u}^*}{\Delta t} = -\nabla\delta p^{n+1} + (\rho^{n+1} - \rho^n)\mathbf{g} \tag{3.26}$$

Equation (3.25) gives an estimation of intermediate velocity $\mathbf{u}^*$, referred to as predictor step. Equation (3.26) is a relation for solenoidal velocity field $\mathbf{u}^{n+1}$ at time step $n+1$, termed as projection step. Note that the time discretization of the time derivative is already employed here.

Taking divergence of equation (3.26), we obtain the Poisson Pressure Equation (PPE):

$$\nabla\cdot\left(\frac{\nabla\delta p^{n+1}}{\rho^{n+1}}\right) = \nabla\cdot\left(\frac{\mathbf{u}^*}{\Delta t} + (\rho^{n+1} - \rho^n)\mathbf{g}\right) \tag{3.27}$$

since $\mathbf{u}^{n+1}$ is solenoidal. The solution of PPE involves solving a system of linear equations. Once the pressure increment δp is obtained, equation (3.26) is used to calculate the solenoidal face velocity field:

$$\mathbf{u}_f^{n+1} = \mathbf{u}_f^* - \Delta t\left(\frac{\nabla\delta p_f^{n+1}}{\rho_f^{n+1}} - \delta\rho_f\mathbf{g}\right) \tag{3.28}$$

where $\delta\rho_f = \rho_f^{n+1} - \rho_f^n$.

Finally, the new time step velocity field $\mathbf{u}^{n+1}$ is calculated from equation (3.26) where the cell-centered pressure gradient $\nabla\delta p^{n+1}/\rho^{n+1}$ is interpolated from $\nabla\delta p_f^{n+1}/\rho_f^{n+1}$.

In the following sections, we will discuss the details of the numerical implementation of the projection method.

3.4.1 Momentum Advection

Momentum advection term $\nabla\cdot(\rho\mathbf{u}\mathbf{u})^n$ in equation (3.25) will be calculated by the face-centered velocities when finite volume method is used as discussed in Section 3.2:

$$\Delta t\int\nabla\cdot(\rho\mathbf{u}\mathbf{u})^n dV \approx \sum_f \delta V_f^n\langle\rho\mathbf{u}\rangle_f^n \tag{3.29}$$

where δV_f is the advected volume across the cell face. Figure 3.2 illustrates the advection of two fluids across the right face of an interface cell. The advected volume is:

$$\delta V_f = \Delta t A_f \mathbf{u}_f\cdot\hat{\mathbf{n}}_f \tag{3.30}$$

where $\mathbf{u}_f$ is the solenoidal face velocity from previous time step and A_f is the cell face area. The advected volume $\delta V_{k,f}$ of each fluid within the advected volume δV_f (see Figure 3.2) is calculated in the volume tracking algorithm. Let $f_{k,f}$ be the volume fraction of δV_f associated with a fluid k:

$$f_{k,f} = \frac{\delta V_{k,f}}{\delta V_f} \tag{3.31}$$

then the advected mass of each fluid k across the cell face can be expressed as:

$$M_{k,f} = \rho_k^0\delta V_{k,f} \tag{3.32}$$

and the total mass flux across the cell face f is

$$M_f = \sum_k M_{k,f} \tag{3.33}$$

therefore the momentum advection is finally calculated in a way consistent with the mass advection:

$$\Delta t \int \nabla \cdot (\rho \mathbf{u}\mathbf{u})^n dV \approx \sum_f \delta V_f^n \langle \rho \mathbf{u} \rangle_f^n = \sum_f \sum_k M_{k,f}^n \langle \mathbf{u} \rangle_f^n = \sum_f M_f^n \langle \mathbf{u} \rangle_f^n \tag{3.34}$$

where the bracket $\langle\rangle_f$ indicates that the face velocity here is not the old time n solenoidal $\mathbf{u}_f$. $\langle \mathbf{u} \rangle_f$ is an estimate of the advected momentum per unit mass. In this study, a first-order upwind scheme is employed to calculate $\langle \mathbf{u} \rangle_f$.

3.4.2 Momentum Diffusion

The viscous stress in equation (3.25) assumes that all the fluids are Newtonian and it is explicitly calculated using n time step information so that it is no need to solve a system of equations.

The discretization of the viscous stress can be expressed as:

$$\Delta t \int \nabla \cdot \left(\mu^n (\nabla \mathbf{u} + \nabla^T \mathbf{u})^n \right) = \Delta t \sum_f \mu_f^n A_f \left[\hat{\mathbf{n}}_f \cdot (\nabla \mathbf{u} + \nabla^T \mathbf{u})_f^n \right] \tag{3.35}$$

The face velocity gradient is interpolated from the neighboring cells and the face viscosity μ_f is harmonically averaged from cell center viscosity:

$$\mu_f = \frac{2}{1/\mu_{nb} + 1/\mu_P} \tag{3.36}$$

where the subscript nb denotes neighbor cell center and i the center of the cell to which the face belongs.

3.4.3 Pressure Poisson Equation

Integrating equation (3.27) and using divergent theorem, we obtain the discretization of the Pressure Poisson Equation:

$$\sum_f \left(A_f \hat{\mathbf{n}}_f \cdot \frac{\nabla \delta p_f^{n+1}}{\rho_f^{n+1}} \right) = \sum_f \left(A_f \hat{\mathbf{n}}_f \cdot \frac{\mathbf{u}_f^*}{\Delta t} + (\rho_f^{n+1} - \rho_f^n)\mathbf{g}_f \right) \tag{3.37}$$

where the face pressure gradient $\nabla \delta p_f$ is evaluated by

$$\nabla \delta p_f = \frac{\delta p_{nb} - \delta p_i}{\Delta l} \frac{\vec{\Delta l}}{\Delta l} \tag{3.38}$$

where δp_{nb} and δp_i are the cell centered pressure increments for cell i and its neighbor nb. $\vec{\Delta l}$ is the vector distance from centroid of cell i to centroid of its neighbor nb, and Δl is its magnitude. $\hat{\mathbf{n}}_f$ is the cell face normal. The intermediate face velocity $\mathbf{u}_f^*$ is interpolated from neighbor cells.

Thus, we solve equation (3.37) for cell centered pressure increment δp^{n+1}. It is a set of linear algebraic equations which can be expressed in matrix notation as:

$$\mathbf{A}\mathbf{x} = \mathbf{b} \tag{3.39}$$

where $\mathbf{A}$ is the coefficient matrix from the discretization (3.37) and (3.38), $\mathbf{x}$ is the cell centered pressure increment, and $\mathbf{b}$ is from the RHS of equation (3.37). In general $\mathbf{A}$ is sparse and symmetric, and a bunch of mature iterative equation solvers are available as a mathematics software package. JTpack90 [73], a linear algebra package, is chosen in the present study, and we use the Krylov subspace methods [19, 62]. Specifically, the preconditioned generalized minimal residual (GMRES) algorithm [63] is used for 3D general unstructured mesh.

3.4.4 Computational Cycle

Starting with information from n time step, such as $\mathbf{u}^n$, $\mathbf{u}_f^n$ and p^n, we advance the solution to $n+1$ time step in the following steps:

I) Use multidimensional PLIC volume tracking algorithm described in Section 3.3 to obtain f_k^{n+1} of each fluid and the cell density ρ^{n+1}. The volume flux $\delta V_{k,f}$ of each fluid within the total advected volume is also calculated by geometric relations.

II) Evaluate intermediate velocity $\mathbf{u}^*$ by equation (3.25) of which the momentum advection and diffusion are calculated as in Section 3.4.1 and 3.4.2.

III) Interpolate cell centered $\mathbf{u}^*$ and ρ^{n+1} to the cell faces to obtain $\mathbf{u}_f^*$ and ρ_f^{n+1}.

IV) Solve the Pressure Poisson Equation to obtain cell centered pressure increment δp^{n+1} as in Section 3.4.3.

V) A solenoidal face velocity field $\mathbf{u}_f^{n+1}$ is projected out of $\mathbf{u}_f^*$ by equation (3.28).

VI) The $n+1$ time step cell centered velocity field $\mathbf{u}^{n+1}$ is calculated by equation (3.26) where the cell centered pressure gradient is interpolated from the face pressure gradient, and the cell centered pressure p^{n+1} is corrected by pressure increment δp^{n+1}.

The overall accuracy of this algorithm is first order in time and space due to the forward Euler time discretization and first-order upwind scheme. From our numerical experience [39, 40, 78], this accuracy suffices to study the breaking wave problems.

3.5 Boundary Conditions

We have introduced the mathematical formulations of boundary conditions in Chapter 2, and their numerical implementation will discussed in this section.

3.5.1 Free-slip Stationary Wall Boundary

The free-slip wall is impermeable and does not generate tangential wall shear stress. And it behaves like a mirror, thus is also called symmetric plane. If the wall shear stress is not significant to the main interested region and a coarse near-wall grid is used, the free-slip wall boundary condition is usually applied in practice.

On the free-slip wall boundary, the velocity component normal to the wall is zero while the tangential component is subject to the flow. Therefore there is no convective fluxes across the free-slip wall.

$$\hat{\mathbf{n}} \cdot \mathbf{u}|_{wall} = 0 \tag{3.40}$$

In the momentum diffusion calculation, $\partial u_\tau / \partial n = 0$ will be applied on the free-slip wall. u_τ is the tangential component of velocity on the wall. In the discrete pressure Poisson equation (3.37), the normal pressure gradient is required:

$$\frac{\partial p}{\partial n} = 0 \quad \text{on the wall} \tag{3.41}$$

so is the normal pressure increment gradient

$$\frac{\partial \delta p}{\partial n} = 0 \quad \text{on the wall} \tag{3.42}$$

which is also called pressure Neumann boundary condition.

3.5.2 No-slip Stationary Wall Boundary

The viscous fluid particle sticks to the no-slip solid wall, thus the velocity on the wall is always zero, $\mathbf{u} = 0$ on the wall, which is the so-called Dirichlet boundary condition. Also, there is no convective fluxes across the solid wall. Along the no-slip solid wall, we have

$$\partial \mathbf{u}_\tau / \partial \tau_k = 0 \tag{3.43}$$

thus it is easily seen from the mass conservation equation that

$$\frac{\partial u_n}{\partial n} = 0 \quad \text{on the wall} \tag{3.44}$$

where τ_k is the unit tangential vector of the wall ($k = 1, 2$ in 3D flow), $\mathbf{u}_\tau$ is the velocity vector tangential to the wall, and n is the unit normal of the wall.

In the momentum diffusion calculation, equation (3.43) and (3.44) will be applied, and the rest of shear stress on the wall is estimated by a one-side interpolation approximation. The normal pressure gradient on the wall is usually assumed to be zero, therefore the normal pressure increment gradient on the wall is also zero:

$$\frac{\partial \delta p}{\partial n} = 0 \quad \text{on the wall} \tag{3.45}$$

which will be applied in equation (3.37).

3.5.3 Partial Cell Treatment

The wall boundary conditions described before are usually applied to the outer boundary of computational domain. In some cases, the solid obstacles are inside the computational domain, and the partial cell treatment can be used to treat the

solid region as part of the computational domain. Let f_s be the volume fraction of solid material in each cell, and an effective cell volume is define as:

$$V_{eff} = (1 - f_s)V \tag{3.46}$$

where V is the original cell volume. Then the cell volume V used in the flow equations will be replaced by the effective cell volume. If the cell is fully occupied by the solid material, there is no need to solve the flow equation in that cell, and the face velocity is assigned zero value.

Consider a cell containing both solid and fluid, its cell face is labeled as either "open" or "closed". A cell face is "closed" if at least one of its neighbor cells is fully occupied by solid materials. Otherwise, the cell face is "open", and the face velocity and pressure are solved by projection method in previous section.

3.5.4 Moving Solid Boundary

Moving solid boundary is usually seen in the wave problems, such as small rolling rocks under surface waves, landslides, and wave maker in the laboratory wave tank. It can be treated as outer boundary if the mesh is regenerated at each time step to fit the new location of the moving boundary. However, this approach is quite expensive in computational cost. In the present study, the mesh is fixed, therefore a moving solid algorithm is introduced to approximate the moving solid boundary. It was first introduced by Heinrich in a 2D landslide problem, and Wu [78] extended it to 3D landslide problem.

The partial cell treatment in section 3.5.3 will be used to deal with the solid region. And an internal source function is added to the original continuity equation to model the movement of the solid material. Consider a control volume Ω

containing a moving solid obstacle with a volume V_s and bounded surface A_s. The mass conservation in the control volume is

$$\frac{1}{V}\frac{dV_s}{dt}\int_\Omega \nabla\cdot\mathbf{u}dV = \frac{1}{V}\frac{dV_s}{dt} = \phi(\mathbf{x},t) \tag{3.47}$$

where ϕ denotes an internal source function. Therefore, the governing equations (2.1) and (2.2) become:

$$\nabla\cdot\mathbf{u} = 0 \tag{3.48}$$

$$\frac{\partial(\rho\mathbf{u})}{\partial t} + \nabla\cdot(\rho\mathbf{u}\mathbf{u}) = -\nabla p + \nabla\cdot\tau + \rho\mathbf{g} + \rho\mathbf{u}\phi \tag{3.49}$$

more details can be found in [78].

3.5.5 Dirichlet Pressure Boundary

In the numerical wave simulation, the top of the computational domain is usually occupied by pure air, and the outer boundary of this region is assumed to be atmospheric pressure, $p_0 = 0$. Since the pressure is prescribed on the boundary, the pressure increment in PPE is always zero:

$$\delta p = 0 \quad \text{on Dirichlet pressure boundary} \tag{3.50}$$

and the normal pressure gradient at the boundary is approximated by a one-side interpolation scheme. The velocity on the boundary is part of the flow solution and the value from previous time step will be used to calculate the momentum advection and diffusion in the new time step.

3.5.6 Free Surface Boundary

In this study, we mainly deal with the air-water interface, i.e. free surface. This section will discuss the numerical implementation of free surface boundary condition described in Chapter 2.

In the VOF model, the VOF function f_k defines the presence of fluid k in the computational cell. In the limit of zero mesh space, it is a Heaviside function:

$$f_k = \begin{cases} 0, & \text{outside fluid}k \\ 1, & \text{inside fluid}k \end{cases} \tag{3.51}$$

thus the VOF equation (3.13) describes the kinematic interface boundary condition (2.5).

In practice, there is not a sharp interface. Instead, the interface spreads over a finite width of the order of mesh spacing, which hinders the direct application of the dynamic interface boundary condition (2.6). Nichols and Hirt [54] reported that fictitious oscillation on free surface happens when applying (2.6). They proposed a simplified dynamic free surface boundary condition that ignores the stress from the air side and the shear stress on the water side. The dynamic free surface boundary condition is simply replaced by setting the pressure on the free surface to zero:

$$p = 0 \quad \text{on the free surface} \tag{3.52}$$

Nichols and Hirt reported that this simplified boundary condition produced rather satisfactory results when the grid size near the free surface does not resolve the free surface boundary layer. In fact, with the introduction of one-field model, all fluids within a cell move with the same velocity, which implies zero shear stress and velocity gradient at the reconstructed interface.

3.5.7 Incident Wave Boundary

The incident wave boundary is usually a Dirichlet boundary where the velocity $\mathbf{u}_{in}$ and free surface elevation η_{in} are prescribed. And the volume fluxes of water and air across the boundary can then be calculated.

3.5.8 Outflow Boundary

In order to let the wave leave the Computational domain without or with very little reflection from the boundary, the advective open boundary condition or a more general numerical sponge layer technique can be employed.

Advective Open Boundary

Replacing ϕ in equation (2.8) by VOF function f or velocity $\mathbf{u}$ at the boundary, we have

$$f_{k,out}^{n+1} = f_{k,out}^{n+1} + C_g \Delta t \frac{\Delta f_{k,out}^{n}}{\Delta x} \tag{3.53}$$

and

$$\mathbf{u}_{k,out}^{n+1} = \mathbf{u}_{k,out}^{n+1} + C_g \Delta t \frac{\Delta \mathbf{u}_{k,out}^{n}}{\Delta x} \tag{3.54}$$

assuming the advective open boundary is vertical which is usually true in practice. x is the streamwise direction. C_g is the group velocity. For long waves, $C_g = \sqrt{g(h+\eta)}$. However, the group velocity of outgoing short waves is not known a priori because they are part of the flow solution, therefore advective open boundary only applies to long waves.

Numerical Sponge Layer

The numerical sponge layer is a region with so strong artificial damping effects that the wave energy within is completely damped out. This idea was first proposed by Larsen and Dancy [34], and was developed to work with VOF algorithm by Troch and De Rouck [72]. The velocity field is gradually reduced by multiplying an absorption function $b(x)$. And we adopt the absorption function suggested by Troch and De Rouck [72] that would produce little wave reflection:

$$b(x) = \sqrt{1 - \left(\frac{x - x_0}{L_s}\right)} \tag{3.55}$$

where x_0 and L_s are the starting position and length of the numerical sponge layer, respectively. Wu [78] suggested that multiplying only the vertical velocity component u_z by the absorption function gives the least amount of reflecting waves. The length of the sponge layer should be at least one wave length λ. In practice, L_s is usually chosen as:

$$\lambda < L_s < 1.5\lambda \tag{3.56}$$

Therefore, longer waves require longer sponge layer which is computational expensive. However, the solution within the sponge layer is not our interest, thus a very coarse mesh can be used in the region, which helps reduce the computational cost.

3.6 Error Analysis and Numerical Stability

3.6.1 Error Analysis

Numerical fluid flow solutions are always approximates of the exact flow solutions. The difference can be termed as the errors. In general, the errors fall into four categories: modeling errors, discretization errors, round-off errors, and iterative convergence errors.

Modeling errors stem from the assumptions made in the mathematical formulation of the real flow and its boundary conditions, so it is also called physical approximation error. The modeling error can be estimated by comparing the exact or highly accurate solution of the physical equations with the accurate laboratory measurements, which is off the topic of present study. For readers who are interested, Mehta [48, 49] had a detailed discussion on the sources of modeling errors.

Discretization errors come from the discrete algebraic expression of the exact PDE equation on a discretized flow domain of time and space, and they are also called numerical errors in the literature. Discretization errors are usually the principal source of errors in computational fluid dynamics. The discretization error is associated with the term "grid-independent solution", i.e. the solutions show little difference when refining the coarser mesh. We have not carried out any research on the grid-independent solution due to the limitation of computational resources. However, the computational experience of our group [39, 41, 78] shows that the current choice of grid size can render satisfactory results.

Discretization errors can be evaluated mathematically on uniform orthogonal structured mesh. However, it is rather difficult to do so on general unstructured mesh. A common practice is to use the results from the uniform orthogonal structured mesh as a rough estimate. For the discretization scheme we used in this study, the time derivative is first-order accurate in time, the momentum advection term is first-order accurate in space, and the momentum diffusion and pressure gradient terms are second-order accurate in space. Therefore, the discretization error of the momentum advection term is the leading part of the discretization error.

Consider the x-component of the advection term in a $x-y-z$ Cartesian coordinate system:

$$F_x = u\frac{\partial u}{\partial x} + v\frac{\partial u}{\partial y} + w\frac{\partial u}{\partial z} \tag{3.57}$$

The leading error of truncation error can be easily obtained from the Taylor series expansion:

$$\begin{aligned} TE_x =& \frac{1}{2}\left(|u|\Delta x - |u|^2\Delta t\right)\frac{\partial^2 u}{\partial x^2} \\ &+ \frac{1}{2}\left(|v|\Delta y - |v|^2\Delta t\right)\frac{\partial^2 u}{\partial y^2} \\ &+ \frac{1}{2}\left(|w|\Delta x - |w|^2\Delta t\right)\frac{\partial^2 u}{\partial x^2} \end{aligned} \tag{3.58}$$

and we obtain TE_y and TE_z in a similar way. Equation (3.58) shows that the truncation error functions in a way like the momentum diffusion, thus it is often referred to as numerical dissipation or numerical diffusion. And the numerical viscosity can be defined as:

$$\begin{aligned} \nu_{num,xx} &= \frac{1}{2}\left(|u|\Delta x - |u|^2\right) \\ \nu_{num,yy} &= \frac{1}{2}\left(|v|\Delta x - |v|^2\right) \\ \nu_{num,zz} &= \frac{1}{2}\left(|w|\Delta x - |w|^2\right) \end{aligned} \tag{3.59}$$

The numerical viscosity is usually at least one order of magnitude lower than the turbulent viscosity when turbulent-viscosity hypothesis model is used to model the turbulent effect [39, 78]. Therefore, the flow solution is not contaminated by the discretization errors.

Round-off errors are attributed to the representation of floating point numbers on the computer and the computer precision at which the numbers are stored. Round-off errors are often considered trivial on modern high speed computers.

Iterative convergence errors arise because the iterative methods used in the flow simulation must stop at some point eventually. The stopping criteria should be at least one order of magnitude smaller than the discretization errors. In this study, we choose the stopping criteria to be 10^{-12} which is small enough to ignore the iterative convergence error.

3.6.2 Stability Analysis

For a linear PDE system, the von Neumann stability analysis (also known as Fourier stability analysis) [6, 29] is widely used to analyze the stability of numerical methods. This method first introduces an initial error which is decomposed in a series of Fourier modes, then substitute it into the discretized equation to obtain the error evolution equation. If the initial error does not grow, i.e. the amplification factor of each Fourier mode is always smaller than unity, then the numerical method is said to be stable. A stable numerical scheme guarantees a bounded solution whenever the solution of exact PDE is bounded. And by virtue of Lax equivalence theorem [29, 70], a stable numerical scheme is also

convergent. The stability condition is often expressed as a constraint on the time step for unsteady partial differential equation.

With the existence of nonlinear advection terms in momentum equation, the convectional von Neumann analysis is not applicable unless the nonlinear terms are linearized. In practice, a constant maximum velocity $\max(|\mathbf{u}|)$ and maximum effective viscosity $\max(\nu_{eff})$ are used to linearize the advection and diffusion terms, and the von Neumann stability analysis gives that

$$\delta t_c < C_r \frac{\Delta}{\max(|\mathbf{u}|)} \tag{3.60}$$

$$\delta t_\mu < V_\mu \frac{\Delta^2}{\max(\nu_{eff})} \tag{3.61}$$

where δt is the time step and its subscript c and μ indicate Courant number constraint and viscous number constraint on the time step; C_r is the Courant number, V_μ is the viscous number and Δ is the characteristic grid size. For the stability of numerical scheme, C_r should be less than unity, and the viscous number $V\mu$ should be 1/2, 1/4 and 1/6 in 1D, 2D and 3D meshes, respectively. In this study, we choose $C_r = 0.5$, and it was found that the time step is always controlled by the Courant number condition (also called CFL condition [10]).

3.7 Model Tests

3.7.1 Solitary Waves in Constant Water Depth

Solitary wave propagation in constant water depth is a classical benchmark problems for numerical wave model test. It propagates without the change of

form in constant water depth over a flat bottom. And different analytical theories are already developed for the solitary wave. Therefore, it is well suited to evaluate the numerical accuracy of the numerical model. For example, by checking the free surface location, the quality of volume tracking algorithm can be evaluated. By checking the balance of mass and energy, the conservation of the numerical scheme can be evaluated.

In the numerical simulation, the free surface elevation and velocity distribution prescribed on the incident wave boundary are calculated by third-order Grimshaw solitary wave solution [24, 35]:

$$\eta(x,t) = h\left[\epsilon s^2 - \frac{3}{4}\epsilon^2 s^2 q^2 + \epsilon^3\left(\frac{5}{8}s^2q^2 - \frac{101}{58}s^4q^2\right)\right] \tag{3.62}$$

where $\epsilon = H/h$; H is the wave height; h is the still water depth; $s = \operatorname{sech}\alpha X/h$; $q = \tanh\alpha X/h$; $X = x - Ct$ in which C is the wave speed; the coefficient α:

$$\alpha = \left(\frac{3}{4}\epsilon\right)^{1/2}\left(1 - \frac{5}{8}\epsilon + \frac{71}{128}\epsilon^2\right)$$

and the wave speed C is:

$$C = \sqrt{gh}\left(1 + \epsilon - \frac{1}{20}\epsilon^2 - \frac{3}{70}\epsilon^3\right)^{1/2} \tag{3.63}$$

and the velocity distribution is:

$$\begin{aligned}\frac{u}{\sqrt{gh}} = {} & \epsilon s^2 - \epsilon^2\left[-\frac{1}{4}s^2 + s^4 + \left(\frac{z}{h}\right)^2\left(\frac{3}{2}s^2 - \frac{9}{4}s^4\right)\right] \\ & - \epsilon^3\left[\frac{19}{40}s^2 + \frac{1}{5}s^4 - \frac{6}{5}s^6 + \left(\frac{z}{h}\right)^2\left(-\frac{3}{2}s^2 - \frac{15}{4}s^4 + \frac{15}{2}s^6\right)\right. \\ & \left. + \left(\frac{z}{h}\right)^4\left(-\frac{3}{8}s^2 + \frac{45}{16}s^4 - \frac{45}{16}s^6\right)\right]\end{aligned} \tag{3.64}$$

$$\begin{aligned}\frac{w}{\sqrt{gh}} = {} & (3\epsilon)^{1/2}\left(\frac{z}{h}\right)q\left\{-\epsilon s^2 + \epsilon^2\left[\frac{3}{8}s^2 + 2s^4 + \left(\frac{z}{h}\right)^2\left(\frac{1}{2}s^2 - \frac{3}{2}s^4\right)\right]\right. \\ & + \epsilon^3\left[\frac{49}{640}s^2 - \frac{17}{29}s^4 - \frac{18}{5}s^6 + \left(\frac{z}{h}\right)^2\left(-\frac{13}{6}s^2 - \frac{25}{16}s^4 + \frac{15}{2}s^6\right)\right. \\ & \left.\left. + \left(\frac{z}{h}\right)^4\left(-\frac{3}{40}s^2 + \frac{9}{8}s^4 - \frac{27}{16}s^6\right)\right]\right\}\end{aligned} \tag{3.65}$$

The coordinate system is defined in Figure 3.3. The Grimshaw solution is well

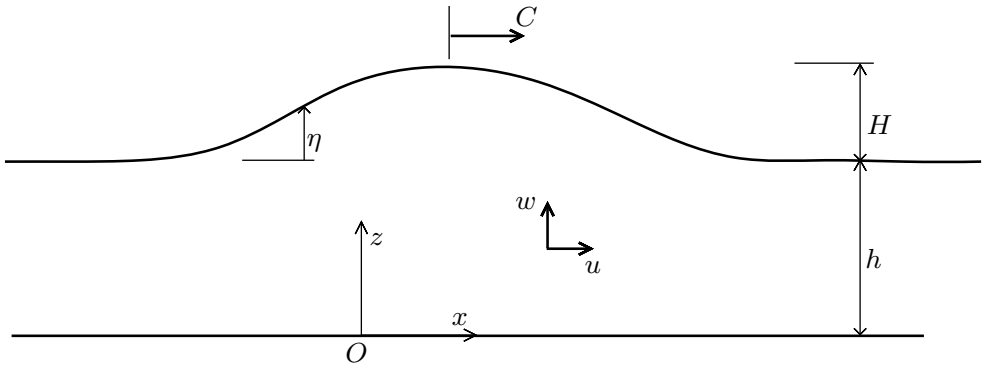

Figure 3.3: Solitary Wave Sketch

suited for solitary wave of $\epsilon < 0.5$. For small amplitude solitary wave ($\epsilon < 0.25$), the Boussinesq solution [35, 78] can be used:

$$\eta(x,t) = H\left[\text{sech}\,\sqrt{\frac{3}{4}\frac{H}{h}}\frac{X}{h}\right]^2 \tag{3.66}$$

$$\frac{u}{\sqrt{gh}} = \left\{\epsilon + 3\epsilon^2\left[\frac{1}{6} - \frac{1}{2}\left(\frac{z}{h}\right)^2\right]\right\}\frac{\eta}{H} - \epsilon^2\left[\frac{7}{4} - \frac{9}{4}\left(\frac{z}{h}\right)^2\right]\left(\frac{\eta}{H}\right)^2 \tag{3.67}$$

$$\frac{w}{\sqrt{gh}} = \sqrt{3\epsilon}\frac{z}{h}\frac{\eta}{h}\tanh\left(\sqrt{\frac{3\epsilon}{4}}\frac{X}{h}\right)\left\{1 + \frac{1}{2}\epsilon\left[1 - \frac{7\eta}{H} - \left(\frac{z}{h}\right)^2 1 - \frac{3\eta}{H}\right]\right\} \tag{3.68}$$

Two solitary waves are simulated to be compared with the analytical theory, as listed in Table 3.1. Here we only show the results of test case 2, with the still water depth $h = 1.0\,\text{m}$ and $\epsilon = H/h = 0.3$.

The computational domain is $60h$ in the streamwise direction x, $1.48h$ in the vertical direction z, and $0.25h$ in the spanwise direction. The mesh is orthogonal. In the streamwise direction, 2400 cells with uniform grid size $\Delta x/h = 0.025$ are used, while we use 3 cells with uniform grid size $\Delta y/h = 0.083$ in the spanwise direction. The grid in the vertical direction is non-uniform with the finest grid size $\Delta z/h = 0.0066$ on the top, giving 85 cells. The Euler's equations will be

Table 3.1: Parameters of solitary waves. h is the still water depth, H the wave height, $\epsilon = H/h$ the wave steepness, and C the phase speed.

Test case	ϵ	h(m)	H(m)	C(m/s)
1	0.1	1.0	0.1	3.28
2	0.30	1.0	0.3	3.57

solved since there is little turlence in the flow. The incident wave boundary is at $x/h = 0$, and the top boundary is zero pressure Dirichlet boundary. Other boundaries are free-slip wall boundary. The surface tension is neglected in the calculation. The time step is dynamically determined by the stability condition, i.e., the Courant number condition (3.60) with $Cr = 0.5$.

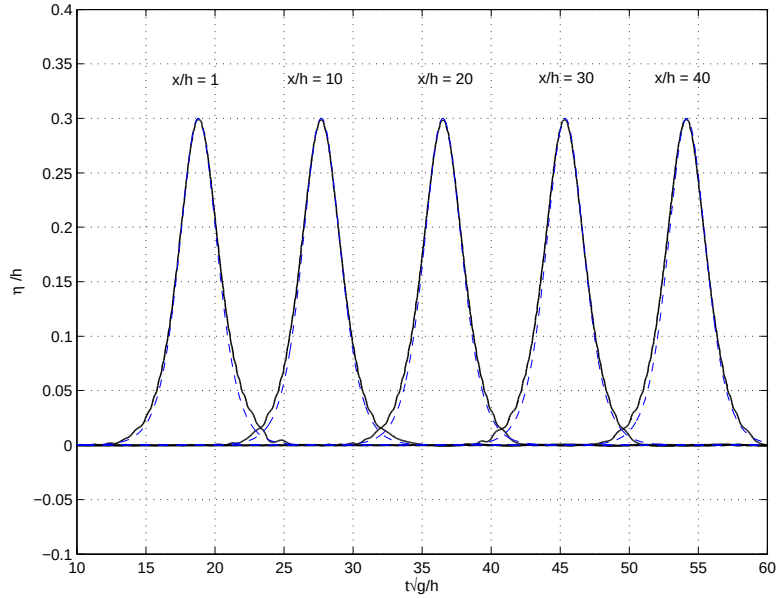

Figure 3.4: Free surface elevation history at different locations. Dash line denotes the analytical solitary wave profile.

Figure 3.4 presents the solitary wave profiles at the cross-section of $y/h = 0.125$. The surface elevations are measured at five numerical gauges. As it shows, the numerical solitary wave of $H/h = 0.3$ fit rather well with the ana-

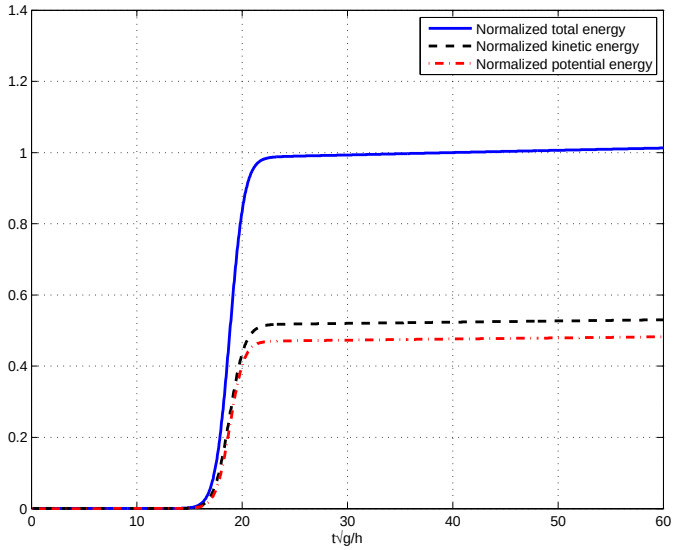

Figure 3.5: Normalized energy history of solitary wave. The energy was normalized by the calculated total energy at $t\sqrt{g/h} = 40$. Solid line: total energy; dash line: kinetic energy; dash-dot line: potential energy.

lytical shape, and it moves without the change of shape at a constant phase speed $C = 3.55\text{m/s}$. The numerical error for the phase speed is 0.56%. Therefore, the numerical model captures the free surface with a satisfactory accuracy and accurately simulates the wave kinematics.

Since the analytical theory for solitary wave is non-dissipative, the mass and energy should be conserved in the computational domain when there are no mass flux through the boundaries. The kinetic energy, the potential energy and the total energy are summed cell by cell over the whole computational domain:

$$E_k = \frac{1}{2}\sum \rho f V(u^2 + v^2 + w^2) \tag{3.69}$$

$$E_p = \sum \rho f V g z \tag{3.70}$$

$$E_t = E_k + E_p \tag{3.71}$$

where V is the cell volume, f the VOF value of water in the cell. Here we choose

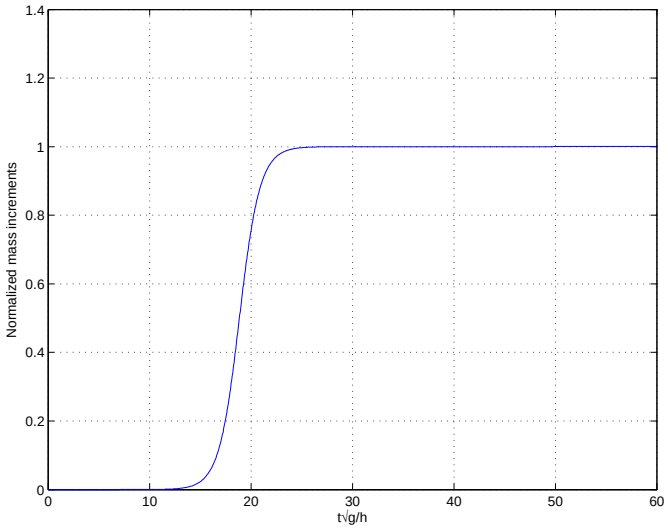

Figure 3.6: Normalized mass history of solitary wave. The mass was normalized by the calculated mass at $t\sqrt{g/h} = 40$

the bottom $z = 0$ as the reference level for the calculation of potential energy. Figure 3.5 and 3.6 show the normalized energy and mass histories, respectively. The mass and energy increase as the solitary wave moves into the computational domain, and then keep almost unchanged when the whole solitary wave travels in the channel. Thus the mass and energy are conserved as the wave travels a distance of $60h$ during the computations. This numerical test shows the excellent capacity of our numerical code to simulate the relative high nonlinear solitary wave ($H/h = 0.3$ here).

3.7.2 Intermediate-depth Periodic Waves in Constant Water Depth

Another test case could be periodic waves which are very common in coastal problems. In this numerical test, an intermediate-depth periodic wave is nu-

merically simulated in a constant water depth. The wave parameters are listed in Table 3.2.

Table 3.2: Numerical wave parameters. h is the still water depth, H the wave crest-to-trough height, T the wave period, λ the wave length, $k = 2\pi/\lambda$ the wave number, and $A = H/2$ the wave amplitude.

h	H	T	λ	kh	kA
4.77 m	1.35 m	6.0 sec	38.0 m	0.79	0.11

Fenton [16] suggested the use of the Stokes wave theory if

$$\frac{\lambda}{h \cdot \exp^{-1.87H/h}} - 21.5 < 0 \tag{3.72}$$

otherwise the cnoidal wave theory is recommended for shallow water wave. The wave parameters of our numerical wave indicates that the Stokes wave theory should be used. In Stokes wave theory, all variations in the streamwise direction are assumed to be expressed by Fourier series. In stead of calculating the Fourier coefficients as some perturbation expansions, our numerical code implemented the Fourier approximation method proposed by Fenton [15], which determines the values of Fourier coefficients by numerically solving a system of nonlinear equations. Therefore, the free surface elevation and velocities prescribed at the incident boundary are given by:

$$\eta = \frac{1}{k}\left[\sum_{j=1}^{N} Y_j \cos jk(x - Ct)\right] \tag{3.73}$$

$$u = \frac{1}{\sqrt{k/g}}\left[C\sqrt{k/g} - u\sqrt{k/g} + \sum_{j=1}^{N} jB_j \frac{\cosh jkz}{\cosh jkh} \cos jk(x - Ct)\right] \tag{3.74}$$

$$w = \frac{1}{\sqrt{k/g}}\left[\sum_{j=1}^{N} jB_j \frac{\sinh jkz}{\cosh jkh} \sin jk(x - Ct)\right] \tag{3.75}$$

where the coefficients Y_j, B_j are calculated by Fourier approximation method, $N = 9$ in our simulation. The coordinate system is denoted in Figure 3.3.

The computational domain is 3.34λ in the streamwise direction x, 0.0158λ in the spanwise direction y, and $1.26h$ in the vertical direction z. The mesh is orthogonal. In the streamwise direction, the grid is uniform except in the numerical sponge layer region which starts at $x/\lambda = 1.76$. The grid size is $\Delta x/\lambda = 0.0053$. The spanwise grid is also uniform using the same size of Δx. In the vertical direction, the grid is nonuniform with the smallest grid size $\Delta z/h = 0.0105$ on the top and largest grid size $\Delta z/h = 0.021$ on the bottom. The Euler's equation will be solved since the flow is irrotational. The incident wave boundary is located at $x/\lambda = 0$, and the top boundary is zero pressure Dirichlet boundary. A numerical sponge layer of length $L_s/\lambda = 1.57$ is used to damp the outgoing wave train. Other boundaries are free-slip wall boundary. Since the wave is uniform in spanwise direction, it is essentially a two dimensional flow but simulated in three dimensional domain. The numerical solution presented below is at the cross-section of $y/\lambda = 0.008$.

Figure 3.7– 3.9 present the comparison between numerical and laboratory data. The laboratory experiment was carried out by the Coastal Research Center (FZK) in Hannover, Germany. More details about the experiments can be found in [51]. The numerical solution agrees very well with the laboratory data in terms of free surface elevation and velocities. Figure 3.10 shows the numerical wave profiles at different locations. The numerical wave keeps its phase very well. It is also clear that the numerical sponge layer suppresses the outgoing wave train very well, generating little wave reflections.

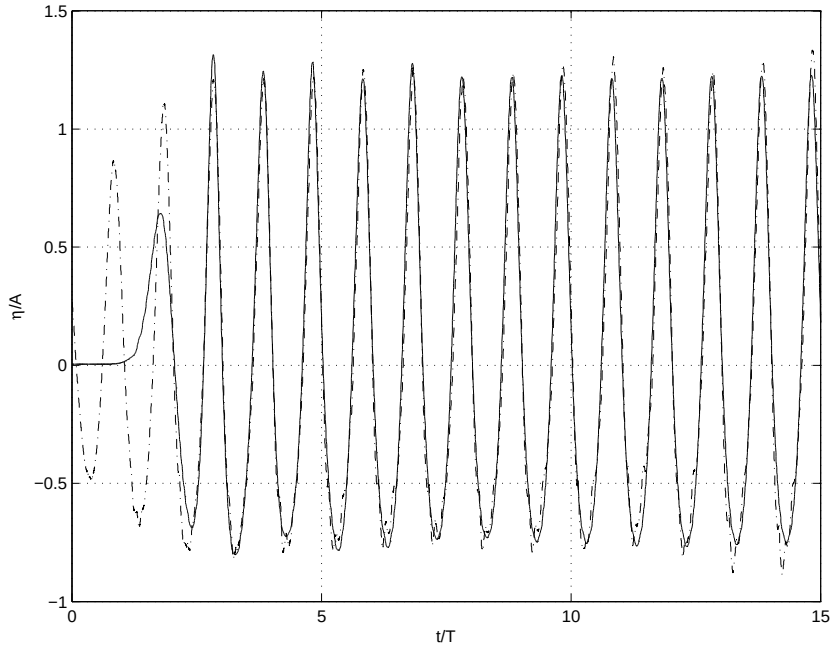

Figure 3.7: Numerical and laboratory wave profiles at the location x/λ = 1.57. Solid line: numerical; dash-dot line:laboratory.

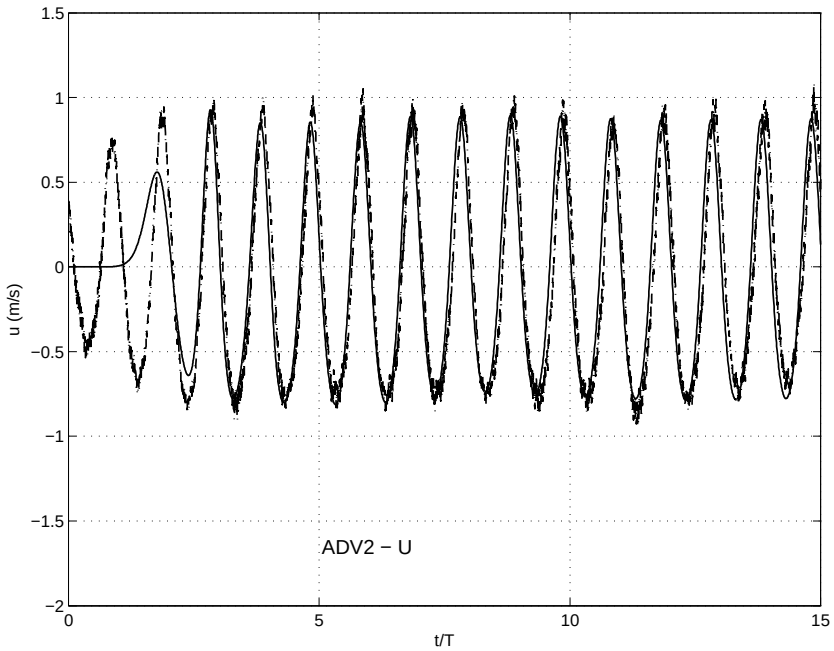

Figure 3.8: Horizontal velocity history at z/h = 0.55. Solid line: numerical; dash-dot line: laboratory.

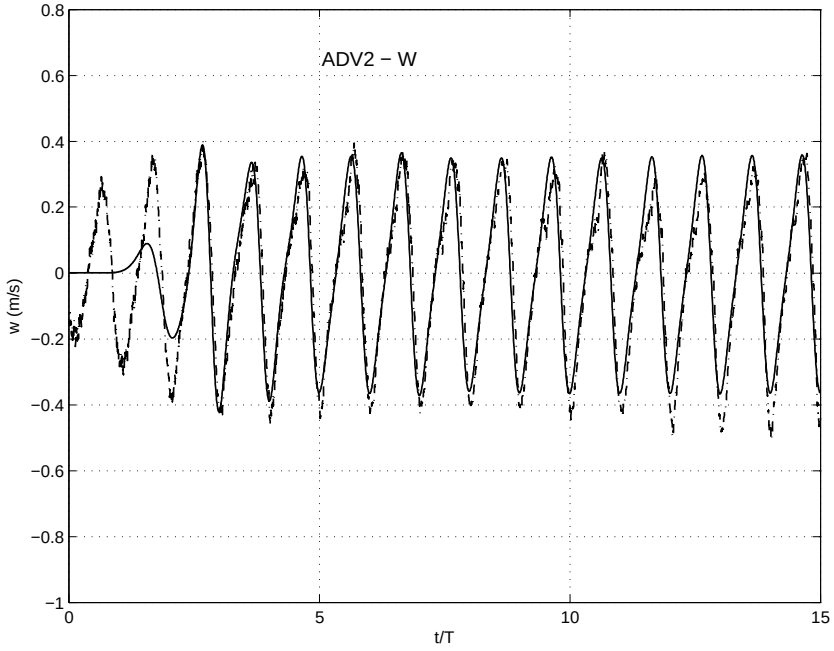

Figure 3.9: Vertical velocity history at $z/h = 0.55$. Solid line: numerical; dash-dot line: laboratory.

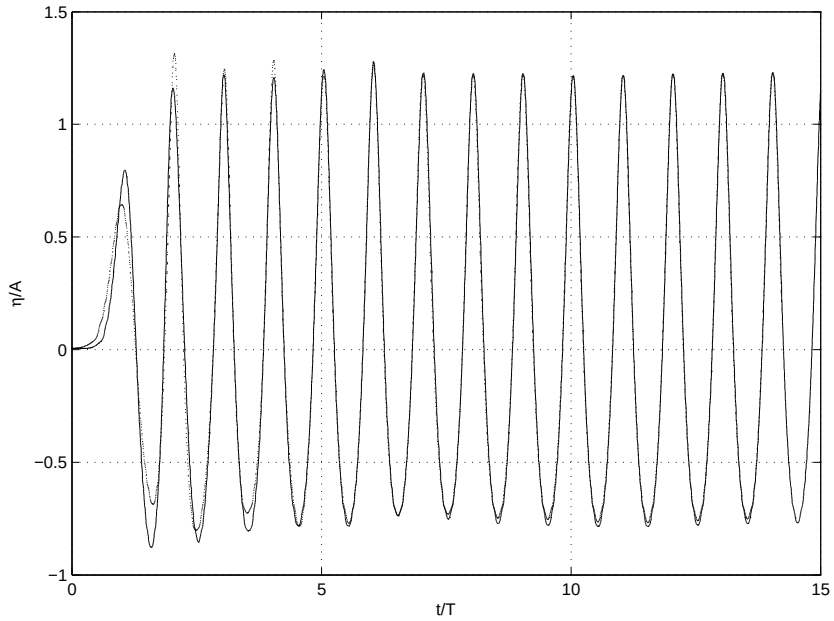

Figure 3.10: Numerical wave profiles at the location $x/\lambda = 0.79$ (solid line)and $x/\lambda = 1.57$ (dash-dot line). The curve at $x/\lambda = 1.57$ is shifted to faciliate comparison.

3.8 Concluding Remarks

In this chapter, the details of our numerical model are discussed. The numerical model has the following features:

- Unstructured irregular mesh to partition the complex geometric topology.
- Numerical calculation of three dimensional flow of incompressible fluids with large density ratios.
- Two-step projection method implemented in a finite volume algorithm.
- Multi-dimensional PLIC (Piecewise linear interface calculation) volume tracking algorithm to capture the air-water interface.
- Solid obstacles can be represented by a partial cell treatment.
- Moving solid algorithm for moving boundary problem.
- Nonlinear wave generation - solitary wave, cnoidal wave and Stokes wave etc.
- Effective wave absorption.
- Large eddy sub-grid turbulence model.
- Parallel computation utilizing multiple computer processors.

Solitary wave and periodic wave propagating in constant water depth over a flat bottom are simulated to check the performance of numerical model. The numerical results are compared with analytical theory or laboratory measurements. We found that the numerical model gives satisfactory results for the wave kinematics, such as the free surface displacement, phase speed and fluid velocity. Therefore, we can conclude that the numerical model provides a solid

framework to study the wave impact on the coastal structures and the breaking wave on a sloping beach.

CHAPTER 4

NUMERICAL INVESTIGATION OF NON-BREAKING SOLITARY WAVE INTERACTION WITH SLENDER CYLINDERS ON FLAT BOTTOM

Tsunami is one of the major hazards in coastal region. It can be generated by earthquakes, landslides, and volcano eruptions. As the wave propagate shoreward with little energy dissipation, the run-up at the shoreline and its impact force on a coastal structure are usually of the most interests in the evaluation of tsunami hazard.

To better understand the interaction between tsunami and coastal structures, we have developed a three-dimensional numerical model to simulate a solitary wave impinging on a group of slender cylinders. The wave amplitude and still water depth vary over a wide range, and there are several cylinder arrangements.

The numerical model solves Euler's equation without any dissipative mechanism, since the available experimental data are for non-breaking solitary waves. The laboratory data sets contain large-scale measurements of the water surface elevation, the fluid particle velocity, the pressure at different locations around the circumference of the cylinders and total wave forces. Numerical results are compared with the experimental data, and numerical simulations over a wide range of wave parameters were carried out to fully understand the solitary wave structure interaction.

4.1 Introduction

Tsunamis have long been a major ocean hazard in the Pacific Basin. The 1896 tsunami attacking Sanriku, Japan took away more than 27,000 lives and destroyed over 10,000 buildings. The December 2004 tsunami caused by an earthquake in the Indian ocean have recently drawn the world's strong interest in tsunami and its mitigation effort.

Solitary waves or N-waves are often used to model the leading waves of tsunamis [42, 71]. Researchers have been using solitary waves for decades to study tsunami problems such as run-up and inundation analytically, numerically and experimentally.

Vertical cylinders are among the most commonly used structures in coastal and offshore engineering. In the near-shore region they are used for jetties or piers and in deep water for offshore platforms and windmill farms. In practical problems, the structures, especially offshore structures in deep ocean region, can be flexible, dynamically response with the ambient waves. In this study, the cylinders are instead rigid and fixed on the bottom, which are commonly seen in near shore region (the water depth can be up to 500m).

In designing these structures, it is critical to be able to calculate wave forces acting on each individually cylinder and, in some cases, a group of cylinders. For a slender cylinder, where the diameter of the cylinder (D) is small in comparison with the design wave length (λ), the Morison formula [52] is a good approximation for calculating the wave forces:

$$F_H = \int_0^{h+\eta} \left(\frac{1}{2} \rho C_D D |u| u \right) dz + \int_0^{h+\eta} \left(\rho C_M V_0 \frac{\partial u}{\partial t} \right) dz \tag{4.1}$$

where C_D and C_M are force coefficients, ρ is the water density, u is the horizontal

particle velocity, D is the cylinder size, and V_0 is the water volume occupied by the cylinder. In general, the drag and mass coefficients (C_D and C_M) must be determined based on the experimental data or numerical simulations.

By dimensional analysis, the wave force exerted on the structure can be expressed as:

$$\frac{F}{\rho u_m^2 D\lambda} = f\left(\frac{u_m T}{D}, \frac{u_m D}{\nu}, \frac{\Delta}{D}, \frac{t}{T}\right) \tag{4.2}$$

where u_m is the maximum horizontal particle velocity, D is the characteristic size of the cylinder, λ is the wave length, T is the wave period, and Δ is the roughness of the cylinder surface. The force coefficients are therefore expressed as functions of Keulegen-Carpenter number $Kc = u_m T/D$, Reynolds number $Re_D = u_m D/\nu$ and the relative roughness Δ/D since they are assumed to be time independent. In this study, the relative roughness is ignored.

For a solitary wave, the question always exists which wave length λ and wave period T should be used. Theoretically, we can express the solitary wave as some functions of the wave steepness H/h, as seen in equations (3.62)– (3.68):

$$u_m = \sqrt{gh} f_1(H/h) \tag{4.3}$$

$$\lambda = h f_2(H/h) \tag{4.4}$$

$$T = \sqrt{h/g} f_3(H/h) \tag{4.5}$$

therefore, the wave force relation (4.2) can be rewritten for a solitary wave as:

$$\frac{F}{\rho g D^3} = f\left(\frac{H}{h}, \frac{h}{D}, Re_D, \frac{t}{\sqrt{h/g}}\right) \tag{4.6}$$

The present study concerns non-breaking solitary wave impinging on a group of slender vertical rigid cylinders. The computational results are compared with the experimental data in terms of water surface elevation, fluid particle velocity, wave forces and etc. The agreements are overall good. It is not

always feasible to perform extensive parameter studies in laboratory experiments, therefore the numerical model is then used to simulate scenarios with much wider range of physical parameters of interest.

4.2 Governing Equations

Three-dimensional Euler's equations must be employed to describe rotational flows:

$$\nabla \cdot \mathbf{u} = 0 \tag{4.7}$$

$$\frac{\partial \mathbf{u}}{\partial t} + \nabla \cdot (\mathbf{u}\mathbf{u}) = -\frac{1}{\rho}\nabla p + \mathbf{g} \tag{4.8}$$

where $\mathbf{u}$ represents velocity vector, ρ water density, $\mathbf{g}$ the gravity force vector, t time and p the pressure.

The numerical method is described in Chapter 3. Free-slip wall boundary condition is applied on the wall.

4.3 Laboratory Setup

To check the capability and accuracy of our numerical model, numerical simulations of non-breaking solitary waves and their interaction with a group of three vertical cylinders were conducted and the results were compared with experimental data. The experiments were conducted in the Tsunami Wave Basin at the O. H. Hinsdale Wave Research Laboratory (WRL) of the Oregon State University (OSU).

The wave basin at the WRL of OSU has an effective length of 160 ft (48.8 m), a width of 87 ft (26.5 m) and a depth of 7 ft (2.1 m). Stainless steel circular cylinders with a diameter, D, of 4 ft (1.219 m) were instrumented and installed in the basin.

Three cylinder configurations were examined. The first configuration (C1) is a single cylinder placement (Figure 4.1). The second configuration (C2) is a three-cylinder placement (Figure 4.2): main cylinder with two dummy cylinders (3 diameters from the center to center between the two dummy cylinders). The third configuration (C3) is similar to C2 but with a smaller gap between two dummy cylinders (2 diameters from the center to center between two dummy cylinders) as shown in Figure 4.3.

To measure the wave characteristics, 10 wave gauges and 5 acoustic Doppler Velocimetries (ADVs) were deployed. Their locations are indicated in Figure 4.1, and they are in the same positions in all three cylinder configurations. Additionally, 47 pressure transducers were fixed on the main cylinder, which is farthest from the wave maker. As sketch in Figure 4.4 the pressure transducers are uniformly distributed along the front line of the main cylinder with spacing $\Delta z = 0.1m$ and are also spread out over the circumference in four horizontal cross sections (Figure 4.5 -4.7). The wave forces were measured by the strain gauges installed inside the structural model.

Six sets of experiments were conducted with different wave steepness and still water depth. Three still water levels were used: $h = 0.45m$, $h = 0.60m$, and $h = 0.75m$. The wave height-to-depth ratios H/h vary from 0.2 to 0.6. The numerical simulations only deal with a subset of the experiments, i.e., non-breaking plane solitary waves.

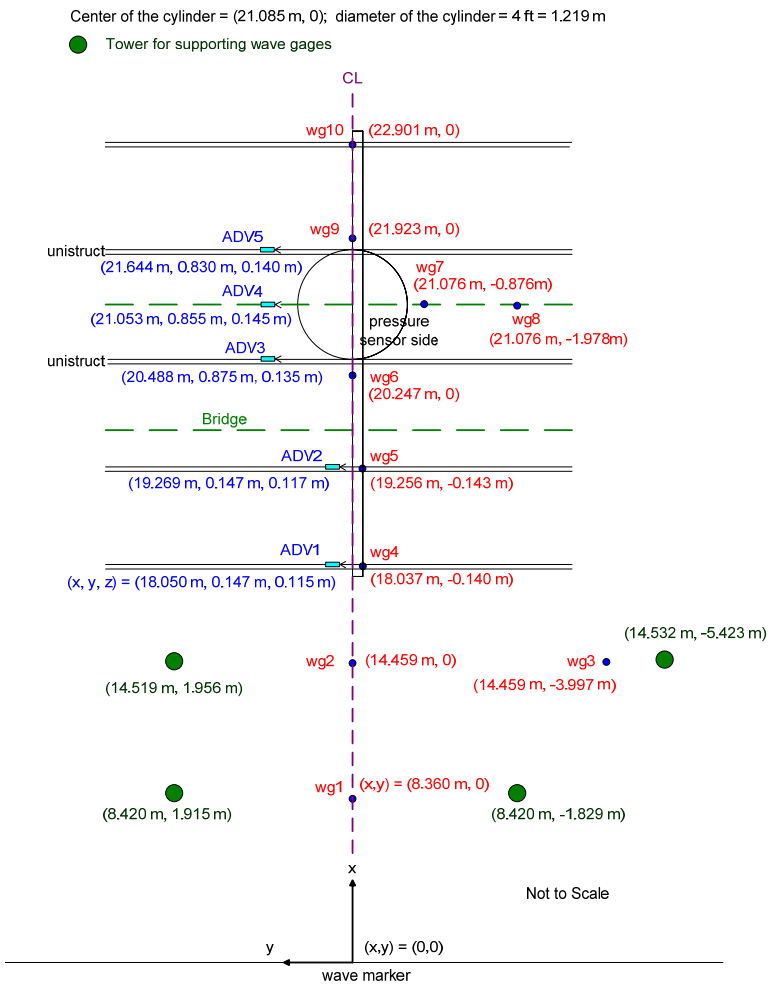

Figure 4.1: C1 sketch of the locations of single cylinder, instruments and wave-maker

In the design of the laboratory experiments, the similarity between the prototype and model must be observed so that the experimental results can be applied to practical problems. For free surface flow with high Reynolds number in this study, gravity similarity criterion should be considered since the gravity is the dominant force that controls the wave propagation. The gravity similarity requires that the Froude numbers of prototype and model flow are equal:

$$\frac{u_p}{\sqrt{gl_p}} = \frac{u_m}{\sqrt{gl_m}} \tag{4.9}$$

where the subscripts p and m denote prototype and model, respectively. And

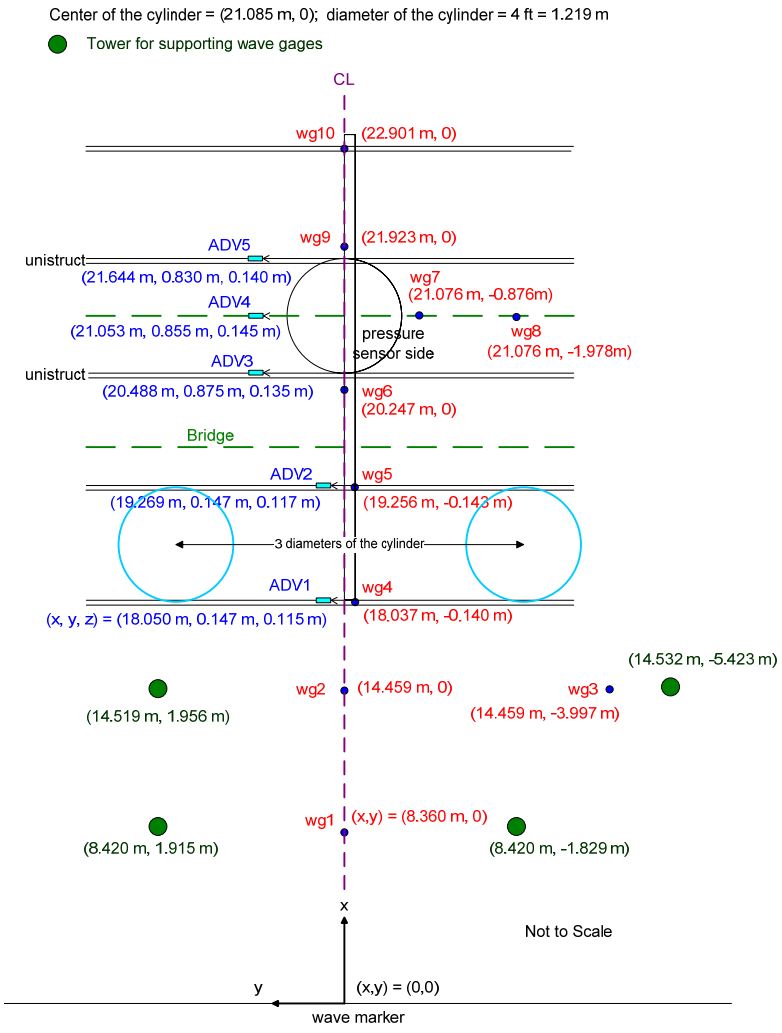

Figure 4.2: C2 sketch of the locations of three cylinders, instruments and wave-maker

we can derive the scales for velocity and force:

$$\lambda_u = \frac{u_p}{u_m} = \frac{\sqrt{l_p}}{\sqrt{l_m}} = \lambda_l^{1/2} \tag{4.10}$$

$$\lambda_F = \frac{F_p}{F_m} = \lambda_l^3 \tag{4.11}$$

here we assume $\rho_p = \rho_m$.

If we choose the diameter of prototype cylinder as 5.0m which is often seen

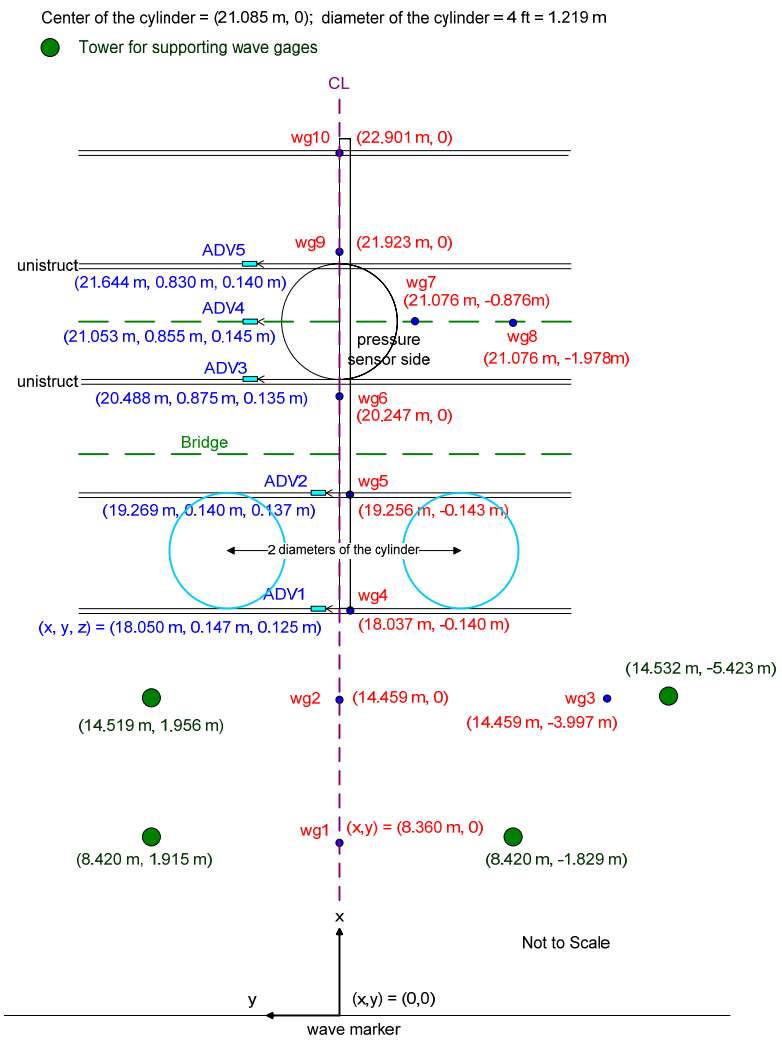

Figure 4.3: C3 sketch of the locations of three cylinders, instruments and wave-maker

in offshore monopile windmill farm, we then have the length ratio:

$$\lambda_l = \frac{5}{1.219} \simeq 4.0 \tag{4.12}$$

and that will give the real wave height and water depth for one set of the laboratory experiments ($H/h = 0.4$ and $h/D = 0.62$) as:

$$h_p = 0.62D = 3.1\text{m} \tag{4.13}$$

$$H_p = 0.4h_p = 1.2\text{m} \tag{4.14}$$

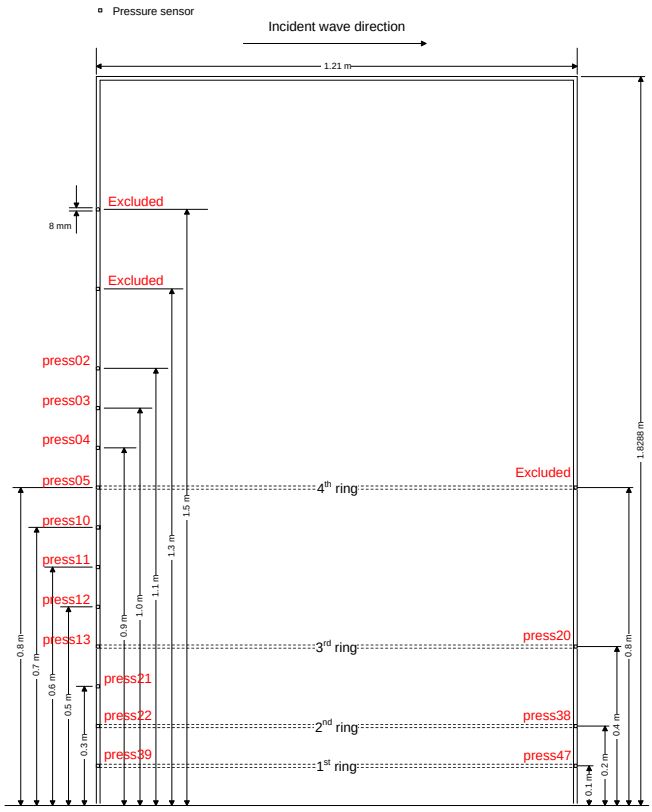

Figure 4.4: A sketch of the locations of pressure transducers on the main cylinder.

which indicates that the wind turbine is quite near the shore. Therefore, the velocity and force in real wave conditions are:

$$u_p = 2u_m \tag{4.15}$$

$$F_p = 64F_m \tag{4.16}$$

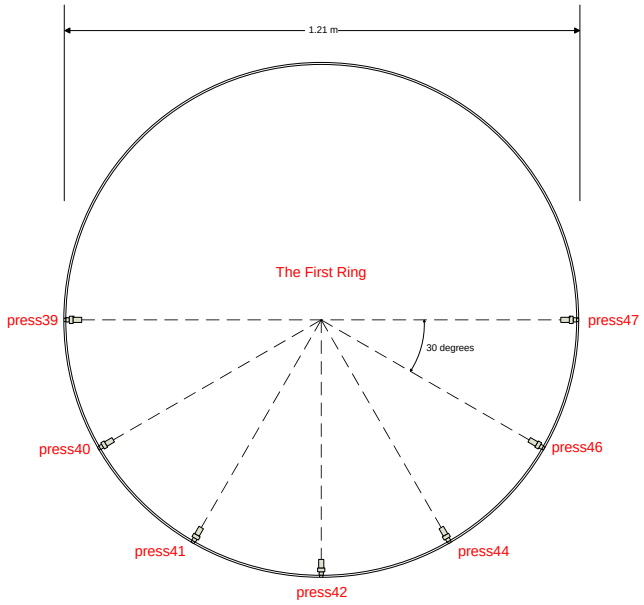

Figure 4.5: The locations of pressure transducers on 1st ring on the main cylinder.

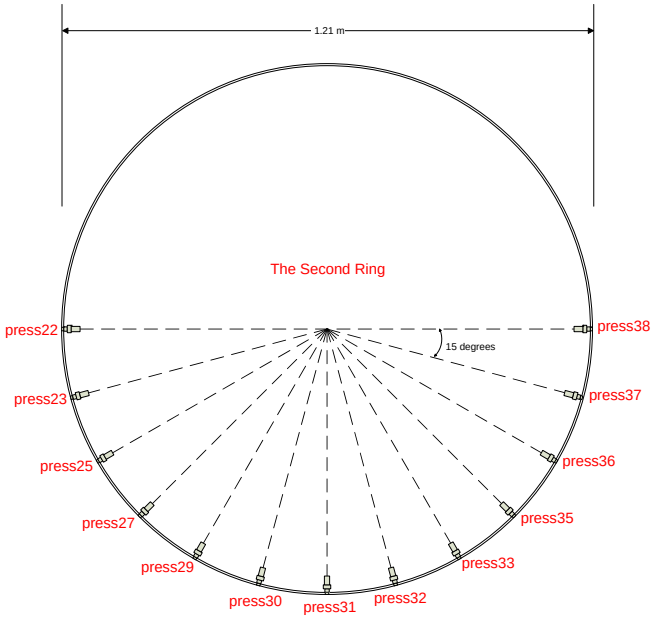

Figure 4.6: The locations of pressure transducers on 2nd ring on the main cylinder.

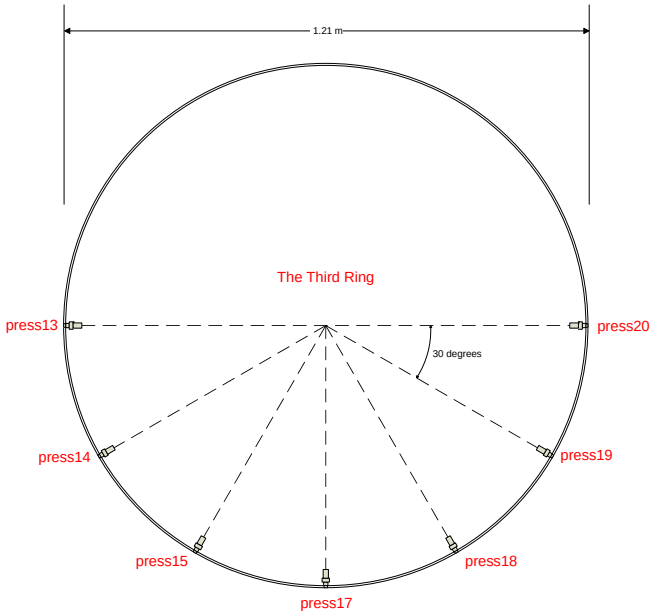

Figure 4.7: The locations of pressure transducers on 3rd ring on the main cylinder.

4.4 Numerical Setup

The numerical simulations were performed only in a half of the wave basin because of the symmetric arrangement of the locations for cylinders and the computational resources constraint. The symmetry can be seen clearly from the laboratory experiment shown in Figure 4.8. One whole-domain numerical simulation of single cylinder case was carried out to make sure that the half domain calculation agrees with the whole-domain calculation, and the results of free surface elevation, particle velocities shows little differences between both cases.

(a) (b)

Figure 4.8: Free surface profile as plane solitary wave passes the cylinder group, $H/h = 0.45$ and $h = 0.75$m. The photos are from [85].

The origin of the numerical coordinate system is located on the incident boundary, with $z = 0$ at the bottom of the basin and $y = 0$ at the symmetric plane.

The length of the computational region in the wave direction in front of the cylinders in one wavelength λ_m that contains 95% of the mass of incident solitary

wave. And λ_m can be estimated from the formula [12]:

$$\lambda_m = \frac{4.12h}{\sqrt{H/h}} \tag{4.17}$$

The lateral domain width is $3D$ or $5D$ for the case of single cylinder and the case of three cylinders respectively, to ensure that the reflection from the lateral wall has not reached the cylinders at the end of each numerical simulation.

The upper (ceiling) and lower (bottom of the wave basin) boundaries and two lateral boundaries as well as the surface of the cylinders of the computational domain are rigid boundaries. Therefore, the no-flux (free-slip) boundary condition is applied. A numerical sponge layer is appended at the end of the numerical wave tank to damp out the outgoing wave. The incident wave information, including the velocity and the water surface displacement, are provided by Grimshaw's 3rd-order solitary wave formula [24] as described in Chapter 3.

Unstructured meshes are used to discretize the computational domain with small volumes in the vicinity of the cylinders. Generally speaking, the volume size is chosen such that there are 60 to 120 grids within one wavelength λ_m in the horizontal directions, $\lambda_m/\Delta x = O(60 \sim 120)$, and 15 to 20 grids within the wave height H in the vertical direction, $H/\Delta x = O(15 \sim 20)$. The total cell number can be up to 1.4 million which almost reaches the limit of our computing facilities.

In the following section, two representative experimental cases (one cylinder and three cylinders) are presented in detail. In both cases the still water depth is $h = 0.75$ m and the wave height of the solitary wave is $H = 0.3$ m. An extensive parameter study of single cylinder case is then discussed.

4.5 Single Cylinder Case

In this study, we have carried out 12 numerical simulations of laboratory experiments with single cylinder. However, one representative simulation ($H/h = 0.40$, $h/D = 0.62$) is discussed in detail.

The numerical setup is described in section 4.4. The numerical simulation starts at a quiescent state, and the solitary wave is sent into the computational domain by specifying the surface elevation and velocity at the incident wave boundary. The simulation is terminated after the wave has passed the cylinder. Numerical wave gauges were located according to the laboratory experiment arrangement. Figure 4.9 shows the mesh used in the numerical simulation.

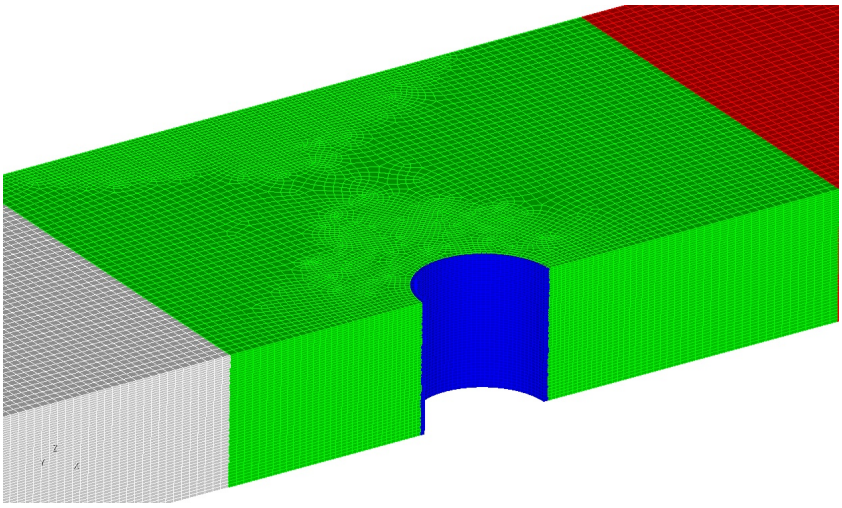

Figure 4.9: Computational mesh for single cylinder case. Finer grid size is used in the neighborhood of the cylinder.

4.5.1 Free Surface Profile

Figure 4.10 shows the comparison of numerical and analytical solitary wave profile at the first two numerical wave gauges. The free surface elevation is normalized by the incident wave height H, and the time is scaled by $\sqrt{h/g}$. The agreement is very good, although the analytical solitary wave is a little wider than the numerical wave. It demonstrates that the numerical wave generator can generate good non-breaking solitary wave as desired.

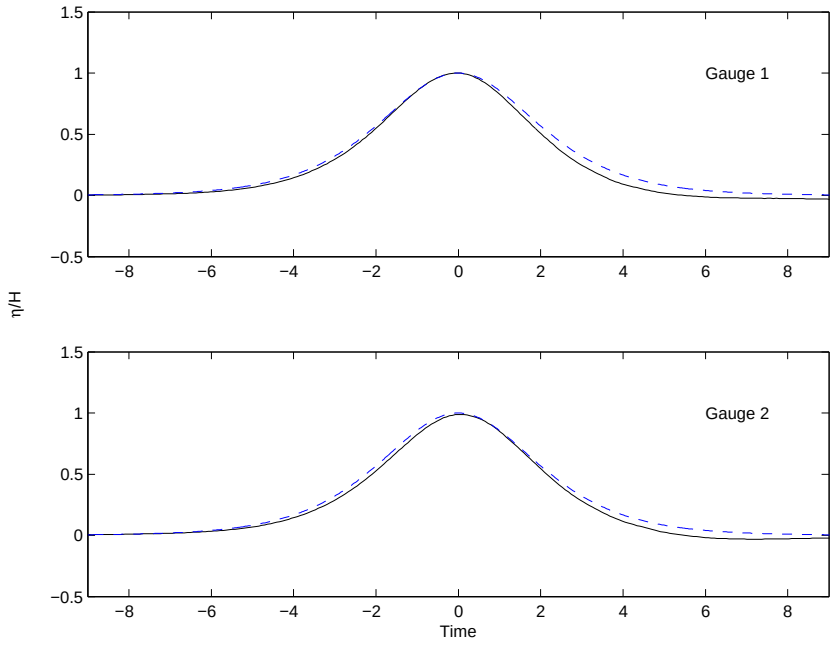

Figure 4.10: Comparison of numerical and analytical solitary wave profiles ($H/h = 0.4$, $h = 0.75$m). Solid: numerical; dash line: analytical (Grimshaw's formula)

Figure 4.11 presents the the numerical results of the time histories of free surface displacements at several wave gauge locations for the one cylinder case (c.f. Figure 4.1). Excellent agreement between the numerical results and the experimental data is observed for the leading waves at all locations. As the

solitary wave propagates to the cylinder, its wave height gets higher due to the blockage of the cylinder. A noticeable scattering wave from the cylinder can be seen at the measurements of wave gauges 4–7. The first scattered wave is due to the wave reflection at the front (impact) side of the cylinder. And a relative higher surface elevation at the back (lee) side causes a secondary scattered wave as seen at gauge 7. The phase of the secondary numerical scattered wave does not match very well with the laboratory wave phase, which could be due to flow separation.

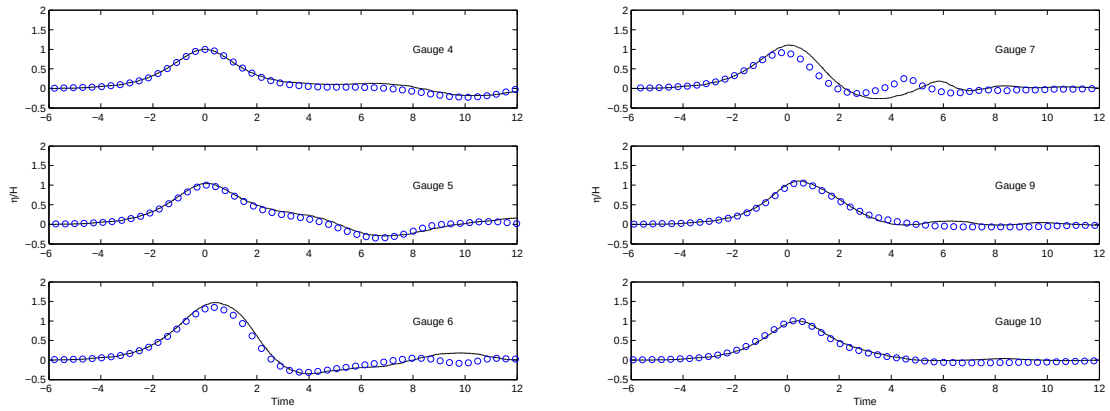

Figure 4.11: Time history of free surface elevations at wave gauges for the one cylinder case. The circles are experimental data and the solid lines are numerical results.

Figure 4.12 shows the time history of free surface elevations around the cylinder. As the solitary wave wraps around the cylinder, the wave height is significantly reduced. At $\theta = 90°$, the wave height is already reduced by a half. As the solitary wave crest passes the cylinder, a noticeable trough below the still water level is observed at the front side ($0° < \theta < 90°$) of the cylinder. It is also noted that the secondary scattered wave shows a small overturning shape at $\theta = 150°$ which may indicate local wave breaking phenomena. However, since it is an inviscid flow simulation, the local turbulence effect is not modeled and

is accounted for by the pure numerical dissipation.

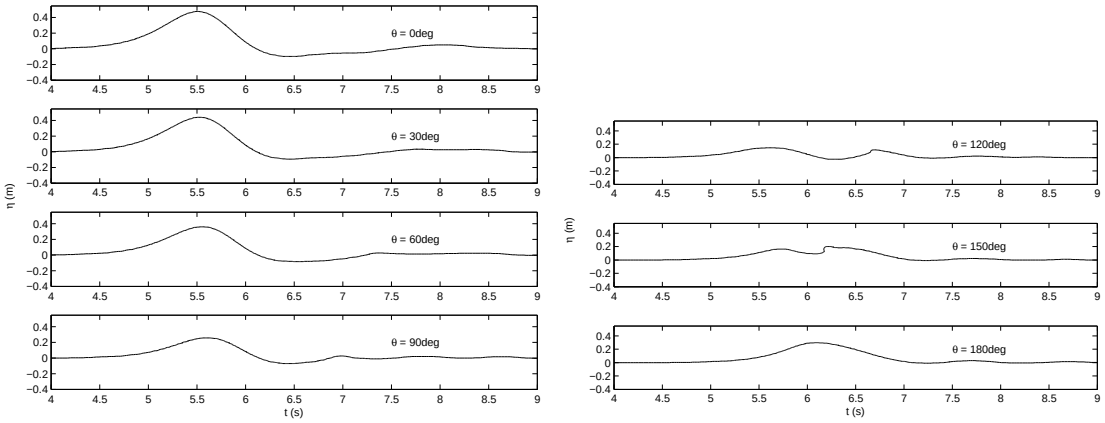

Figure 4.12: Time history of free surface elevations around the cylinder. $\theta = 0°$ indicates the front side, and $\theta = 180°$ is the back side of the cylinder.

Figure 4.13 shows the snapshots of free surface on the symmetrical plane. The analytical free surface (dash line) propagating without the cylinder is also plotted as a comparison. The free surface around the cylinder circumference is also projected horizontally onto this plane and presents the surface displacement around the cylinder. The numerical wave approaches the cylinder at a wave speed very close to the analytical value $C = 3.17\text{m/s}$, and it lags behind and generates scattered waves due to the block effect of the cylinder. The solitary wave almost reverts back to its original shape after it passed the cylinder for a distance of about 4 times the cylinder radius, which shows that the cylinder radiates only a very small amount of the solitary wave energy. It is reasonable that the presence of the cylinder does not influence the wave field very much since the wave length is much longer than the size of the cylinder ($\lambda/D = 9.7$). It is also noted that there exists a kink at the back side of the cylinder ($120° < \theta < 150°$) after the wave run-up at the front side reaches its maximum, which reflects the existence of free surface detachment.

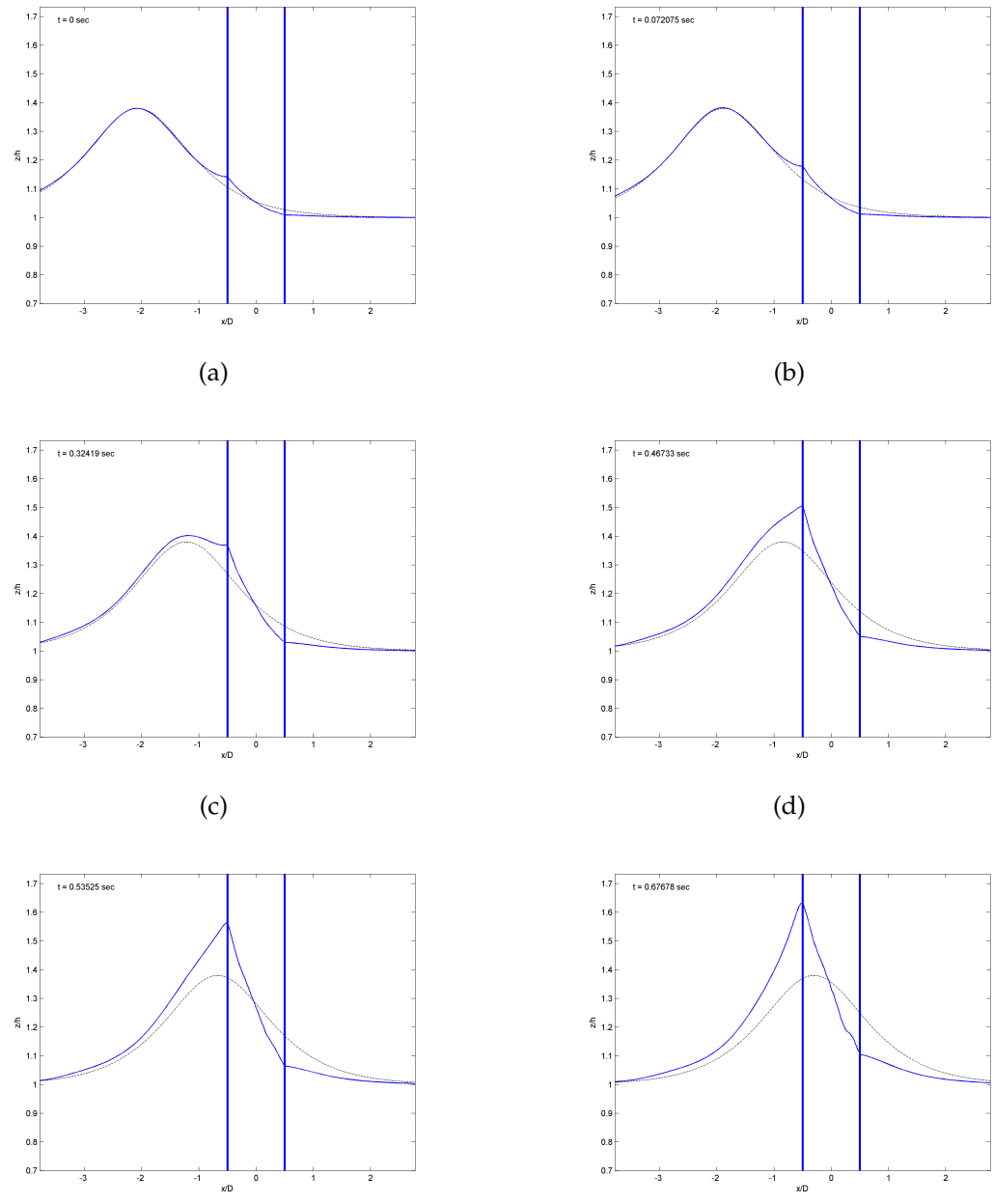

(a) (b) (c) (d) (e) (f)

Figure 4.13: Free surface profile on the symmetrical plane. The dash line represents the analytical solitary wave profile without the presence of the cylinder as a comparison to the numerical wave. The free surface inside the cylinder range is the horizontal projection of the free surface around the cylinder.

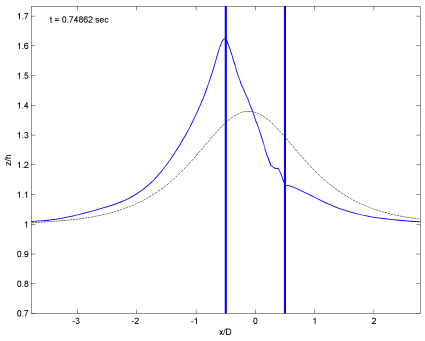

(g)

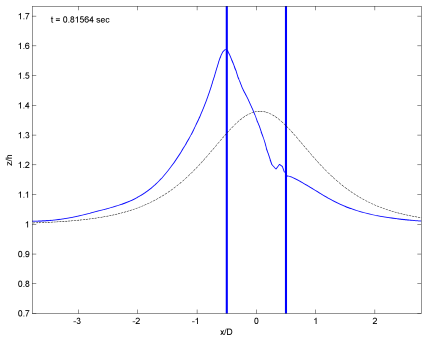

(h)

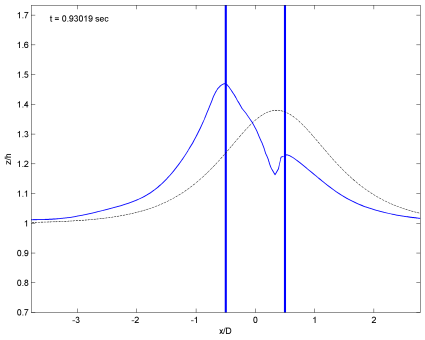

(i)

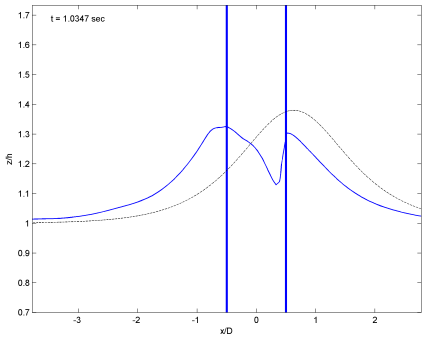

(j)

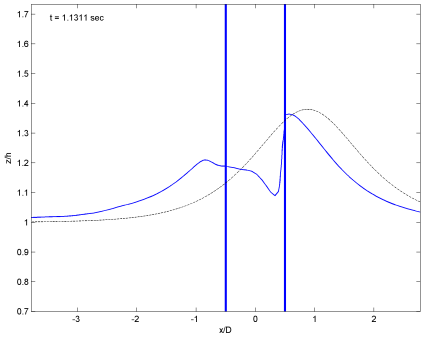

(k)

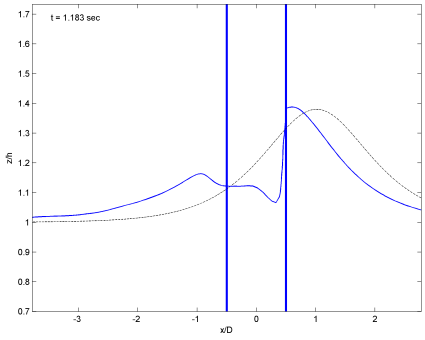

(l)

Figure 4.13: Free surface profile on the symmetrical plane (cont).

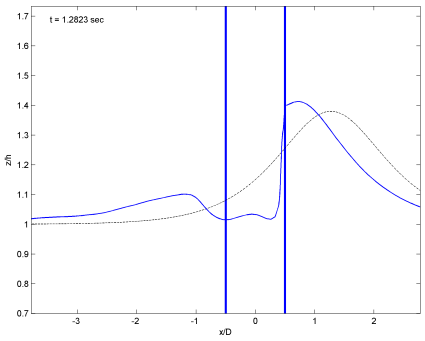

(m)

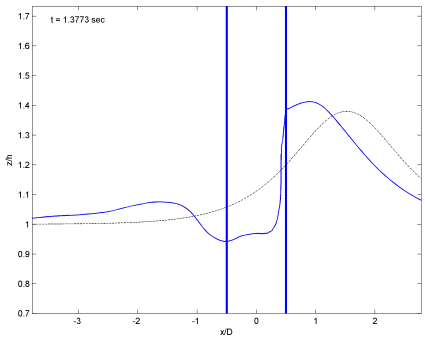

(n)

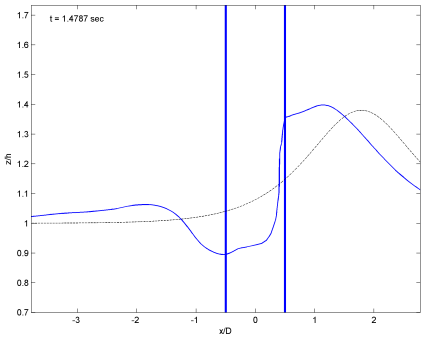

(o)

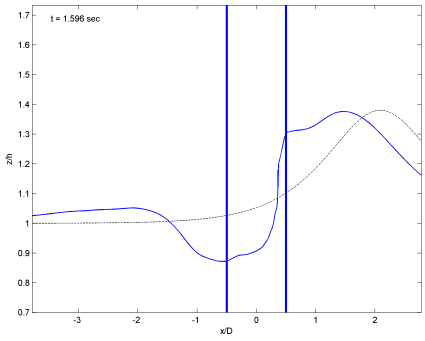

(p)

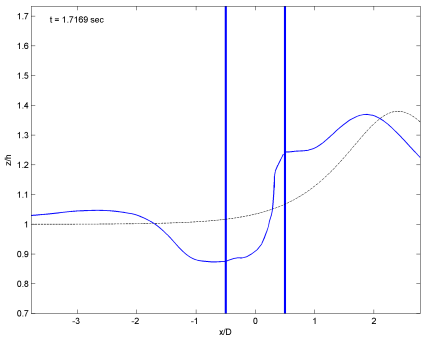

(q)

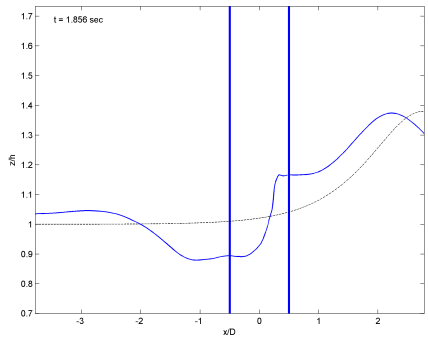

(r)

Figure 4.13: Free surface profile on the symmetrical plane (cont).

Figure 4.14 presents the three dimensional free surface profiles as the solitary wave impinges and passes the cylinder. Two scattered waves can be seen in the figure. One is due to the reflection from the front side of cylinder, and the other is generated by the water column trapped behind the cylinder and propagates along the cylinder circumference and to the sides.

4.5.2 Run-up on the cylinder

Figure 4.15 shows the run-up of numerical and laboratory solitary wave on the front side of the cylinder. The numerical model captures very well the phase and magnitude of the wave run-up. The solitary wave increases by 70% than the normal incident wave height at the front side of the cylinder.

4.5.3 Velocities

Figure 4.16 presents the particle velocity measurements at laboratory ADV locations. The agreement between the experimental data and the numerical results for all three velocity components is quite good. It is not surprising the flow filed is dominated by the velocity component in the direction of wave propagation.

Figure 4.16(a) shows that the numerical and laboratory kinematics agrees rather well before the ADV instrument senses the influence of the cylinder. It, combined with the free surface comparison in Figure 4.10, confirms that the incident wave condition agrees with the laboratory condition.

Figure 4.16(b) – 4.16(d) show the velocity measurement at the off-symmetric-

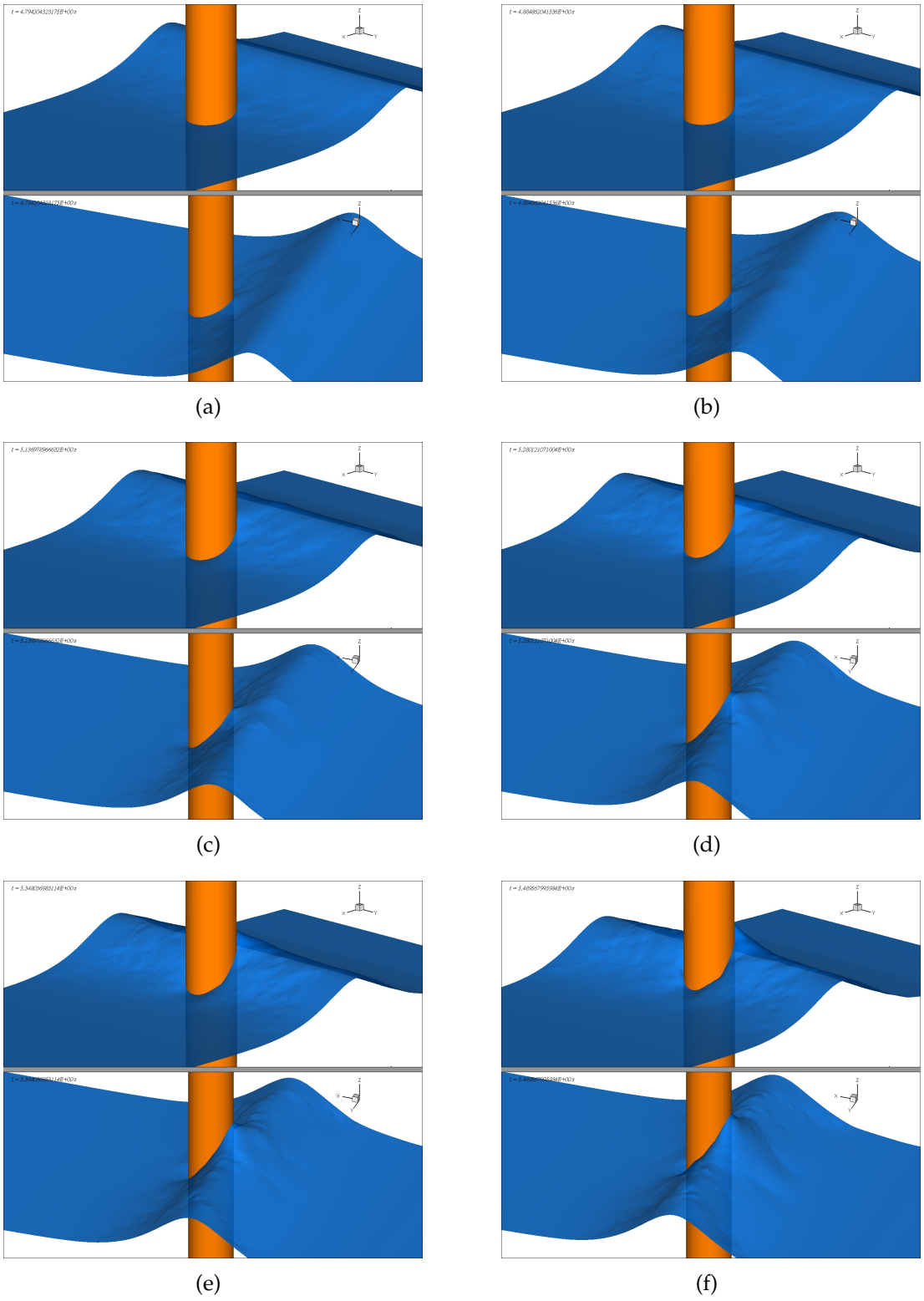

(a) (b) (c) (d) (e) (f)

Figure 4.14: Snapshots of three dimensional free surface profiles. The upper and lower graphs in each subfigure show the three dimensional view from two different view angles.

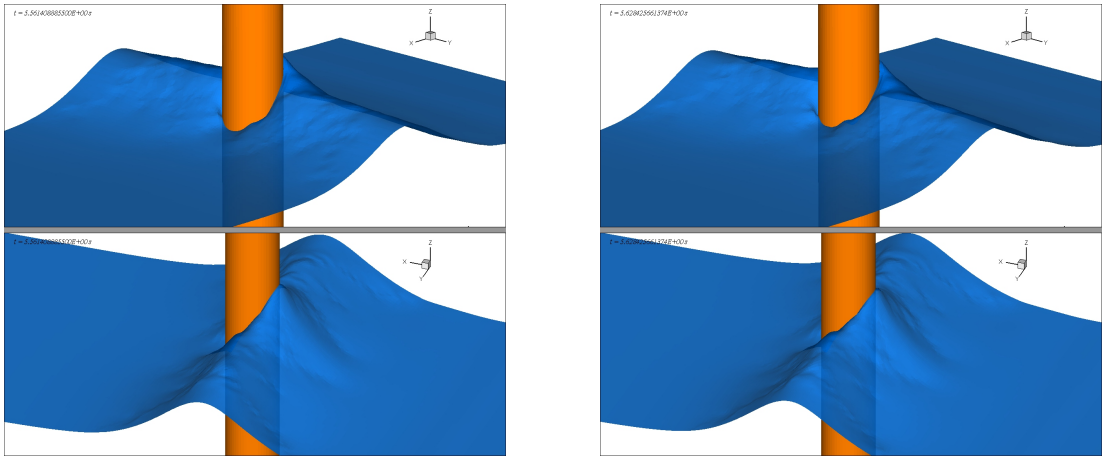

(g) (h)

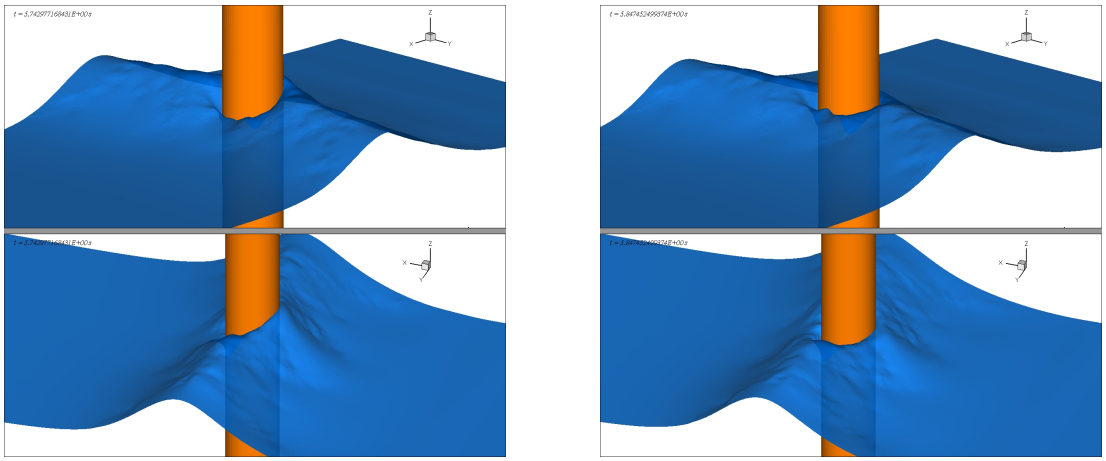

(i) (j)

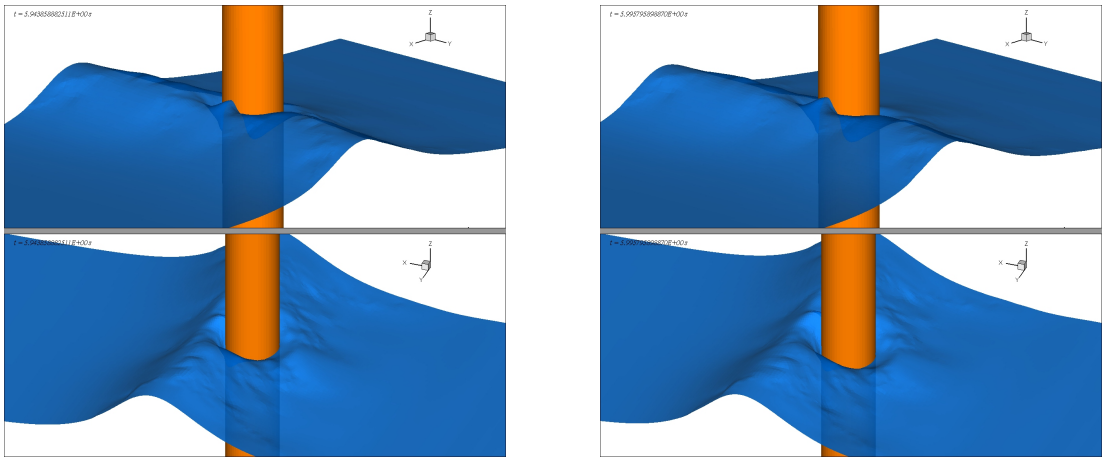

(k) (l)

Figure 4.14: Snapshots of three dimensional free surface profiles (Cont).

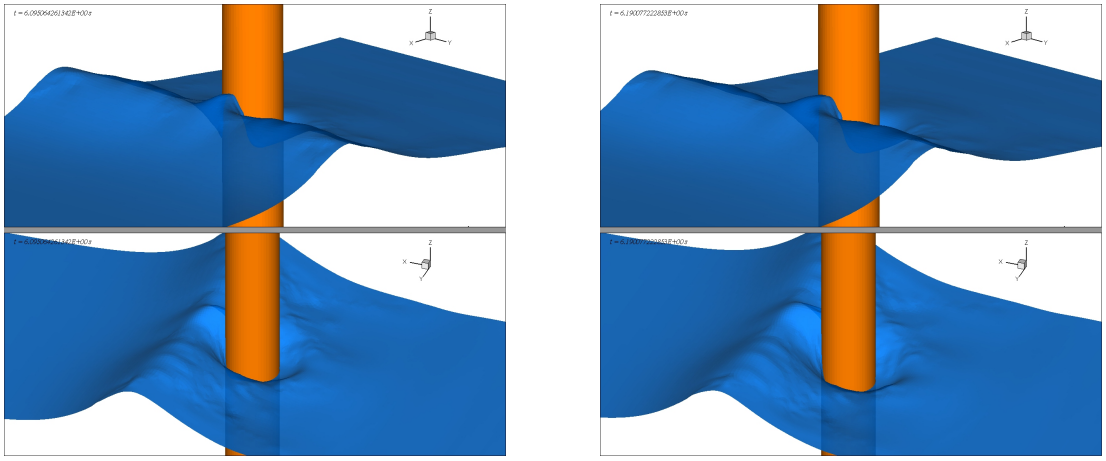

(m) (n)

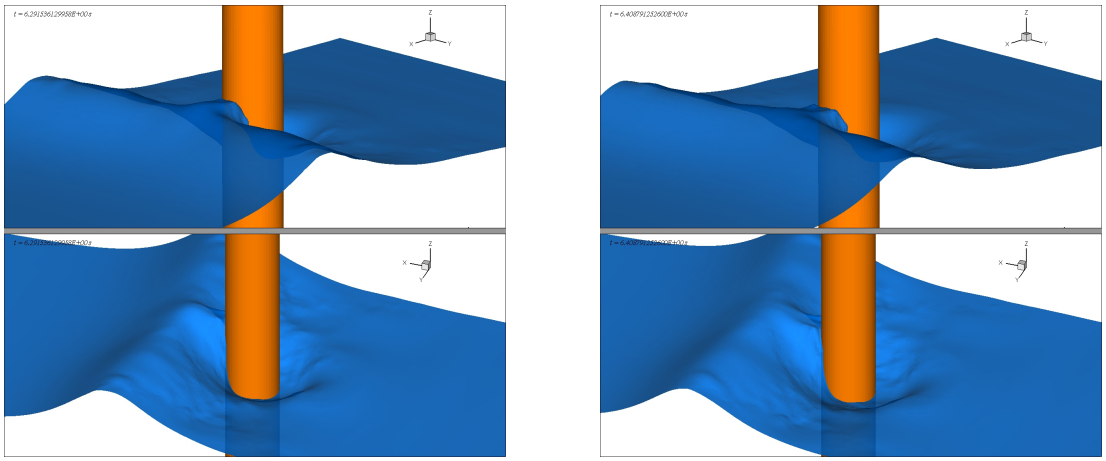

(o) (p)

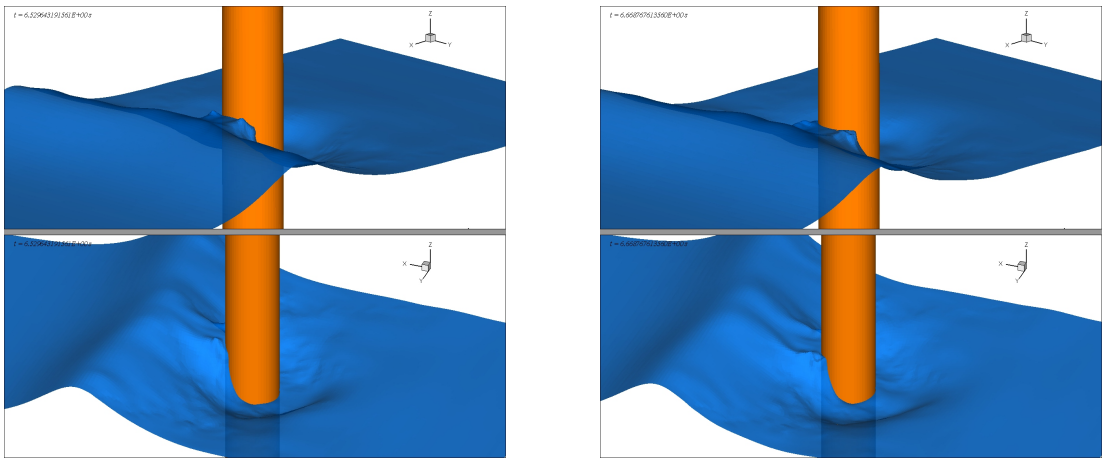

(q) (r)

Figure 4.14: Snapshots of three dimensional free surface profiles (Cont).

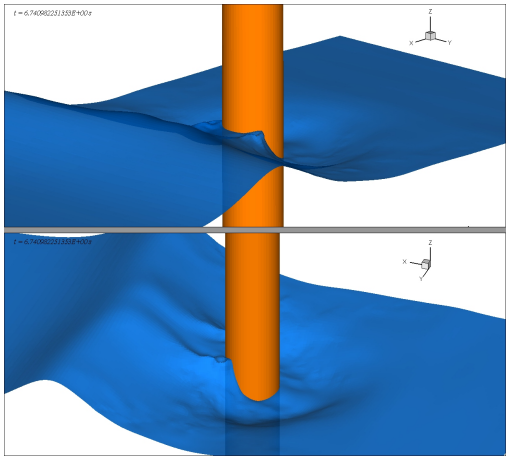

(s)

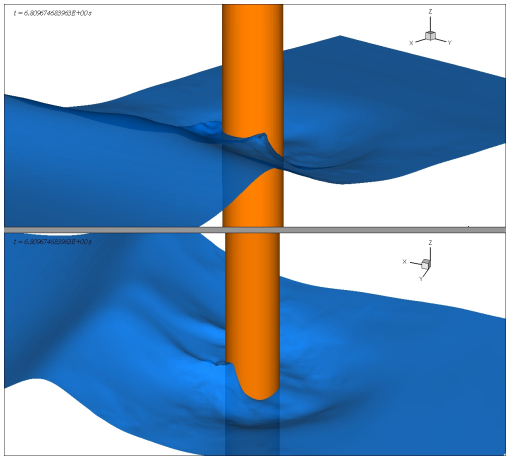

(t)

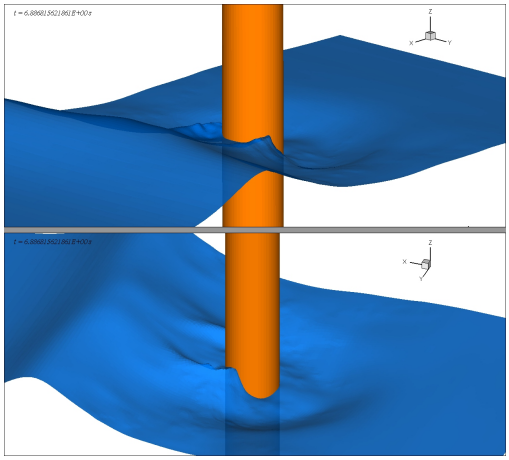

(u)

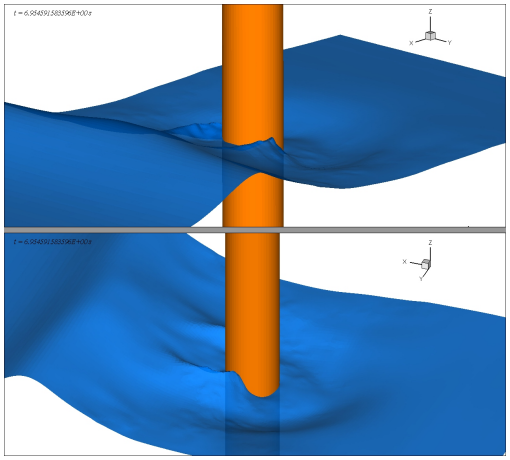

(v)

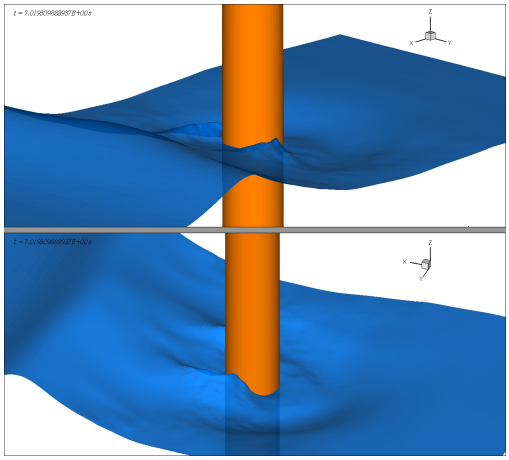

(w)

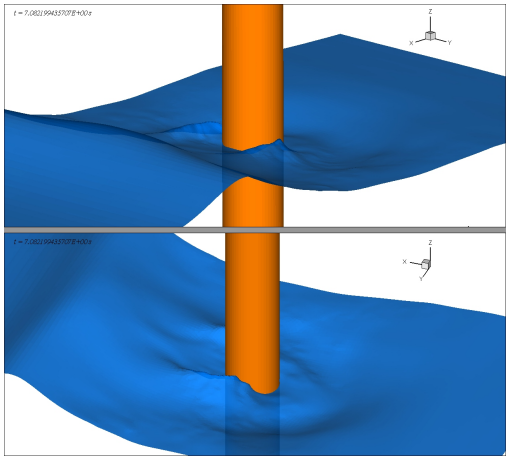

(x)

Figure 4.14: Snapshots of three dimensional free surface profiles (Cont).

plane locations near the cylinder. In general, the numerical horizontal velocity component under-predicts the velocity magnitude, while the lateral and vertical velocity components show good agreements with laboratory measurements. It may indicate that the cylinder has a stronger blockage effect in our numerical simulation. There exist strong counter-directional lateral flows at the cylinder's front and back region (Figure 4.16(b) and 4.16(d)), which renders almost zero lateral velocity (Figure 4.16(c)) at the plane which is normal to the symmetric plane and passes through the cylinder axes.

Figure 4.17 shows the velocity field and dynamic pressure distribution at the neighborhood of the cylinder. In Figure 4.17(a,b), the solitary wave crest has not reached the cylinder yet. As the wave reaches the cylinder, the water passes around the cylinder smoothly, and the dynamic pressure distribution along the cylinder circumference does not show the adverse pressure gradient. In Figure 4.17(e,f), the run-up at the front side of cylinder reaches its maximum, no adverse flow is observed at both planes. In Figure 4.17(g,h), the wave crest moves to the middle of the cylinder, and the adverse dynamic pressure gradient shows up at the back side of the cylinder, although no adverse flow is present yet. The adverse pressure gradient near the still water level is clearly larger than that at the middle of the water depth. This adverse pressure gradient is due to the free

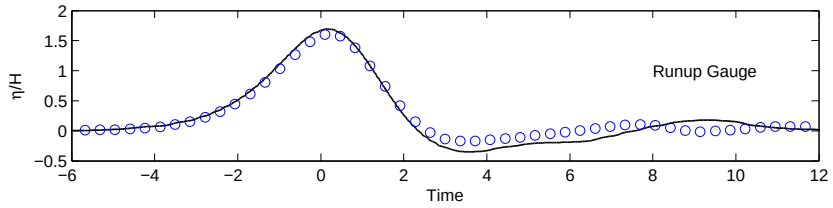

Figure 4.15: Solitary wave run-up on the cylinder ($H/h = 0.40$, $h = 0.75$m). The cirles are laboratory data, and solid line is the numerical result.

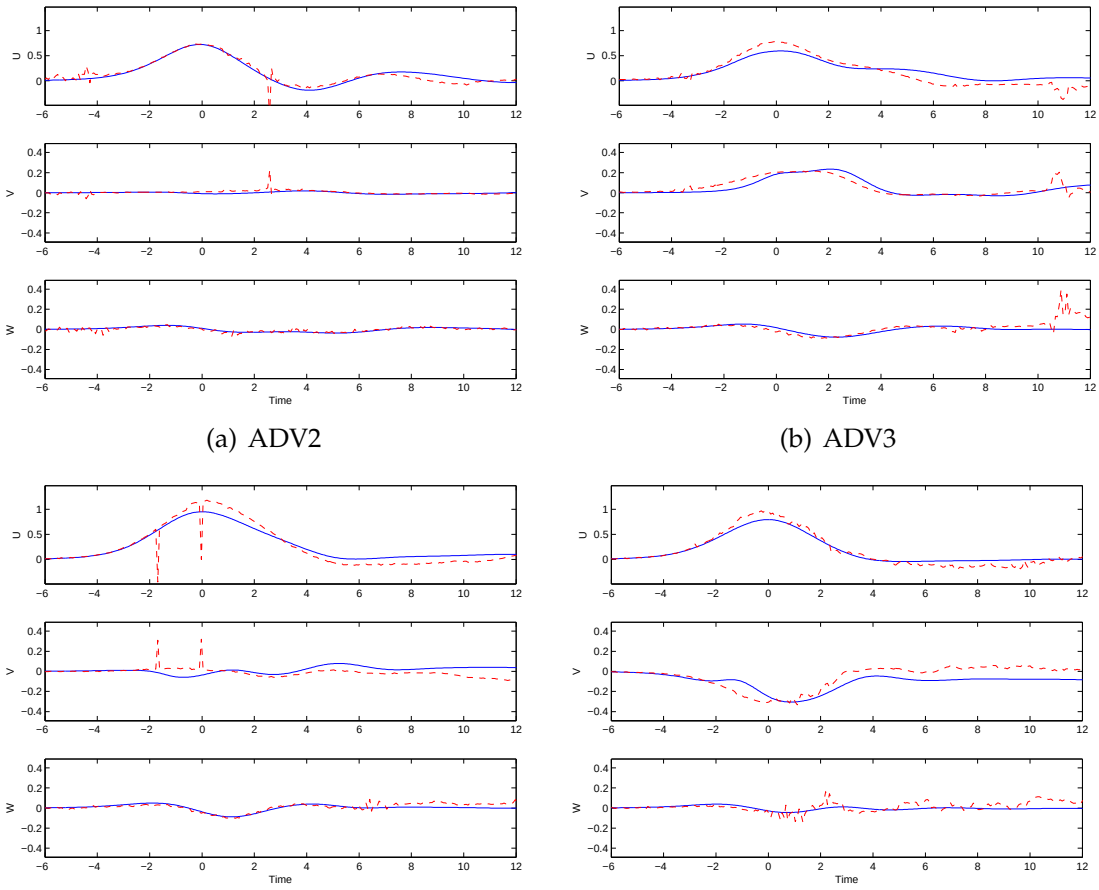

(a) ADV2 (b) ADV3

(c) ADV4 (d) ADV5

Figure 4.16: Time histories of particle velocity components at specified locations. Solid line: numerical results; Dash line: laboratory measurements.

surface difference there: the free surface on the cylinder is lower than the neighboring free surface which does not touch the cylinder. In Figure 4.17(k,l), the wave crest has passed by the cylinder, a small vortex is generated at the lee side of the cylinder on the top plane and evolves eventually to the bottom as seen in 4.17(m,n). As the wave leaves the cylinder, a scattered wave is generated at the back of the cylinder and propagates upstream along the cylinder surface. It triggers a second vortex at the position a little behind the middle of the cylinder and the corresponding counter-direction vortex outside the cylinder. The vortex

is also first seen on the top plane and later present on the lower plane.

4.5.4 Pressure around the cylinder

The dynamic pressure response along the front line of the cylinder are shown in Figure 4.18. The positions of the pressure sensors can be found in Figure 4.4. The agreement between the numerical results and experimental data is rather disappointing. The measured data are not reasonable at several transducers, especially those near the free surface or above the still water level. For example, negative pressures are measured under wave crest at transducer 10. It suggests that some of these transducers did not function properly. As the free surface and velocities show excellent agreements with laboratory data, it is most probably that the numerical pressure measurement is also reliable, therefore the numerical data could be used to calibrate the laboratory pressure transducers.

4.5.5 Wave load on the cylinder

Figure shows the horizontal hydrodynamic force on the cylinder. Good agreement between the experimental and numerical data is observed.

4.5.6 Extensive parameter study

The laboratory setup parameters are confined in a very small range ($h/D = 0.37, 0.49, 0.61$). The numerical simulation has the advantage of easily changing the wave and geometry parameters to study the physics in a wider range.

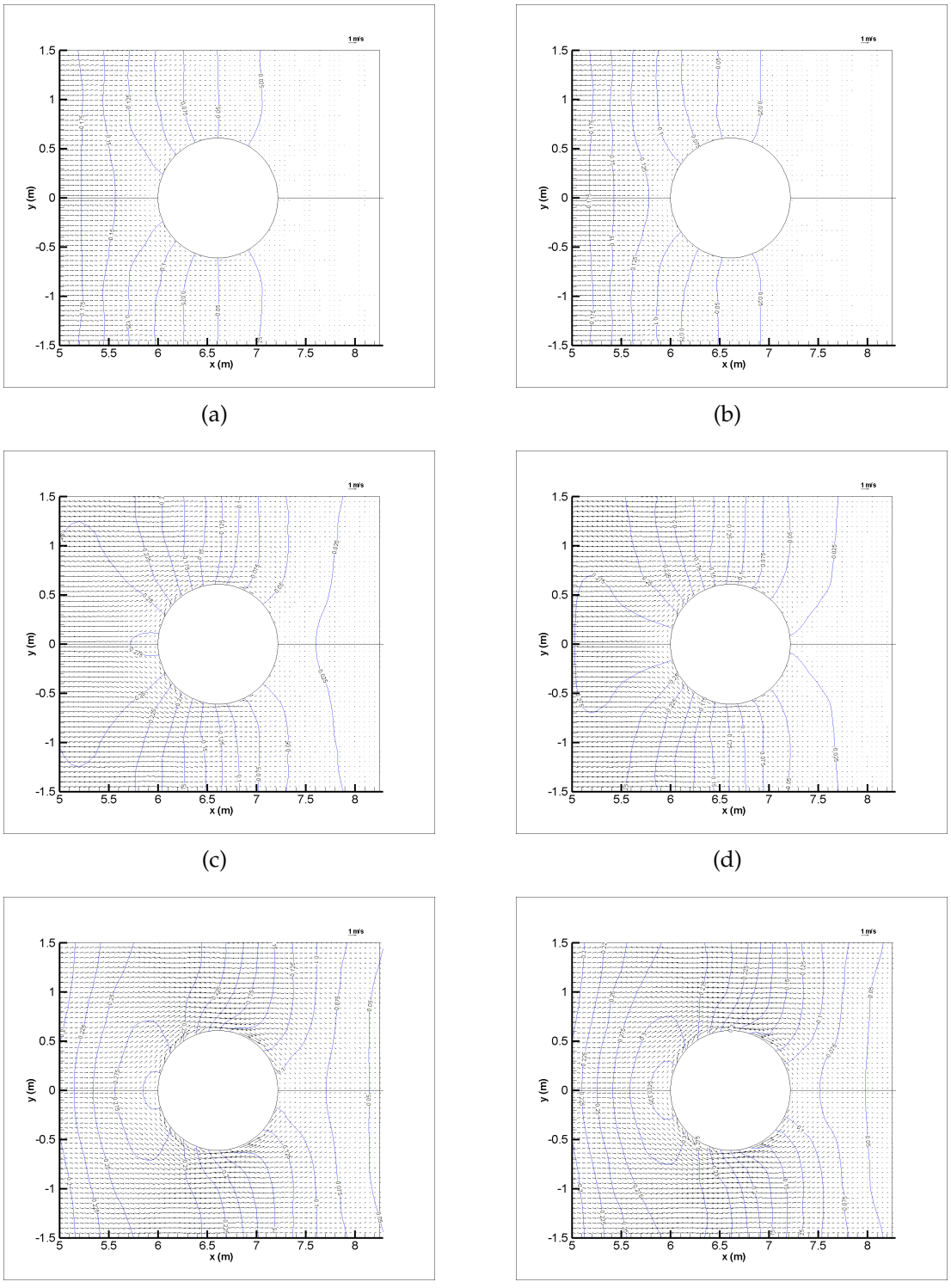

(a) (b)

(c) (d)

(e) (f)

Figure 4.17: Velocity and dynamic pressure field near the cylinder on horizontal cross-section. Left: z = 40cm plane; right: z = 70cm plane. From top to bottom: t = 4.88, 5.145.49s.Dynamic pressure is in meters.

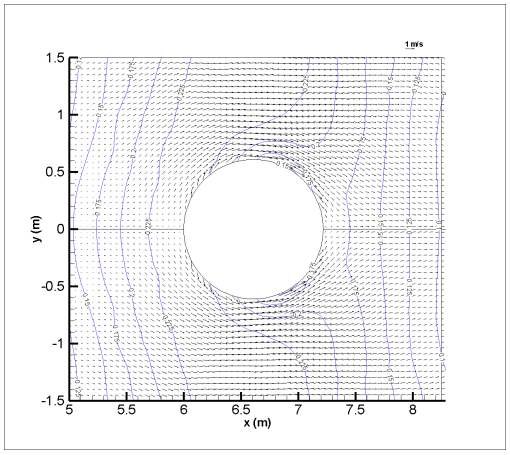

(g)

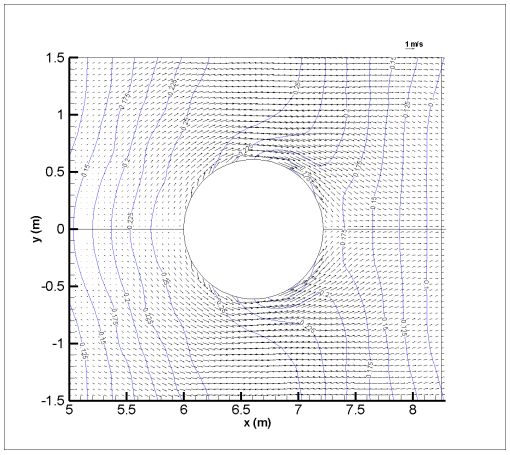

(h)

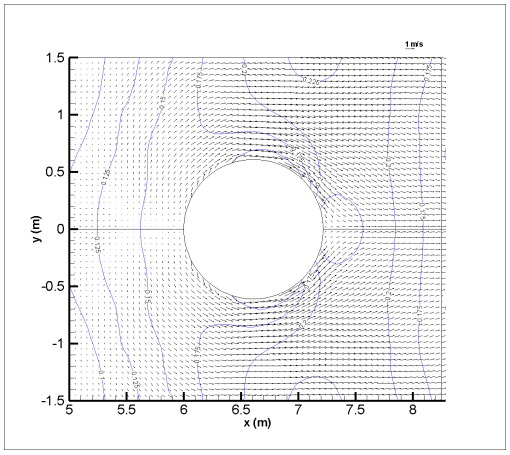

(i)

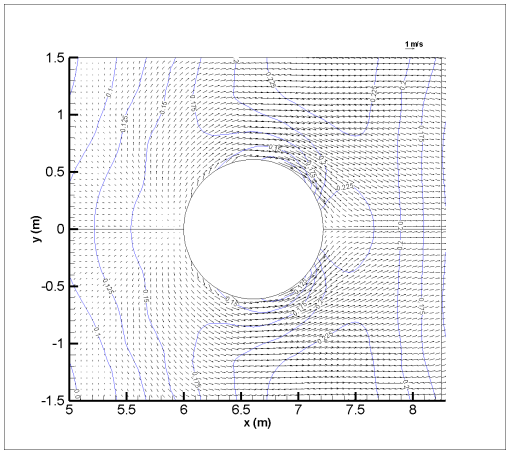

(j)

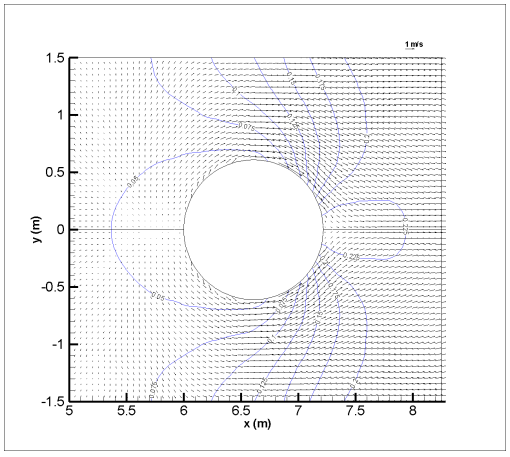

(k)

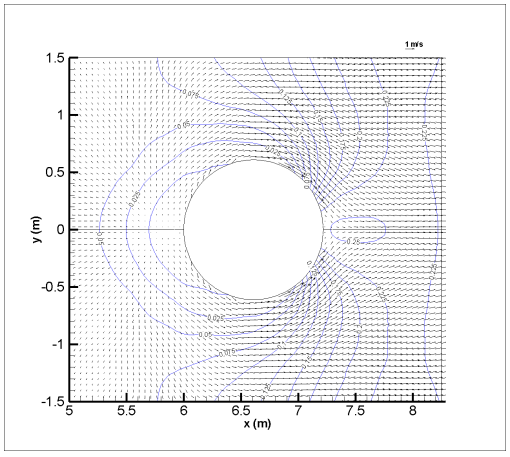

(l)

Figure 4.17: Velocity and dynamic pressure field near the cylinder on horizontal cross-section (cont). From top to bottom: t = 5.74, 5.94, 6.14s.

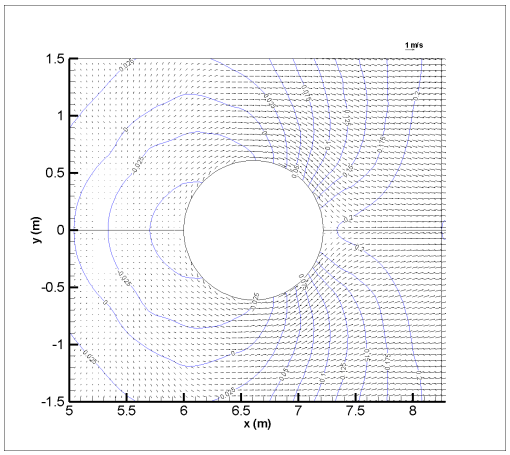

(m)

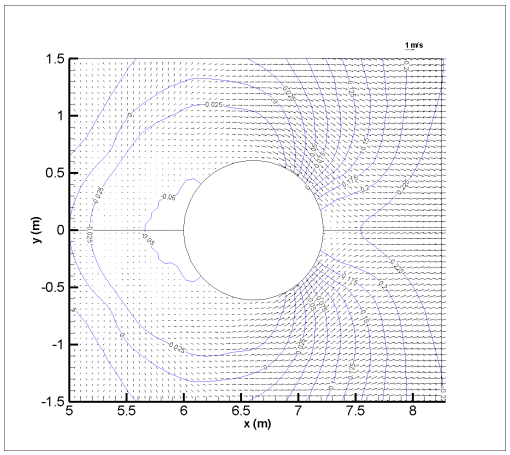

(n)

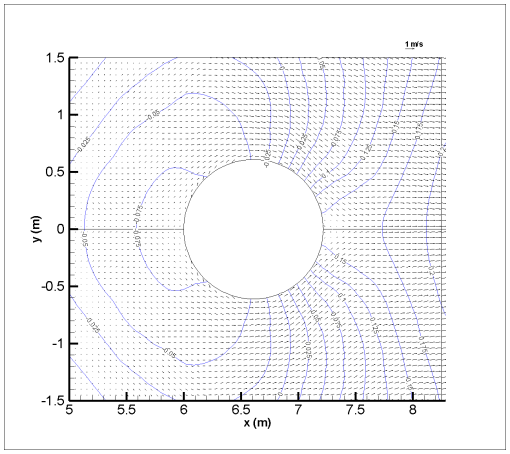

(o)

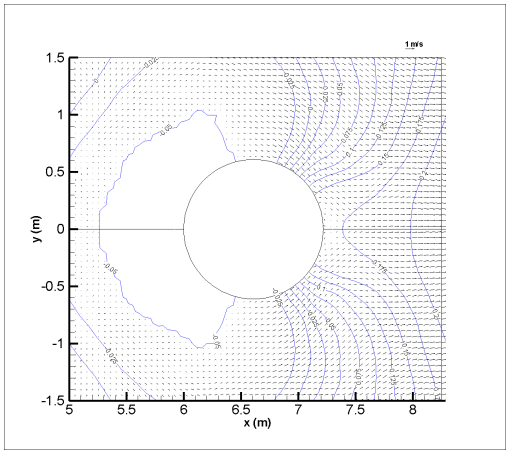

(p)

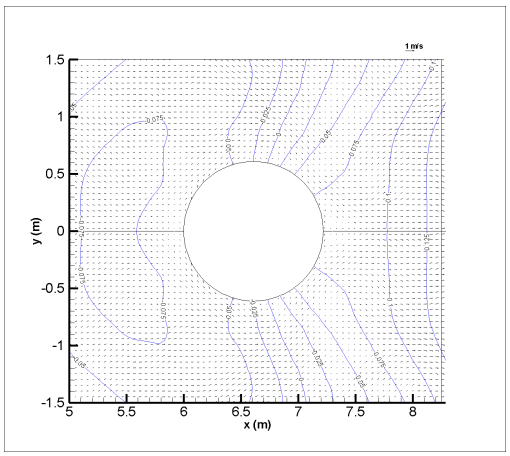

(q)

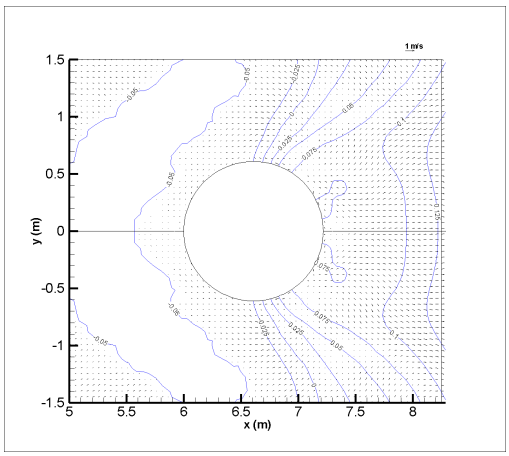

(r)

Figure 4.17: Velocity and dynamic pressure field near the cylinder on horizontal cross-section (cont). From top to bottom: t = 6.35, 6.53, 6.81s.

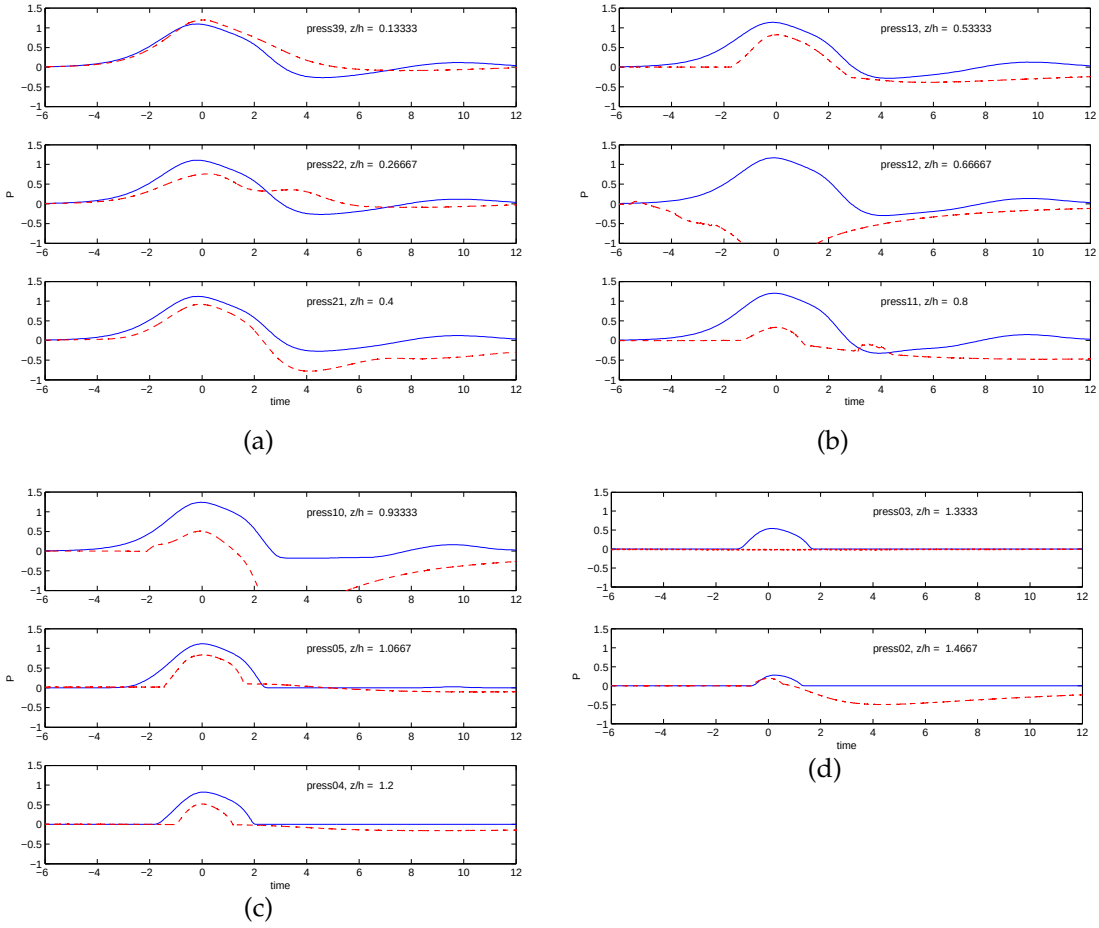

Figure 4.18: Time histories of pressure at the front line of cylinder. Solid line: numerical results; Dash line: laboratory measurements.

In this study, the parameter h/D is extended, and a total of 24 numerical simulations were carried out with different combination of h/D and H/h as shown in Table 4.1. However, the extent of h/D is still limited due to the constraint of computational resources since larger h/D requires more CPU time and computer memories. The maximum horizontal force and run-up at the front side of the cylinder will be presented here since they are important in the design of offshore structures.

As stated in Section 4.1, the solitary wave exerted on the cylinder can be

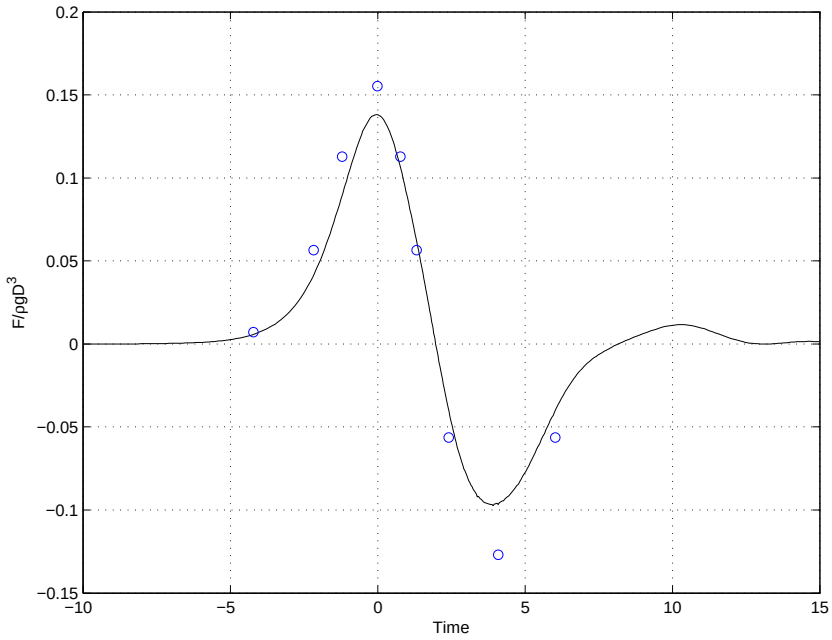

Figure 4.19: Horizontal force on the cylinder of single cylinder case. The circles are laboratory data, and solid line is the numerical results.

expressed as:

$$\frac{F}{\rho g D^3} = f\left(\frac{H}{h}, \frac{h}{D}, Re_D, \frac{t}{\sqrt{h/g}}\right) \tag{4.18}$$

Since our numerical results are based on the inviscid flow calculation, the dependency on the Reynolds number vanishes. In other words, the numerical results only apply for high Reynolds number flow. In addition, we are concerned with the maximum wave force, thus the time dependence is ignored. Therefore, the maximum horizontal force exerted on a single cylinder by a non-breaking

Table 4.1: Extensive wave parameters.

h/D	0.41	0.69	1.0	3.0	5.0	7.0	10.0
H/h	0.1	0.2	0.33	0.4			

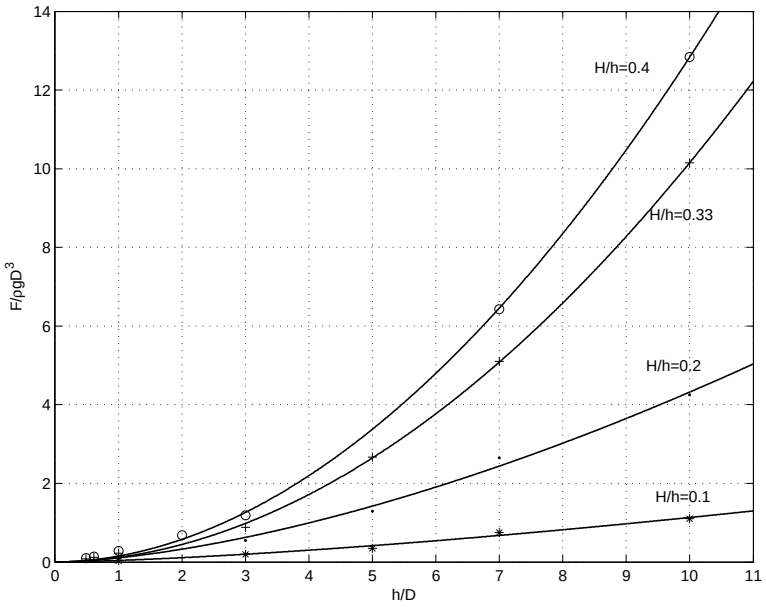

Figure 4.20: Maximum horizontal force as a function of h/D.

solitary wave can be expressed as:

$$\frac{F}{\rho g D^3} = f\left(\frac{H}{h}, \frac{h}{D}\right) \tag{4.19}$$

Figure 4.20 shows the maximum horizontal force as a function of h/D. Their fitting formula are listed in Table 4.2. Since we use cylinder diameter D in the normalization of the force, the increase of h/D should be explained as the increase of still water depth. It is shown that the maximum force is not linear with h/D even though the non-linearity is very small $H/h = 0.1$. And the force increases faster with the increase of still water depth h at higher non-linear incident solitary wave.

Figure 4.21 presents the maximum horizontal force as a function of H/h, and the fitting formula are listed in Table 4.3. The force is not linear with H/h either, and higher h/D does not necessarily mean a faster force increase with the non-

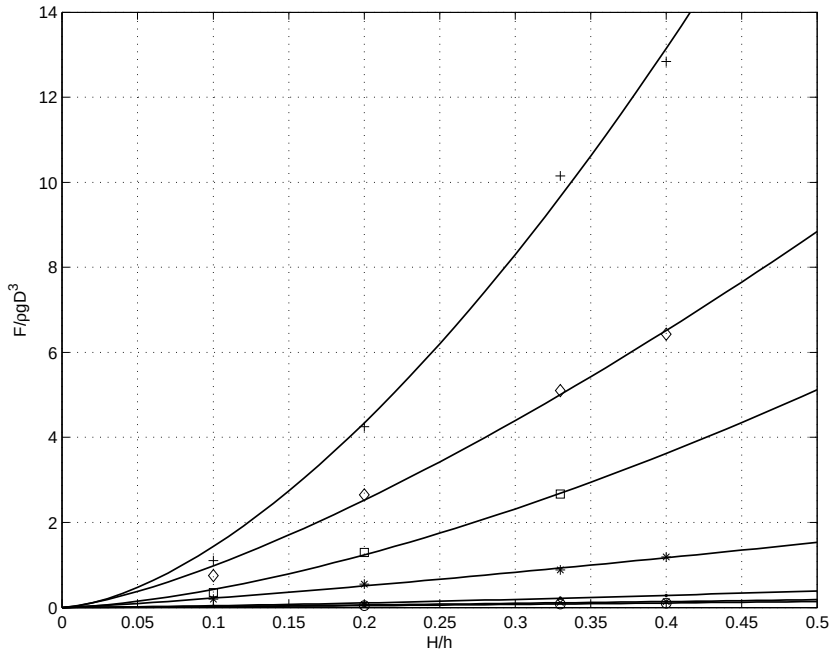

Figure 4.21: Maximum horizontal force as a function of H/h. From top to bottom: h/D = 10, 7, 5, 3, 1, 0.69, 0.41.

linearity H/h.

Figure 4.22 shows the maximum run-up at the front side of the cylinder as a function of h/D. The fitting formula are listed in Table 4.4. It is seen that the maximum run-up is nearly linear with h/D, but essentially they are not. And for all the simulated solitary waves, the increase rate of maximum run-up gets

Table 4.2: Maximum horizontal force fitting formula as a function of h/D: $F_m = \alpha(h/D)^\beta$.

H/h	α	β	R^2
0.1	0.04075	1.44	0.9861
0.2	0.1078	1.603	0.9954
0.33	0.1166	1.94	0.9996
0.4	0.1519	1.927	0.9997

Table 4.3: Maximum horizontal force fitting formula as a function of H/h: $F_m = \alpha(H/h)^{\beta}$.

h/D	0.41	0.69	1	3	5	7	10
α	0.3472	0.4434	1.041	3.524	14.98	22.81	56.88
β	1.313	1.242	1.415	1.205	1.55	1.368	1.599
R^2	0.9927	0.9782	0.9964	0.9923	0.9967	0.9956	0.9922

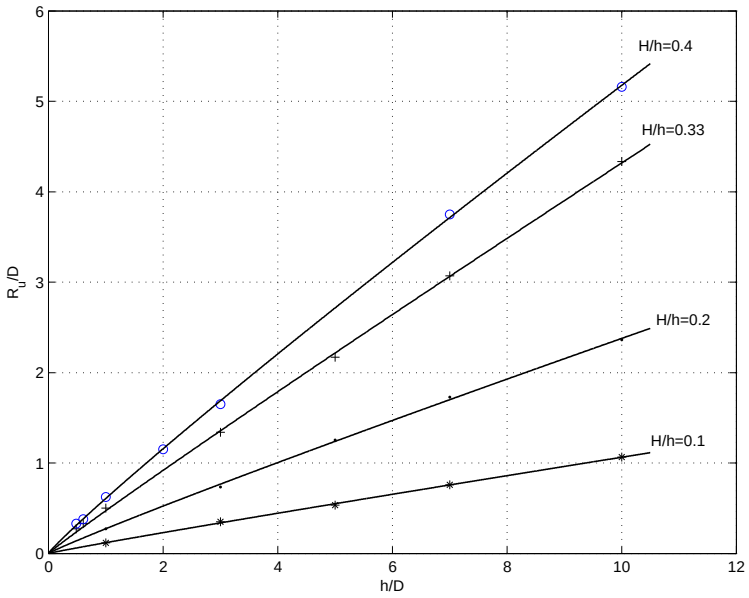

Figure 4.22: Maximum run-up at the front side of the cylinder as a function of h/D.

slower as the still water depth h increases.

Figure 4.23 shows the maximum run-up at the front side of the cylinder as a function of H/h. The fitting formula are listed in Table 4.5. For the same value of h/D, the maximum run-up increase faster than H/h does.

Table 4.4: Maximum run-up fitting formula as a function of h/D: $R_u = \alpha(h/D)^{\beta}$.

H/h	0.1	0.2	0.33	0.4
α	0.1185	0.2723	0.4707	0.6062
β	0.9529	0.941	0.9624	0.9313
R^2	0.9993	0.9991	0.9996	0.9998

Table 4.5: Maximum run-up fitting formula as a function of H/h: $R_u = \alpha(H/h)^{\beta}$.

h/D	1	3	5	7	10
α	1.902	4.715	7.715	10.66	14.75
β	1.211	1.143	1.141	1.133	1.13
R^2	0.9999	0.9995	0.9991	0.9995	0.9979

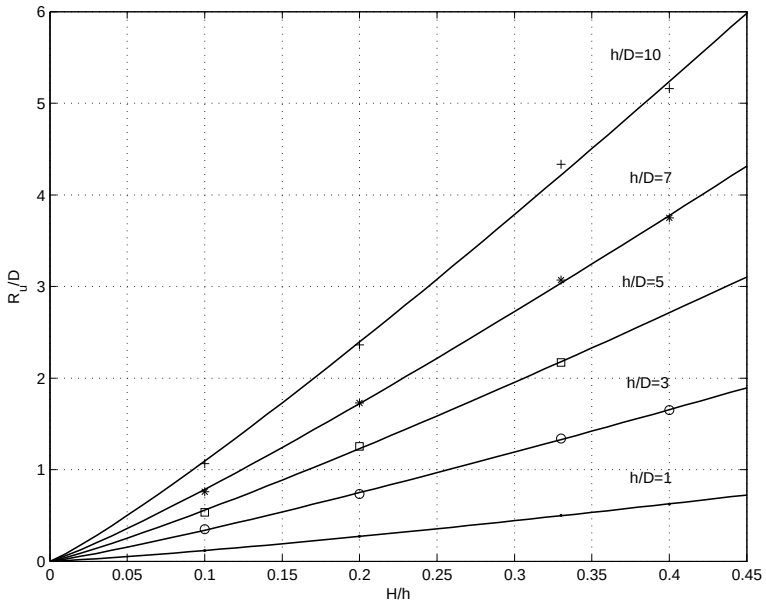

Figure 4.23: Maximum run-up at the front side of the cylinder as a function of H/h.

4.6 Multiple Cylinders Case

In the laboratory experiments, two different cylinder arrangements were deployed: one with a center-to-center distance between the dummy cylinders equal to $3D$ (Figure 4.2) and the other $2D$ (Figure 4.3). The laboratory experiments showed that the cylinder arrangement $C2$ with larger gap renders smaller shielding effect in terms of the free surface elevation around the cylinder. Therefore, we only concerned about the cylinder arrangement with $2D$ center-to-center distance between the dummy cylinders. In this section, a representative case (H/h = 0.40, h/D = 0.62) is presented, and the comparison between single and multiple cylinders is also discussed. It should be noted here that three cylinders are of the same dimensions.

The numerical setup is similar to the single cylinder case, except that the computational domain is larger thus a relatively coarser grid size is used. The simulation is terminated after the wave has passed the instrumented cylinder. The computational mesh is shown in Figure 4.24.

4.6.1 Free surface profile

Figure 4.25 shows the numerical results of the time histories of free surface elevation at specified wave gauge locations for the multiple cylinder case. Excellent agreement between the numerical and experimental data is observed for the leading wave at all locations.

Numerical solitary wave profiles at wave gauge 2 and 3 indicate desirable incident wave condition. As the solitary wave impacts on the two front dummy

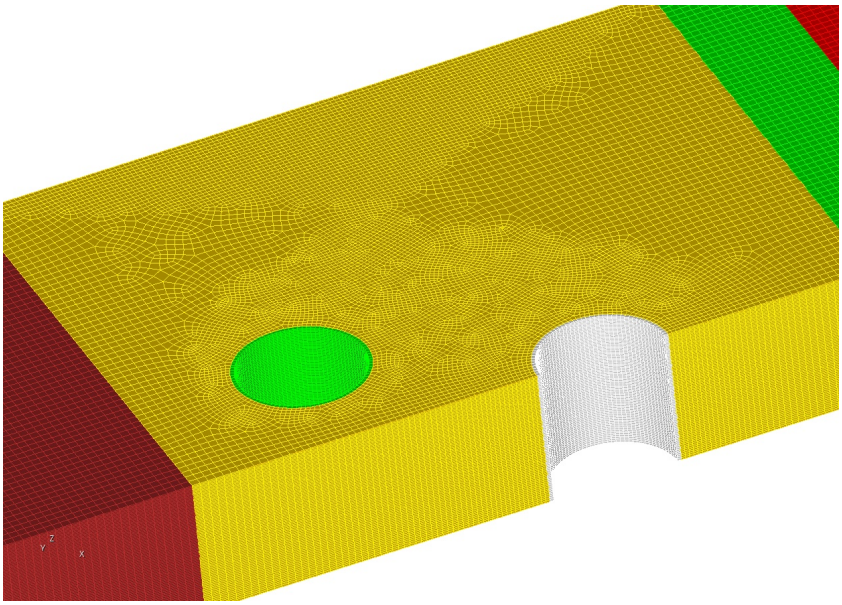

Figure 4.24: Computational mesh for multiple cylinder case (H/h = 0.4, h/D = 0.62). Finer grid size is used in the neighborhood of the cylinder.

cylinders, scattered waves are generated at both cylinders, and they collide with each other in phase at the symmetric plane, combined with the reflected wave from the instrumented cylinder, generating a local breaking wave as the secondary wave crest appearing at the measurement of wave gauge 4. It is also noted that the numerical dissipation takes the role of turbulence model in our inviscid calculation to stabilize the calculation in extreme conditions such as wave breaking.

Figure 4.26 shows the time history of free surface elevations around the instrumented cylinder. The variation of surface elevation around the cylinder is quite similar to what we observed for single cylinder case. And the wave profile at $\theta = 150^\circ$ also shows a tendency of wave breaking.

Figure 4.27 shows the snapshots of free surface on the symmetrical plane. The analytical free surface (dotted line) propagating without the cylinder cluster

is also plotted as a comparison. The free surface around the instrumented cylinder circumference is also projected horizontally onto this plane and presents the surface displacement around the cylinder. Due to the blockage of the front dummy cylinders, the incident solitary wave has been significantly deformed locally before it hits the instrumented cylinder. But the evolution of free surface displacement at the instrumented cylinder face is quite similar to that of single cylinder. Especially, the solitary wave also reverts back to its original shape after it passes the instrumented cylinder by a distance of about 4 times the cylinder radius.

Figure 4.28 presents the three dimensional free surface profiles in the multiple cylinder case. The flow is more violent than that of single cylinder case. The reflected wave from the instrumented cylinder, combined with the water column trapped inside the cylinder grid, generates a strong scattered wave which is propagating upstream and may be about to break.

4.6.2 Run-up on the instrumented cylinder

The solitary wave run-up on the front side of the instrumented cylinder is shown in Figure 4.29. The solitary wave increases by 64% than the normal incident wave height at the cylinder's front side. The numerical result shows a longer trapping time of water trapped inside the cylinder array and indicates a deeper trough. However, the numerical result of leading wave is very satisfactory.

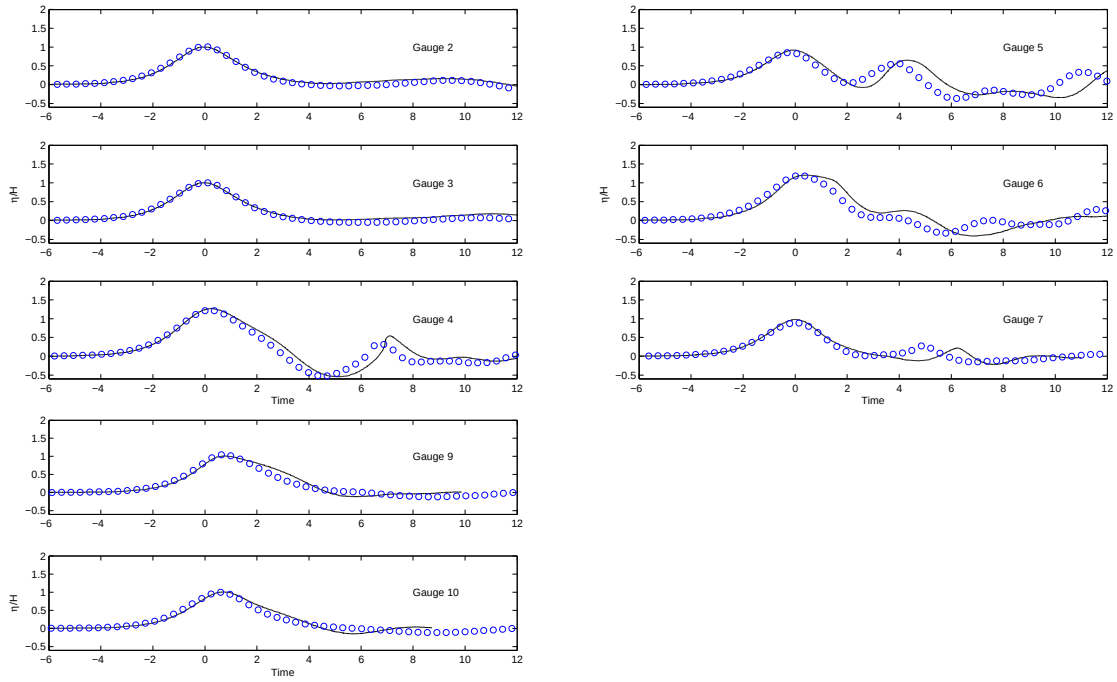

Figure 4.25: Time history of free surface elevations at wave gauges for the one cylinder case. The circles are experimental data and the solid lines are numerical results.

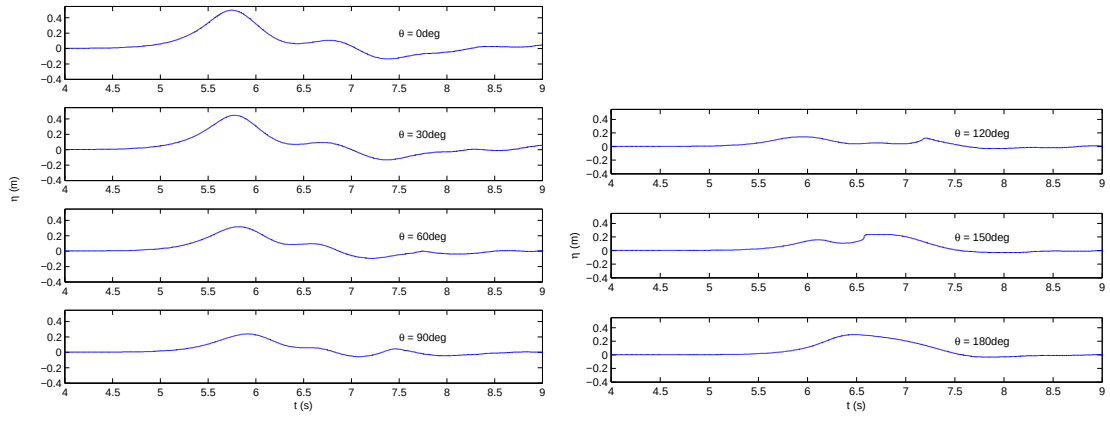

Figure 4.26: Time history of free surface elevations around the instrumented cylinder. $\theta = 0°$ indicates the front side, and $\theta = 180°$ is the back side of the cylinder.

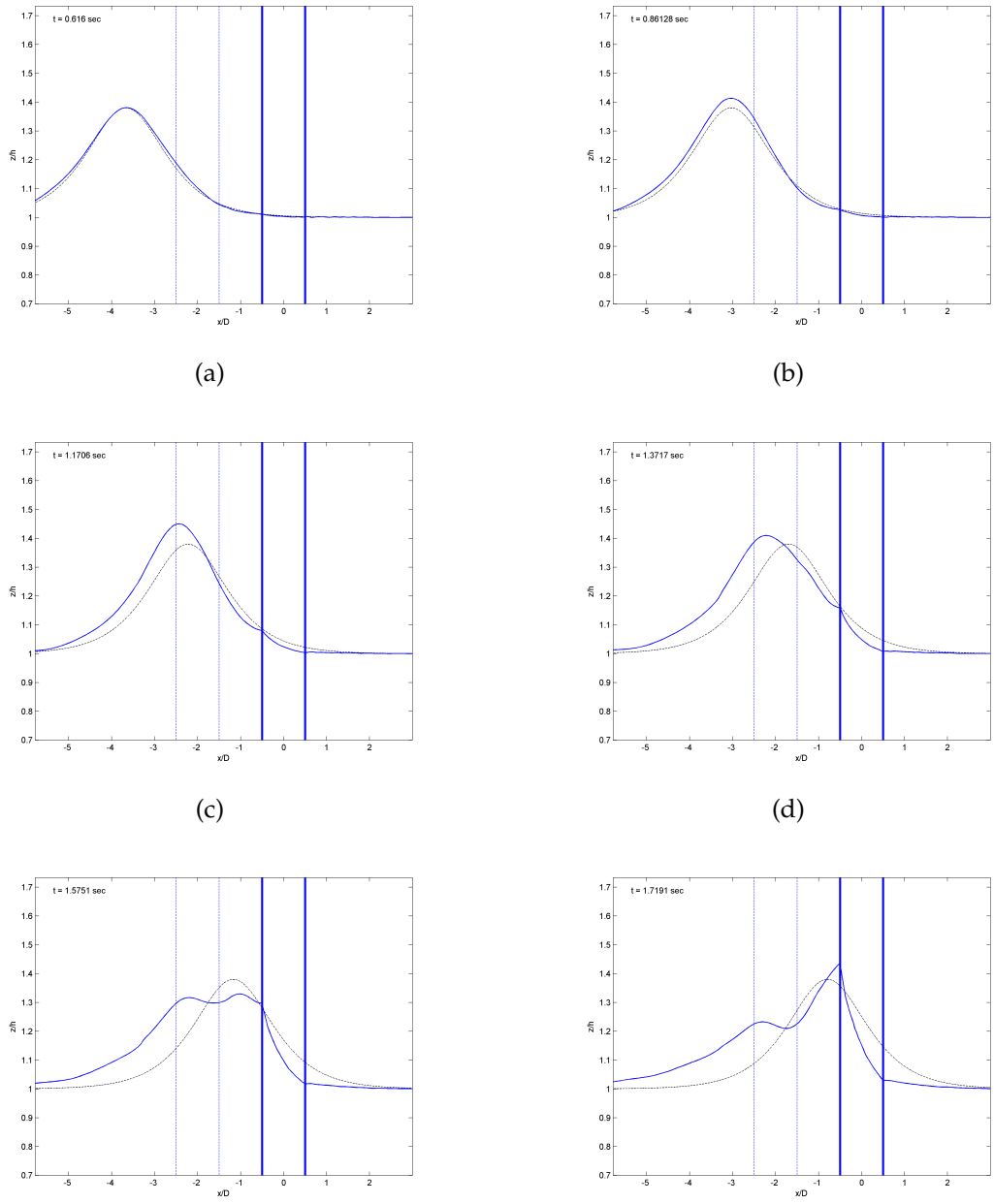

(a) (b) (c) (d) (e) (f)

Figure 4.27: Free surface profile on the symmetrical plane. The vertical dash line indicates the dummy cylinder. The dash line represents the analytical solitary wave profile without the presence of the cylinder as a comparison to the numerical wave. The free surface inside the cylinder range is the horizontal projection of the free surface around the cylinder..

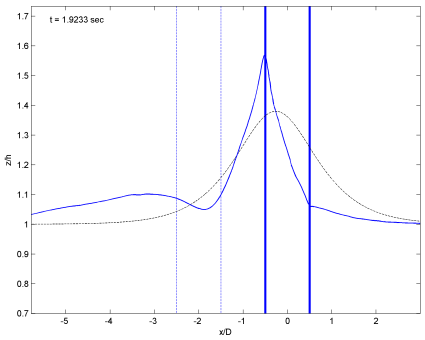

(g)

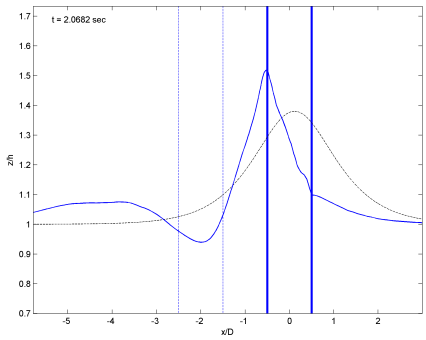

(h)

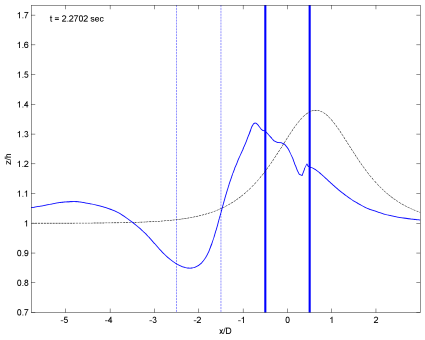

(i)

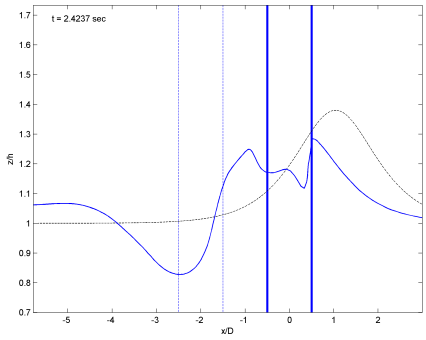

(j)

Figure 4.27: Free surface profile on the symmetrical plane (cont.).

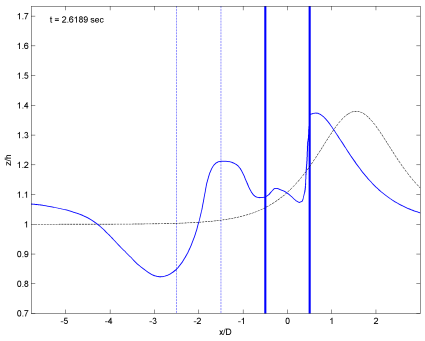

(k)

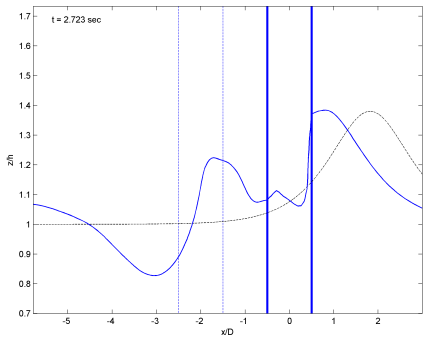

(l)

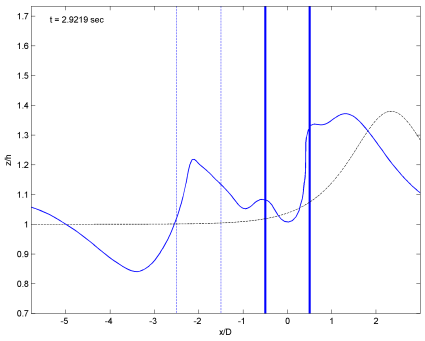

(m)

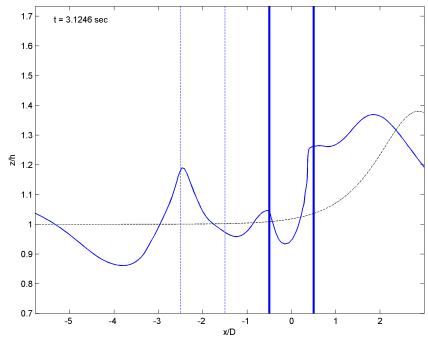

(n)

Figure 4.27: Free surface profile on the symmetrical plane (cont.).

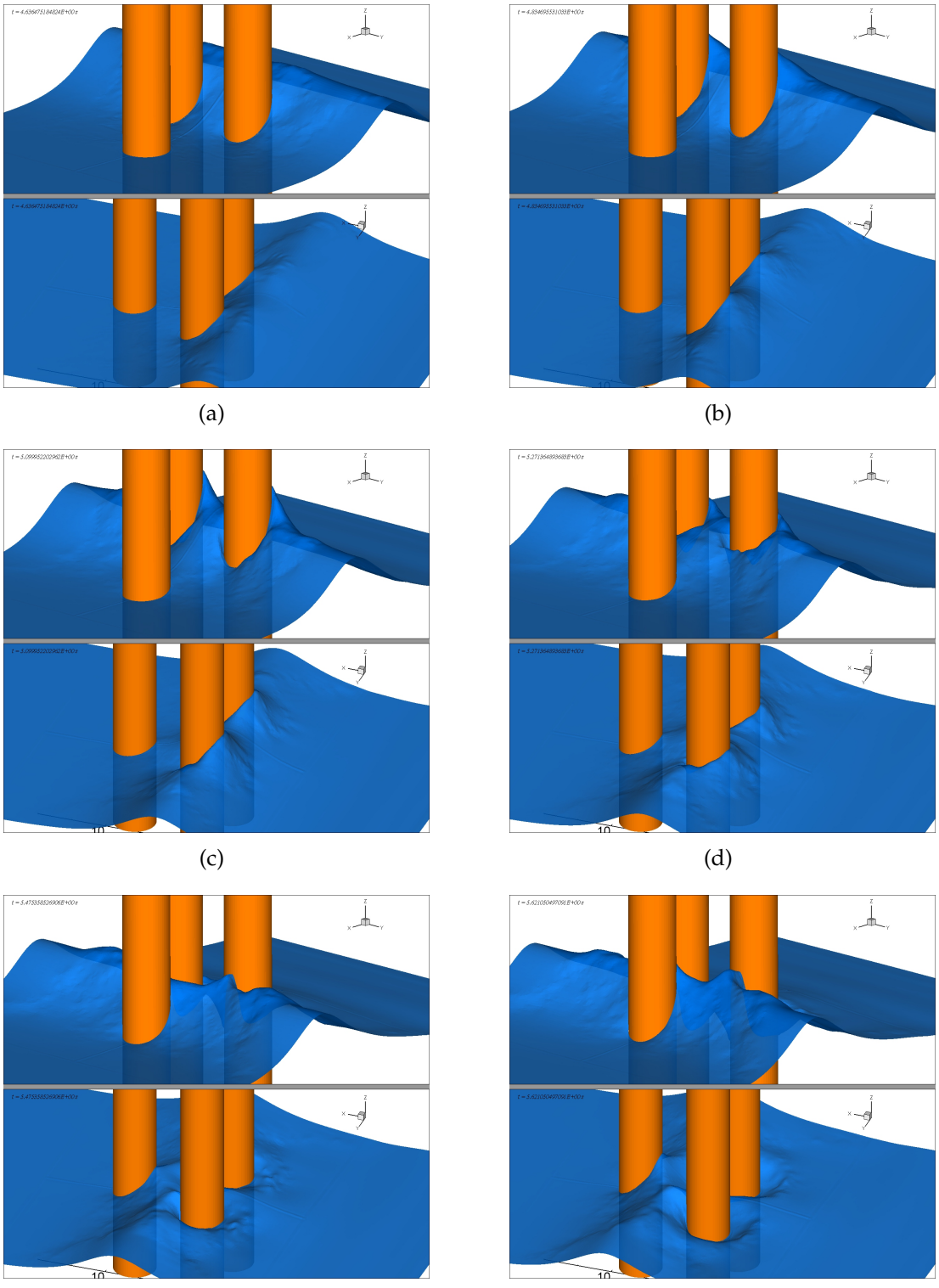

(a) (b) (c) (d) (e) (f)

Figure 4.28: Snapshots of three dimensional free surface profiles. The upper and lower graphs in each subfigure show the three dimensional view from two different view angles.

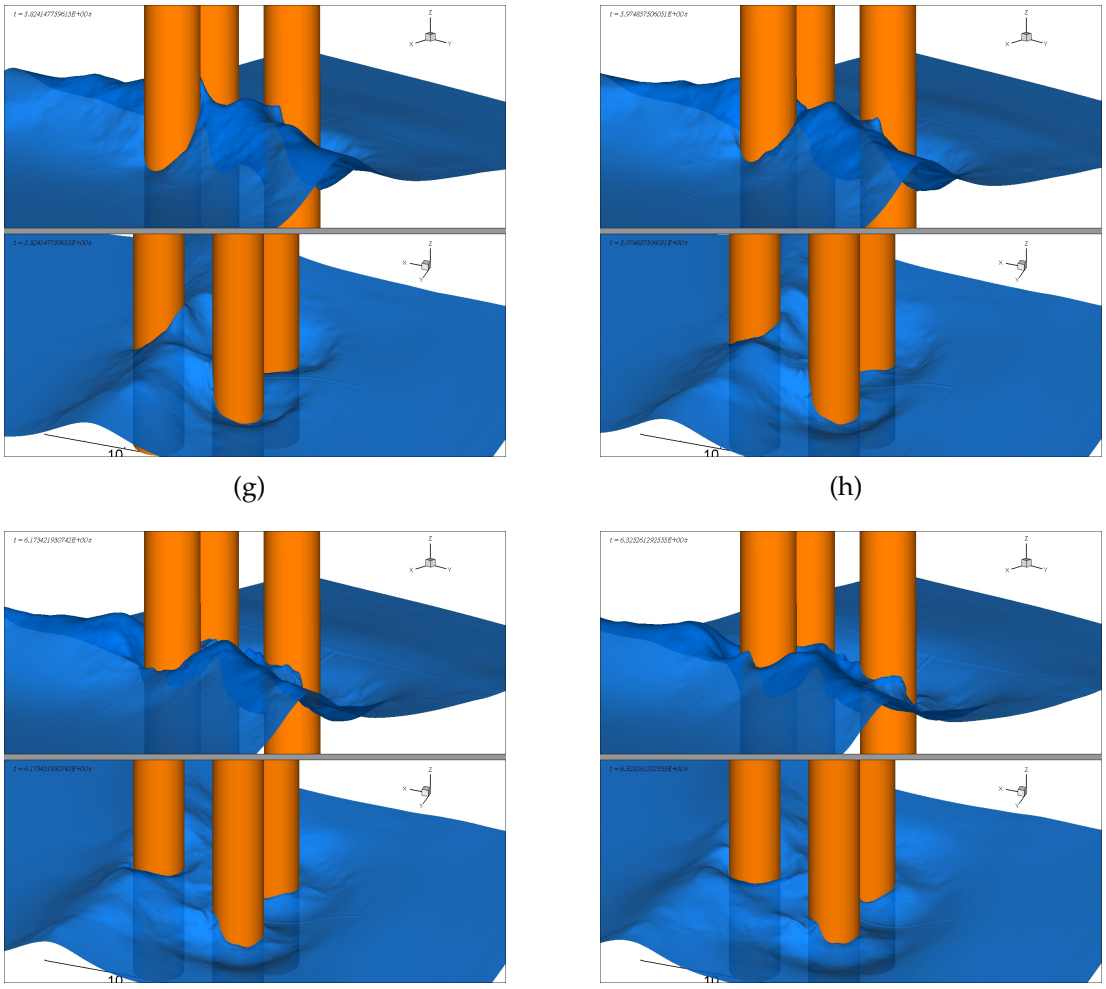

(g) (h)

(i) (j)

Figure 4.28: Snapshots of three dimensional free surface profiles (cont.).

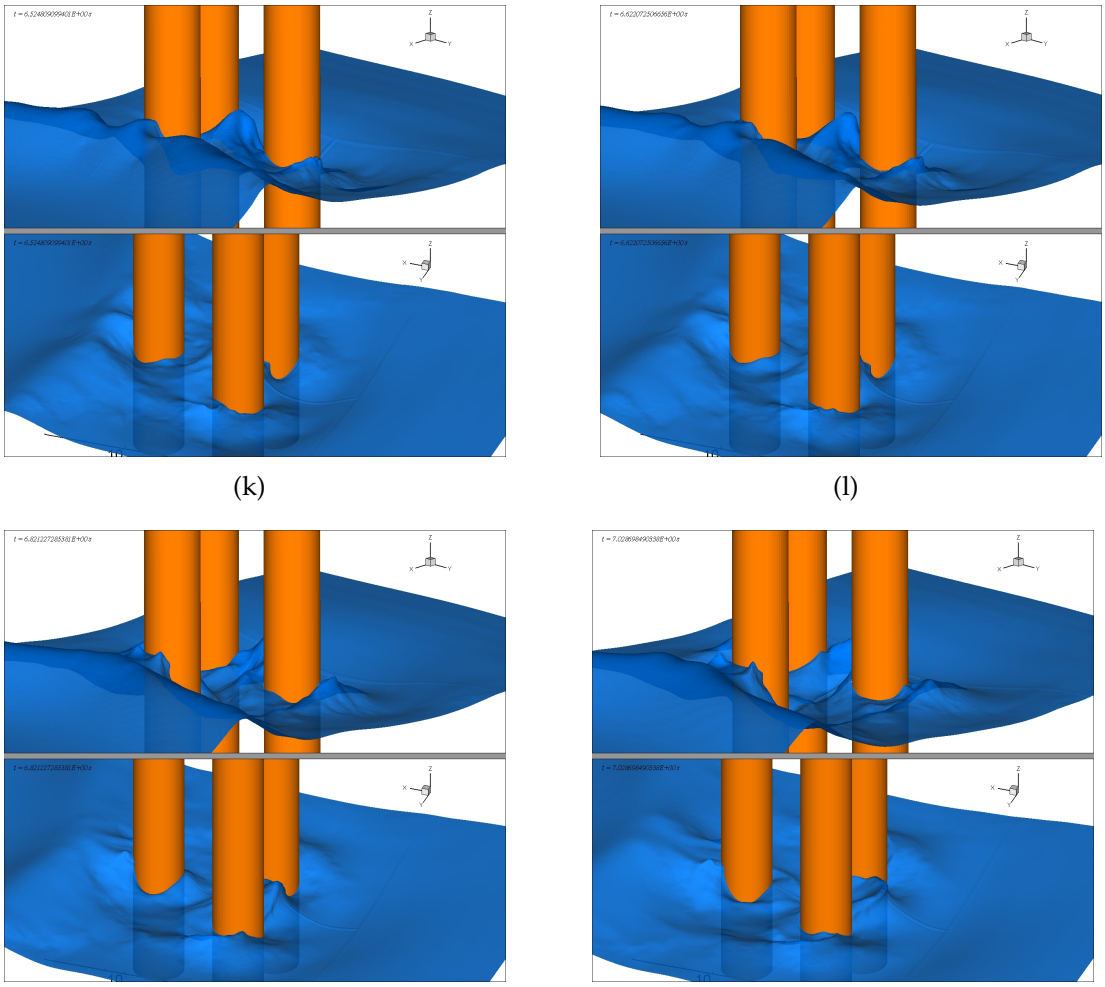

(k) (l)

(m) (n)

Figure 4.28: Snapshots of three dimensional free surface profiles (cont.).

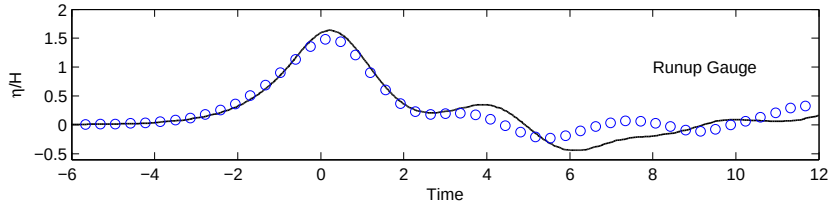

Figure 4.29: Solitary wave run-up on the instrumented cyliner of multiple cylinder case ($H/h = 0.40$, $h = 0.75$m). The circles are laboratory data, and solid line indicates numerical results.

4.6.3 Velocities

Figure 4.30 shows the particle velocity measurements at laboratory ADV locations. The counter-directional lateral flows at the front and back region are also observed, but they are not complementary as they are in the single cylinder case. The front region experiences a longer time of outward lateral flow because of the water trapped inside the cylinder array. As a consequence, the lateral velocity component at ADV 4 shows noticeable positive value. It is noted that numerical lateral velocity at ADV 3 shows a secondary crest which is consistent with the observation of secondary wave crest at wave gauge 5, which is not seen in the laboratory velocity measurement.

The velocity field in the neighborhood of the instrumented cylinders on the horizontal cross-section is similar to that of single cylinder case (The detailed snapshots thus are not presented here). One vortex first appears at the lee side of the cylinder, then a second vortex appears at the location a little behind the middle of the cylinder due to the influence of scattered wave. However, it should be noted that the flow field within the cylinder cluster is more complex because of the complex interaction of scattered waves from the cylinders.

4.6.4 Pressure around the cylinder

Figure 4.31 shows the dynamic pressure response along the front line of the instrumented cylinder in multiple cylinder case.

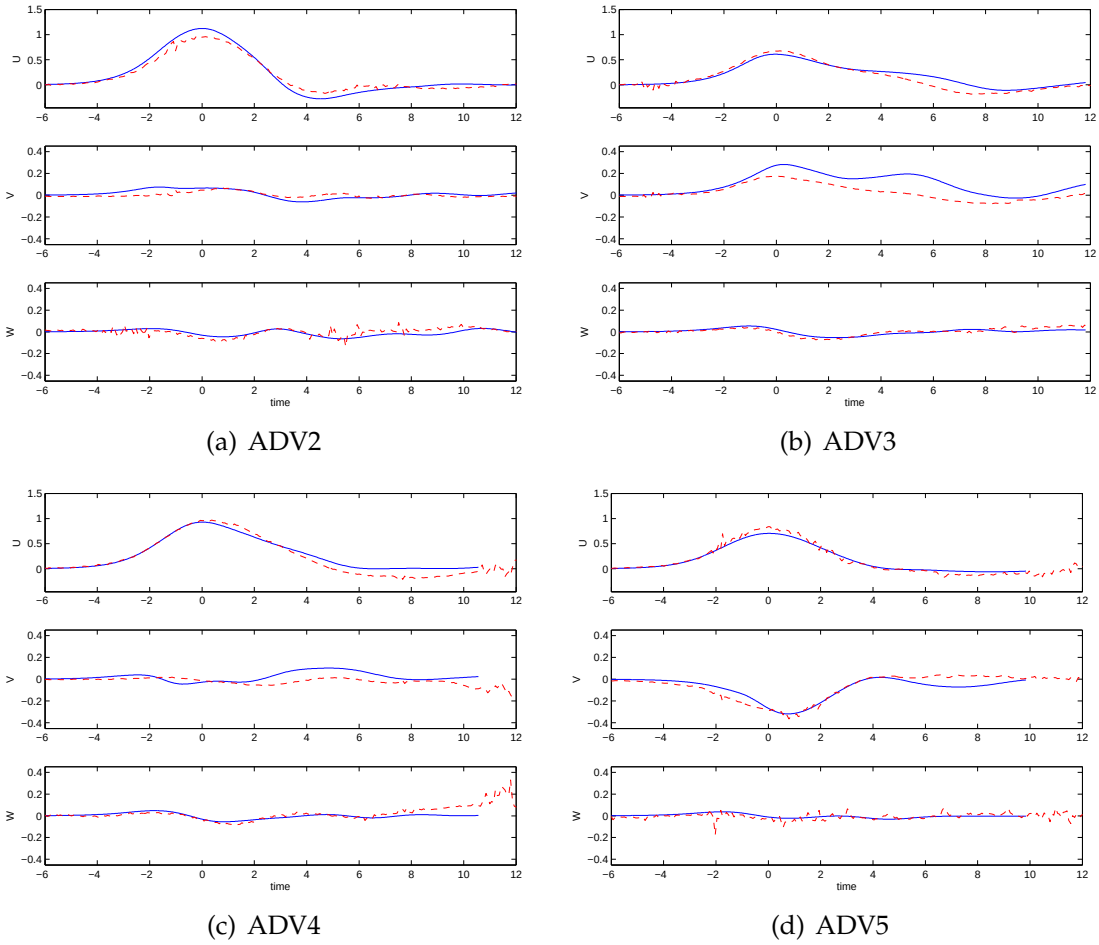

(a) ADV2 (b) ADV3

(c) ADV4 (d) ADV5

Figure 4.30: Time histories of particle velocity components at specified locations for multiple cylinder case. Solid line: numerical results; Dash line: laboratory measurements.

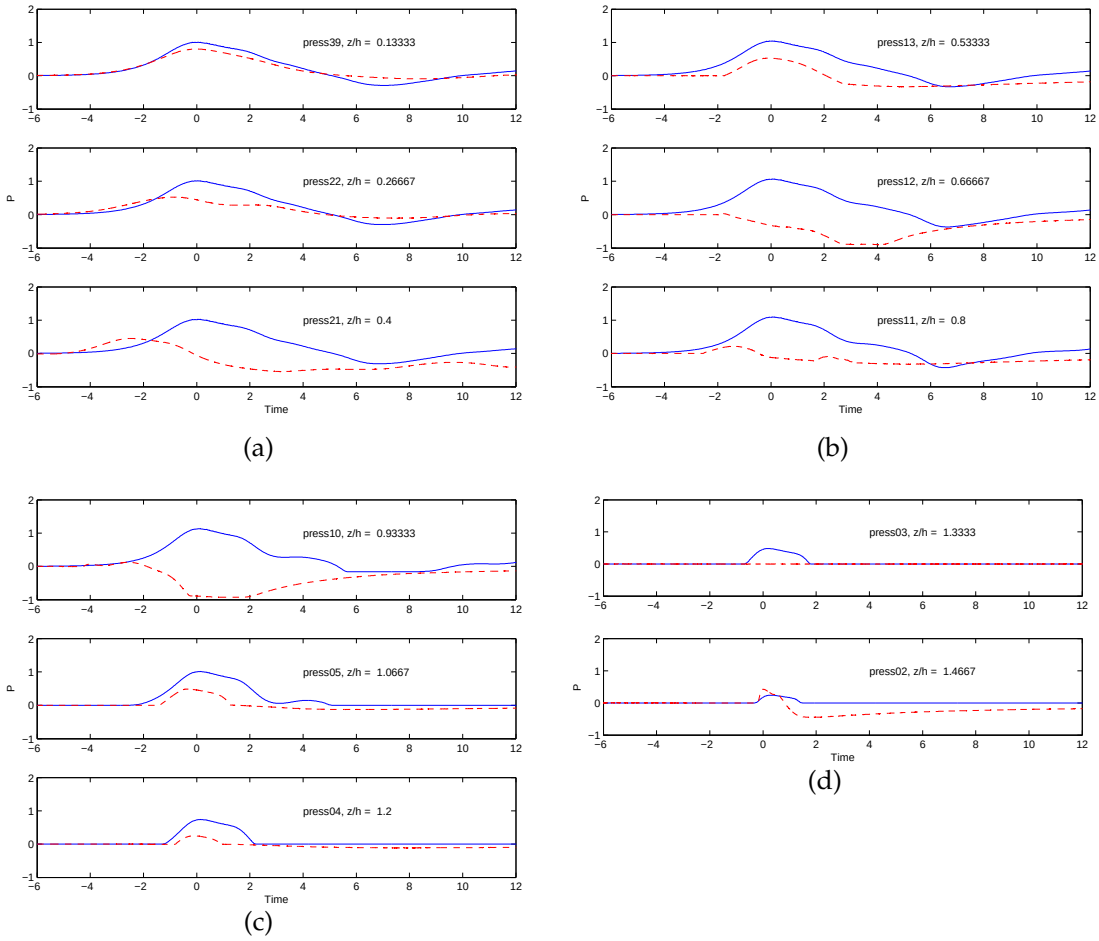

Figure 4.31: Time histories of pressure at the front line of cylinder for multiple cylinder case. Solid line: numerical results; Dash line: laboratory measurements.

4.6.5 Wave load on the cylinder

Figure 4.32 shows the horizontal hydrodynamic force on the instrumented cylinder. Good agreement between the experimental and numerical data is observed.

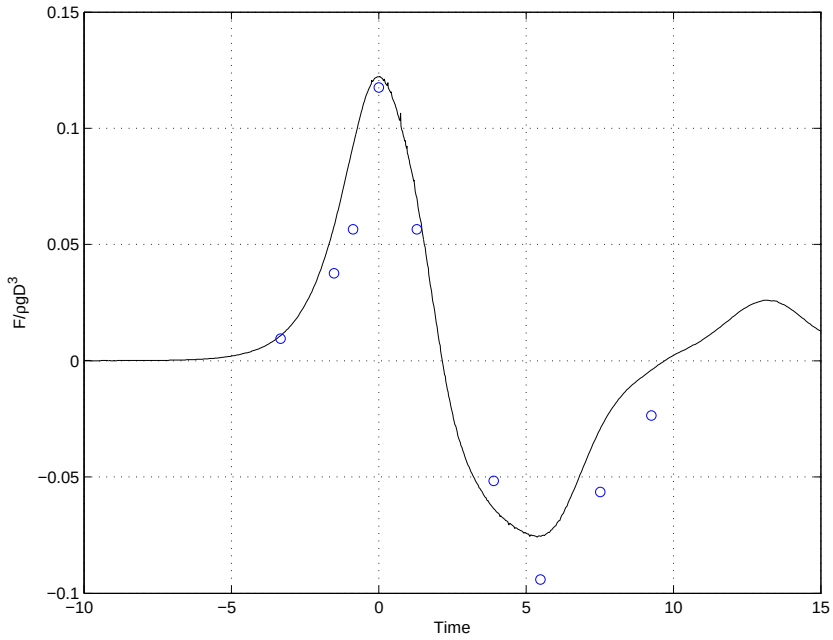

Figure 4.32: Horizontal force on the instrumented cylinder of multiple cylinder case. The circles are laboratory data, and solid line is the numerical results.

4.6.6 Disscussion on the effect of multiple cylinders

Figure 4.33 presents the numerical free surface elevations at specified wave gauge locations for both single and multiple cylinder cases. Although the incident wave conditions are the same, the free surface profiles at wave gauge 6 and 7 show significant difference. The impact wave shape (at wave gauge 6) is

locally deformed in multiple cylinder case because of the scattering by the front two dummy cylinders, and its leading wave has a smaller wave height and a shorter wave length than those of single cylinder case. However, the wave recovers its solitary type at wave gauge 10 in both cases and shows small difference, which indicates that few energy is scattered as the solitary wave passes by the cylinder cluster.

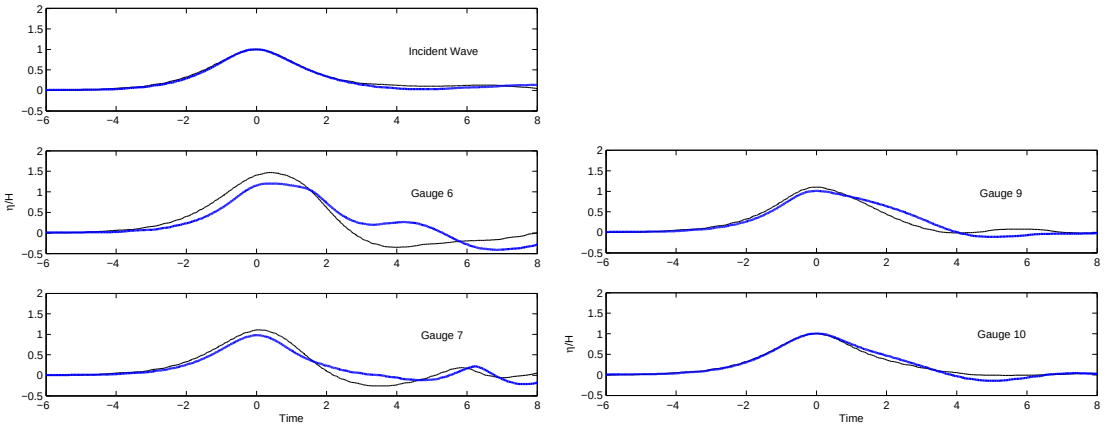

Figure 4.33: Numerical free surface elevations at specified wave gauge locations. The blue thick line denotes the case of three cylinders, and the black thin line represents the single cylinder case.

In Figure 4.34 the free surface displacements around the perimeter of the cylinder are shown for both the case of three cylinders and the one cylinder case. It is also observed that the leading wave in multiple cylinder case shows a smaller wave height and shorter wave length. Due to the blocking of the cylinder, the incident solitary wave deforms locally and a trailing wave is created and propagates along the perimeter of the cylinder. This feature is local in the vicinity of a cylinder and occurs in both one-cylinder and three-cylinders cases. Because of the wave scattering, the maximum wave force is also smaller in the 3-cylinder case as shown in Figure 4.35. The maximum wave force is 1.14 times larger in the single cylinder case. Significant phase difference also appears in

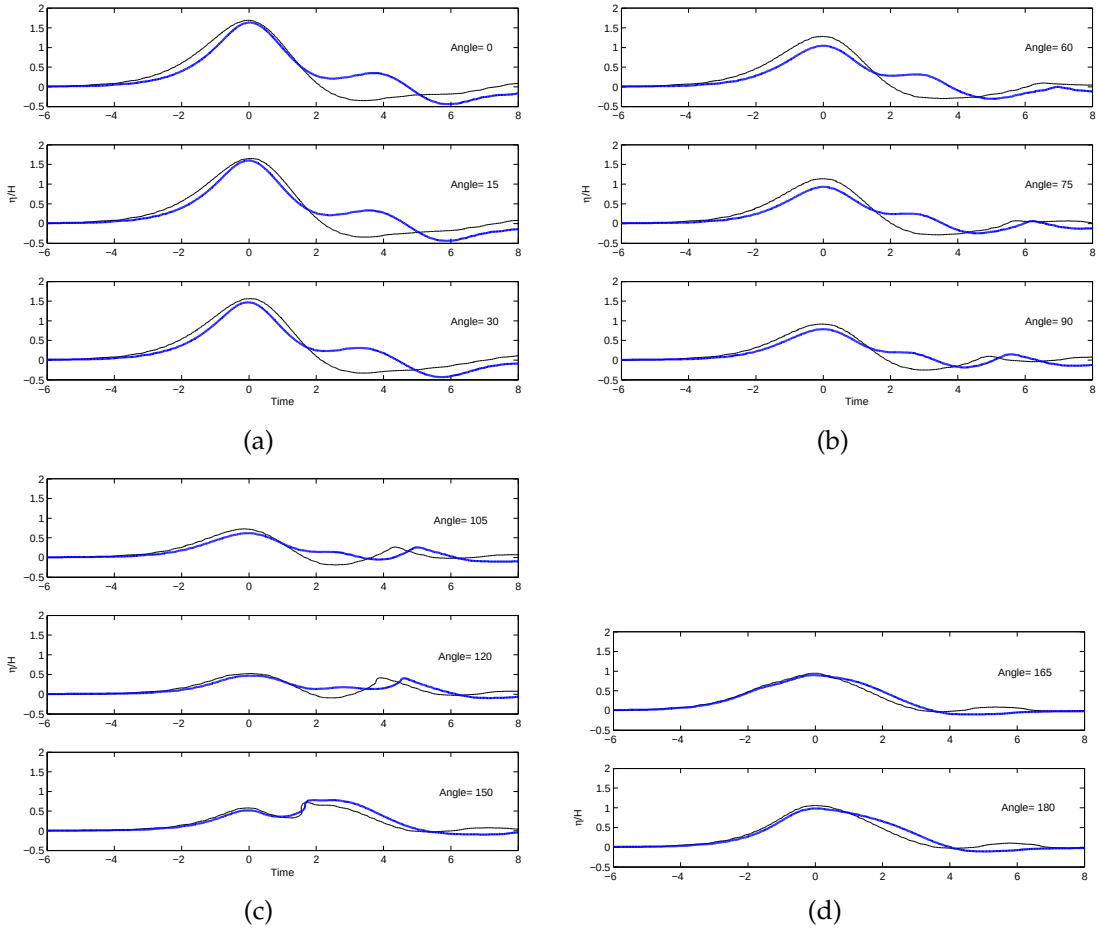

Figure 4.34: Time histories of free surface elevations around the cylinder. The blue thick line denotes the case of three cylinders, and the black thin line represents the single cylinder case.

the force time history because of the interference effect. It is also noted that the second force peak is not only postponed but also approximately two times larger in 3-cylinder case.

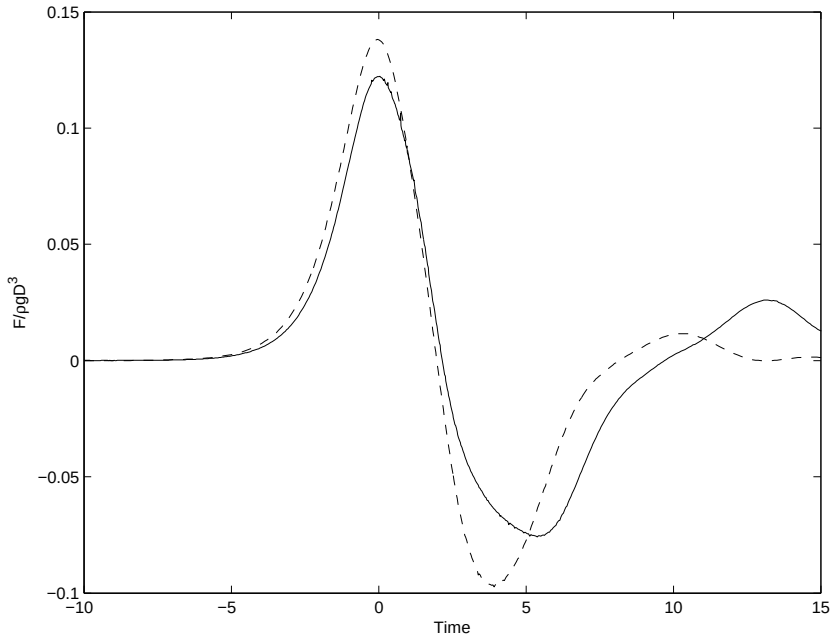

Figure 4.35: Horizontal force on the cylinder. Solid line represents the 3-cylinder case and the dash line the single cylinder case.

4.7 Concluding Remarks

In this chapter, a non-breaking solitary wave is numerically simulated to impinge on a group of fixed rigid circular cylinders. The numerical results, such as free surface displacement, fluid particle velocity, the pressure around the cylinder and the total wave force and run-up, are compared with the laboratory measurements. The good agreements shows that our numerical model is capable of simulating this complex three dimensional wave-structure interaction problem.

The numerical simulation has the advantage of detailed flow information over the whole domain, which is usually quite hard for the laboratory measurements, especially for a large scale experiment like what was discussed in this study. Therefore, detailed numerical solutions, such as three dimensional free surface profile, velocity and pressure fields on sliced planes, are presented and

discussed. It shows that the original two dimensional flow becomes fully three dimensional due to the cylinder group, and that the local flow near the cylinders is complex due to the interaction of the incident wave and scattered waves.

For the single cylinder case, more numerical simulations of extensive wave parameters were performed to supplement the laboratory data. The maximum wave force and run-up were presented as functions of h/D or H/h, and the functions are given as the fitting curves of the numerical results. The results clearly show that the force magnitude or run-up is non-linear with h/D or H/h.

CHAPTER 5

A NUMERICAL INVESTIGATION OF SOLITARY WAVE INTERACTION WITH SLENDER CYLINDER ON A SLOPING BEACH

As ocean wave propagates from deep sea to the coastal region, the wave profile deforms and steepens with increasing wave height and the decrease of wave celerity in the shoaling zone, and may eventually become unstable and break at some region, which is usually called breaking zone. The wave breaking causes many complex phenomena in the surf zone (region between the breaking zone and shoreline), such as beach erosion, sand drift, contaminant transport and so on. Therefore, it is important to understand the flow field in the surf zone. However, the theoretical approaches to study the breaking waves on the sloping beach are still inadequate[50], the laboratory experiments and the numerical simulations are the most common ways for the research of breaking wave phenomena.

Stokes[69] proposed that the wave profile becomes unstable and breaks as the horizontal fluid particle velocity at the wave crest equals to the phase speed at which the wave propagates. McCowan[47] used relative wave height as breaking criterion for the solitary waves, i.e. the solitary wave breaks at

$$\gamma_b = \frac{H_b}{h_b} = 0.78 \tag{5.1}$$

where the subscript b denotes the breaking point. It is often used as breaking index to predict breaking solitary wave on a mild slope. In practice when the wave shoaling profile is available, people usually define the breaking point as the location where the wave front becomes vertical.

The breaking waves at the sloping beach are generally categorized into three

types[18]: spilling, plunging, collapsing and surging breakers. Galvin classified the breaker types of periodic waves by their incident wave height, wave period and beach slope. Similarly, Battjes defined the surf zone parameter ξ_0 to classify the breaker types:

$$\xi_0 = \frac{s}{\sqrt{H/\lambda}} \tag{5.2}$$

where $s = \tan\beta$ is the beach slope, λ the wave length. And the breaker types can be classified quantitatively:

$$\xi_0 = \begin{cases} \xi_0 < 0.5, & \text{spilling breaker} \\ 0.5 < \xi_0 < 3.3, & \text{plunging breaker} \\ \xi_0 > 3.3, & \text{surging breaker} \end{cases} \tag{5.3}$$

For solitary waves, Grilli et al [23] stated that the solitary wave with

$$\frac{H_0}{h_0} > 16.9 s^2 \tag{5.4}$$

will eventually break as it climbs up the beach of a slope s. And a slope parameter S_0, defined as $1.521 s/\sqrt{H_0/h_0}$, is used to predict the breaker type of a solitary wave:

$$S_0 = \begin{cases} S_0 < 0.025, & \text{spilling breaker} \\ 0.025 < S_0 < 0.3, & \text{plunging breaker} \\ 0.3 < S_0 < 0.37, & \text{surging breaker} \end{cases} \tag{5.5}$$

In the past few decades, numerical studies on the breaking waves have become popular due to the increasing computer power and the limitation of laboratory experiments. Grilli [21, 23] used a fully nonlinear wave model based on potential theory to study the shoaling and breaking characteristics of solitary wave on sloping beaches, but their method is restricted to the shoaling process and the early stage of breaking. Lin and Liu [39, 40] successfully applied their

numerical model to the surf zone. They numerically solved the Reynold averaged Navier-Stokes equations with a Reynold stress model closure, and the numerical results agreed well with the laboratory measurements. Bradford [3] also solved the RANS equations to study the spilling and plunging waves over a sloping beach. Watanabe [75, 76] used large eddy simulation to study the turbulence characteristics after wave breaking.

In this chapter, the spilling and plunging solitary waves on a sloping beach will be discussed and compared with laboratory measurements. The turbulence is modeled by large eddy simulation. The impact of a plunging solitary wave unto a vertical cylinder will then be presented.

5.1 Spilling Breaker on a Mild Slope

5.1.1 Laboratory and Numerical Setup

The laboratory setup is shown in Figure 5.1. A highly nonlinear solitary wave of $H_0/h_0 = 0.73$ is generated by the wave maker and breaks at a beach of $1:50$ slope. The solitary wave is close to breaking according to the breaking index proposed by McCowan [47] which serves as a good prediction on very mild slopes. The still water depth is $h_0 = 0.3$m, and the wave height is $H_0 = 0.22$m. 24 resistance-type wave gauge are installed to measure the evolution of wave profile. And 7 ADVs are employed well inside the surf zone at different heights.

The numerical domain and coordinate system are shown in Figure 5.2. The grid is non-orthogonal, and its characteristic size are $\Delta x = 1.5$cm, $\Delta y = 3.0$cm, $\Delta z = 1.0$cm. 25 numerical wave gauges are placed along the center line in the

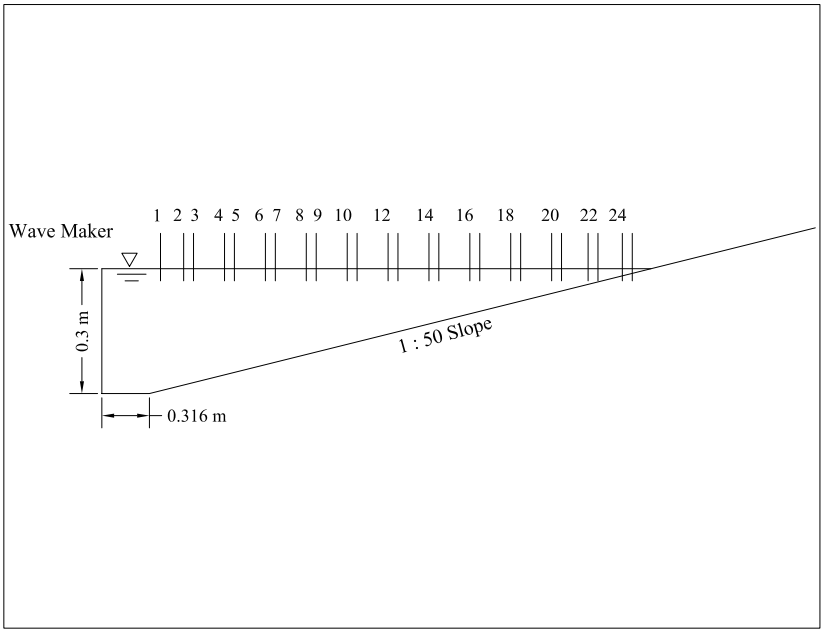

Figure 5.1: Sketch of laboratory setup

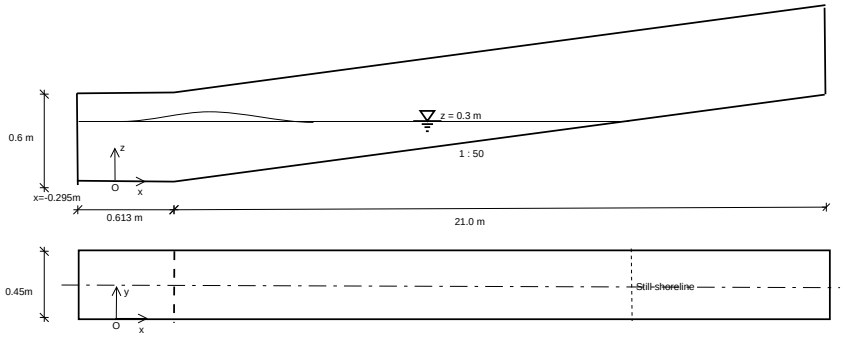

Figure 5.2: Sketch of computational domain.

domain as done in the laboratory experiments. Their locations are listed in the Table 5.1. One other numerical gauge is placed at x = 7.69m, which corresponds to the laboratory ADV location, to collect the numerical velocity information. Numerical velocities at 7 different heights above the bottom (10, 30, 50, 70, 100, 110, 330 mm) will be compared with laboratory measurements.

The solitary wave is generated by numerically simulating the wave piston

Table 5.1: Numerical wave gauge. h is the local water depth.

	1	**2**	**3**	**4**	**5**	**6**	**7**	**8**	**9**	**10**
x (m)	0.99	2.23	2.64	3.23	3.64	4.23	4.64	5.23	5.64	6.23
h (m)	0.286	0.262	0.253	0.242	0.233	0.222	0.213	0.202	0.193	0.182
	11	**12**	**13**	**14**	**15**	**16**	**17**	**18**	**19**	**20**
x (m)	6.64	7.23	7.64	8.23	8.64	9.23	9.64	10.23	10.64	11.23
h (m)	0.173	0.162	0.153	0.142	0.134	0.122	0.114	0.102	0.094	0.082
	21	**22**	**23**	**24**	**25**					
x (m)	11.64	12.23	12.64	13.23	13.64					
y (m)	0.074	0.062	0.054	0.042	0.034					

movement based on Goring's long wave generation theory. It is shown later that our numerical code generates rather good solitary waves. The upper boundary is zero pressure Dirichlet boundary. The bottom is no-slip solid wall, and the lateral boundaries are free-slip solid walls.

Since the wave breaks at the sloping beach, turbulence model has to be incorporated to account for the turbulence effect. In this study, we use both classical Smagorinsky sub-grid model and Yakhot RNG SGS model. The Smagorinsky coefficient is the only user-input parameter in the models. It is usually suggested Cs = 0.1–0.2, and it may take a value smaller than 0.1 for shear flows. We choose Cs = 0.15 which is the median between 0.1 and 0.2, and Cs = 0.08 which is usually used for shear flows.

5.1.2 Wave Shoaling and Breaking

In this section, the numerical results from various LES subgrid models are presented and discussed here. The free surface elevation at each gauge and the velocity profiles are compared to the laboratory data.

In both laboratory and numerical experiments, the free surface elevations are measured by wave gauges at different locations along the beach. Table 5.2 lists the locations of the wave gauge which measures the maximum wave elevation in space and time among all gauges. The position of maximum wave height during the wave shoaling and breaking process should be close to this gauge location, i.e. in the range of $x \pm 50$cm. The results of all numerical simulations are well within the range around the laboratory gauge location, and the local wave steepness H_i/h_i is consistent with the laboratory data. Smagorinsky model with $Cs = 0.08$ and RNG model with $Cs = 0.15$ give the closest results to the laboratory data, which is also shown in Figure 5.3. This is reasonable since smaller Cs value is favorable in the shear flow for Smagorinsky model, and that $Cs = 0.08$ for RNG model seems too small to trigger the turbulence. Although the breaking point locations are different, the shoaling rate dH_i/dx in the shoaling zone are very close, so are the decay rate dH_i/dx in the surf zone. It is also noticed that the envelops of Smagorinsky model ($Cs = 0.15$) and RNG model ($Cs = 0.15$) results coincide with each other in the surf zone, which is consistent with the performance of RNG model that converges the classical Smagorinsky model in strong turbulent flow. And the wave heights of Smagonrinsky model result in the shoaling zone are smaller than those of RNG model, because the classical Smagorinsky model always exhibits significant artificial turbulent dissipation in the shoaling zone while the RNG model does not.

Table 5.2: Location of the wave gauge which measures the maximum surface elevation in numerical and laboratory experiments. H_i is the local wave height, h_i the local water depth and h_0 the still water depth over the flat bottom.

	x (m)	H_i (m)	h_i (m)	H_i/h_i	H_i/h_0
Smagorinsky: $Cs = 0.15$	3.93	0.221	0.228	0.97	0.74
Smagorinsky: $Cs = 0.08$	3.41	0.230	0.238	0.97	0.77
RNG: $Cs = 0.15$	3.81	0.225	0.230	0.98	0.75
RNG: $Cs = 0.08$	4.26	0.216	0.221	0.98	0.72
Laboratory	3.64	0.229	0.234	0.97	0.75

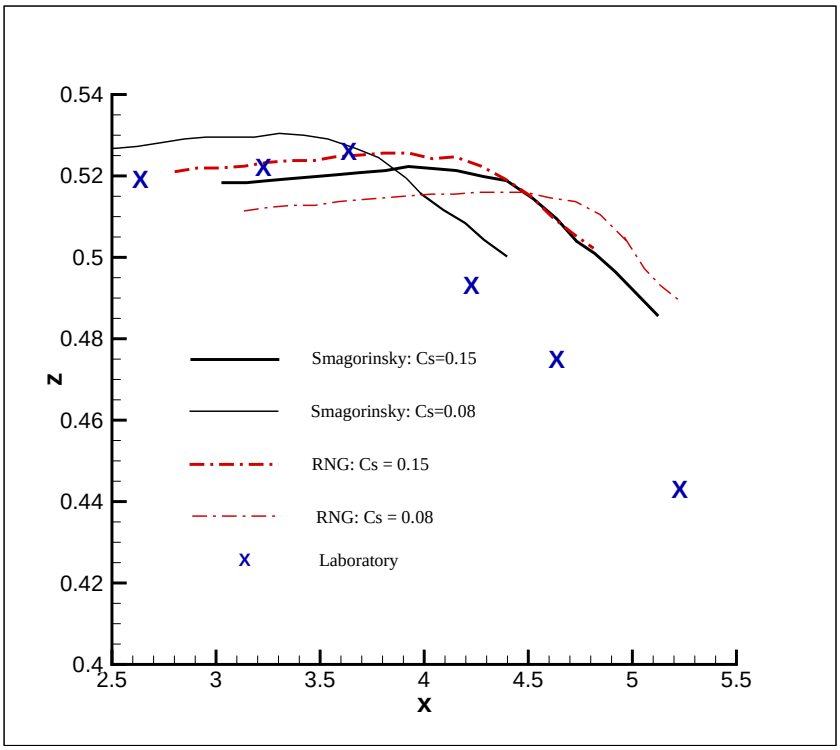

Figure 5.3: Envelop of maximum free surface elevations. z is the vertical coordinate with $z = 0$ at the flat bottom. Unit is in meters.

5.1.3 Comparison with laboratory results

Figure 5.3 shows that all the turbulence calculation produce the overall shoaling and breaking process fairly well in terms of its shoaling and decaying rate, although the numerical waves break at different locations. It is also confirmed by the comparison of numerical and laboratory free surface elevation at the wave gauges. Figure 5.4 shows the numerical results of Smagorinsky sub-grid model calculation ($Cs = 0.15$). Results of other numerical simulations show similar patterns and are thus not shown here.

Figure 5.4(a) shows the free surface elevation near the beach toe. The solitary just leaves the wave maker and has not yet been influenced significantly by the variation of the geometry. The good agreement at this gauge demonstrates good performance of the numerical wave generation code. In general, the numerical free surface profile agrees well with the laboratory data. Figure 5.4(c) shows large discrepancy between numerical and laboratory results. This is due to the difference in the onsets of wave breaking. However, with the strong turbulence dissipation, the wave decays very quickly in a short region, and the numerical breaking wave becomes close to the laboratory data in the middle and inner surf zones ($x > 7.23$m).

Figure 5.5 shows the histories of velocity components at different heights in the inner surf zone. In general, numerical results underpredict their peaks. The numerical vertical velocity component shows an obvious crest after the first one; this discrepancy may be due to the sawtooth shape of the free surface.

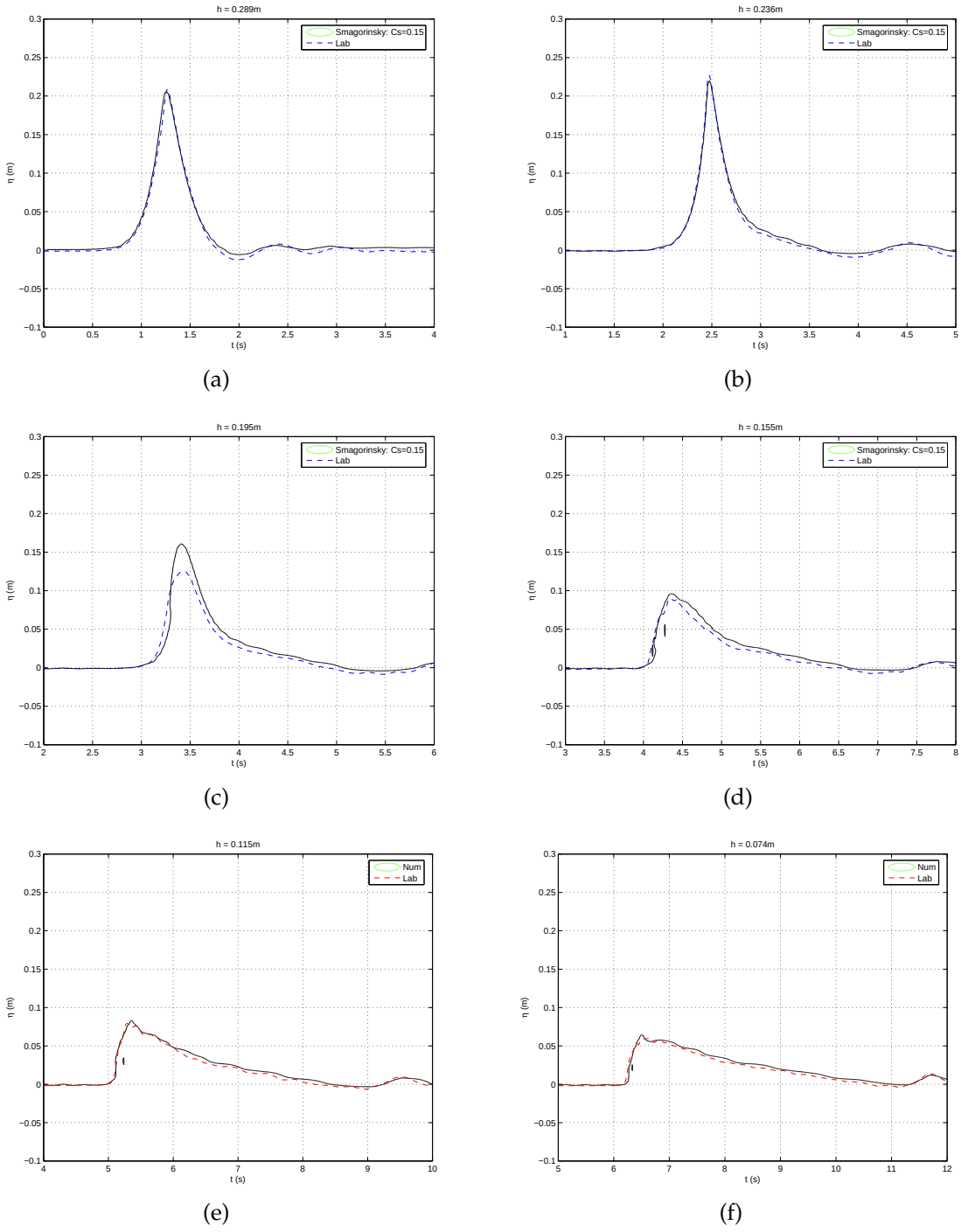

Figure 5.4: Free surface elevation at wave gauges. Solid: numerical results; dash: laboratory data.

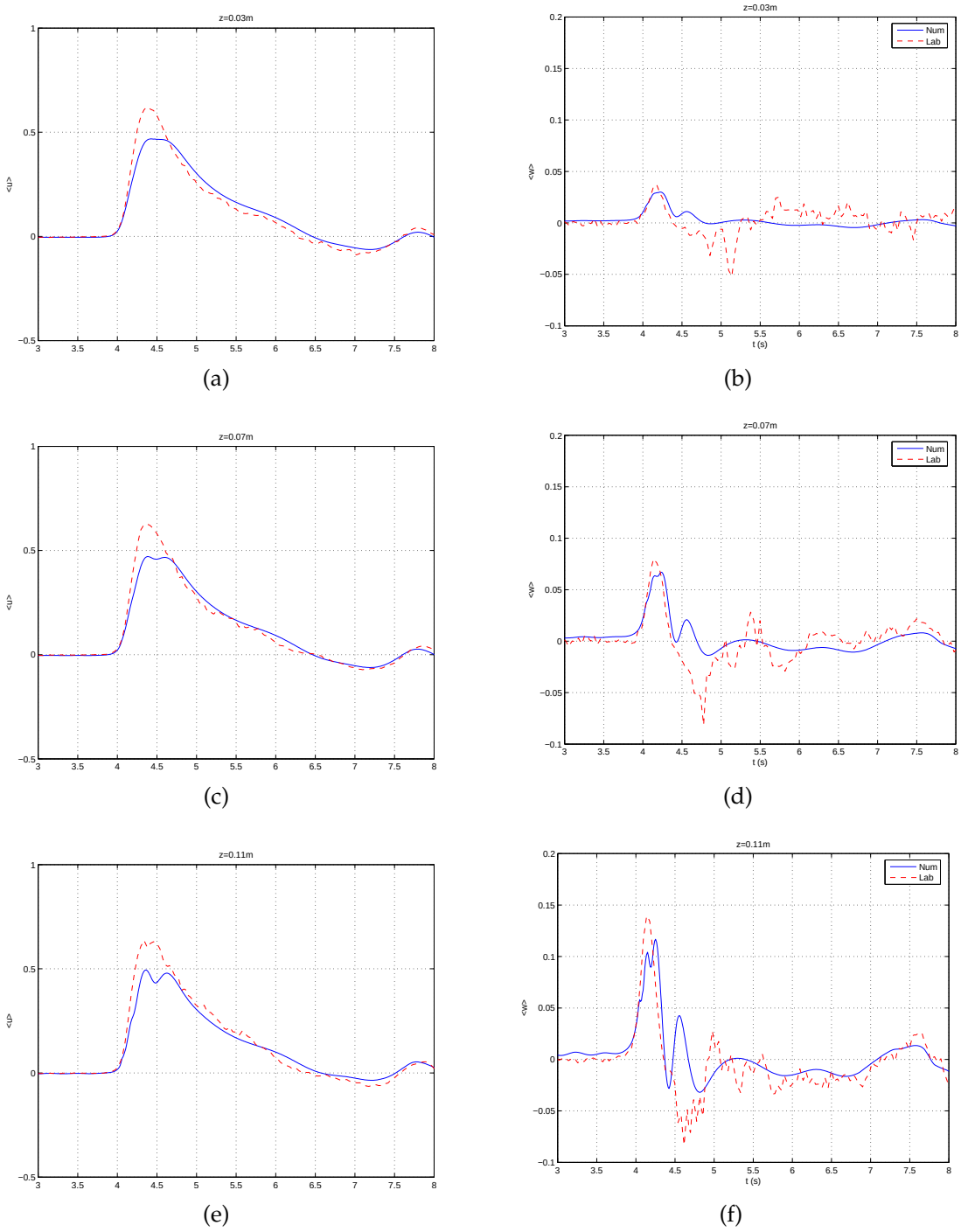

Figure 5.5: Velocity measurements at ADVs. z is the height above the bottom. Solid: numerical results; dash: laboratory data. Left: horizontal velocity component; right: vertical velocity component

5.1.4 Comparions between numerical results

First, the numerical results of two Smagorinsky sub-grid models are compared in Figure 5.6. It is found that the numerical solution is not very sensitive to the Cs value by comparing the surface elevations and the velocities at different heights from the bottom at each gauge. But Cs does have some effect on where the wave breaks and how it decays in the zone near the breaking point. Larger Cs value also renders smaller incident wave height, since larger Cs means larger turbulent viscosity.

Figure 5.7 shows the comparison between Smagorinsky and RNG LES models. In general, the two numerical results are quite close. However, the Smagorinsky model shows more dissipation in the shoaling zone because the turbulent viscosity is always non-zero. And RNG LES model has its advantage in modeling the transition from laminar (or low turbulent) state to highly turbulent flow.

5.1.5 Convergence test

It is always a primary concern in the numerical simulation that the numerical result is grid-independent or convergent. Numerical simulations on a finer mesh were performed for this purpose. The grid size in x and z direction are cut by a half while the grid size in y direction remains the same. This is mainly because of the computational resources limitation. However, we noticed that the flow field changes very little in the transverse direction, therefore the grid size in y direction does not influence much the accuracy of capturing the physics. In addition, the aspect ratio $\Delta x/\Delta y = 1:4$, $\Delta z/\Delta y = 1:6$ are also acceptable. Fig-

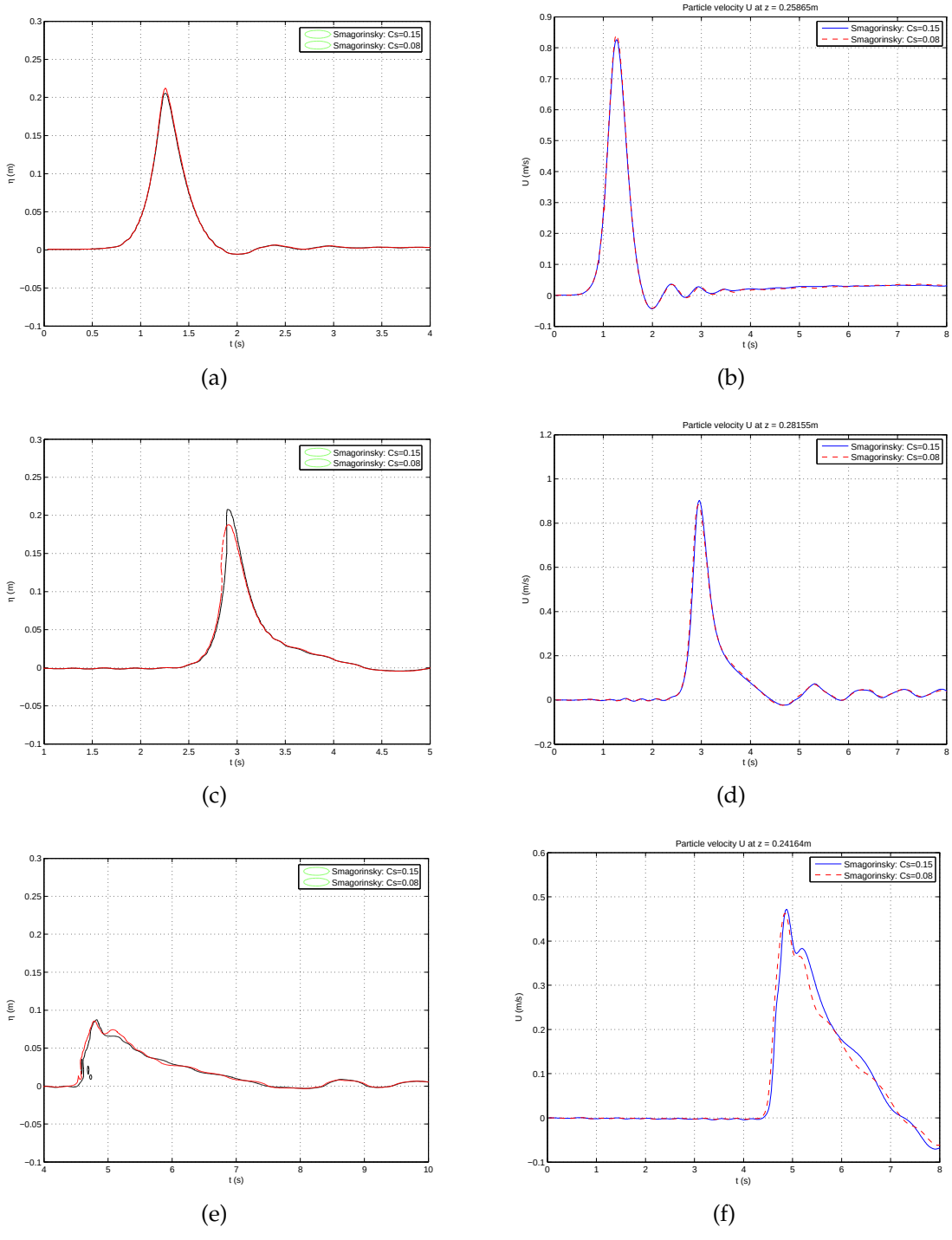

Figure 5.6: Free surface and horizontal velocity component at the wave gauge locations. From top to bottom: $x = 0.99$m, 4.64m, 8.64m. Left: free surface elevation (Black: $Cs = 0.15$; red: $Cs = 0.08$). Right: horizontal velocity component (Solid: $Cs = 0.15$; dash: $Cs = 0.08$)

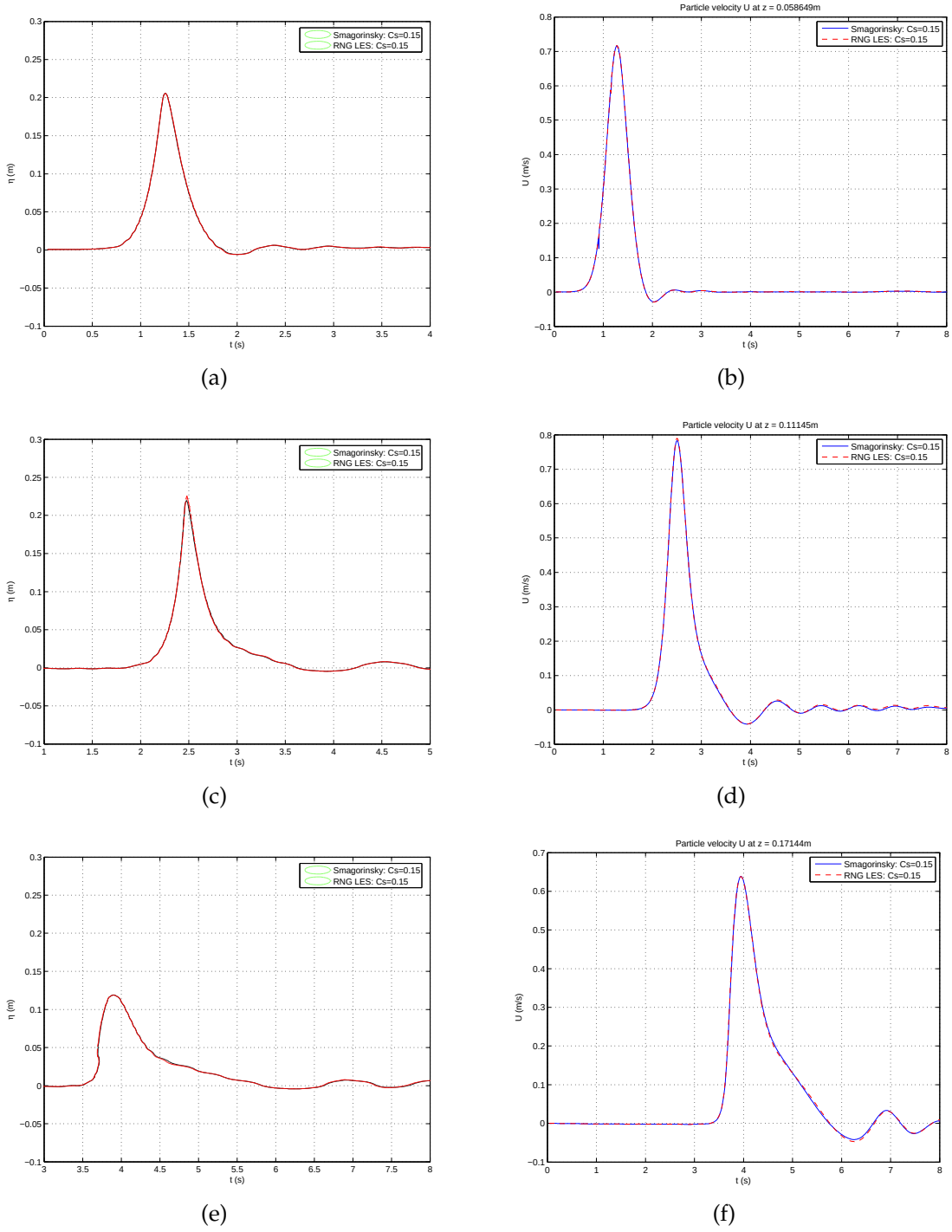

Figure 5.7: Free surface and horizontal velocity component at the wave gauge locations. From top to bottom: x = 0.99m, 3.64m, 6.64m. Left: free surface elevation (Black: Smagorinsky; red: RNG). Right: horizontal velocity component (Solid: Smagorinsky; dash: RNG

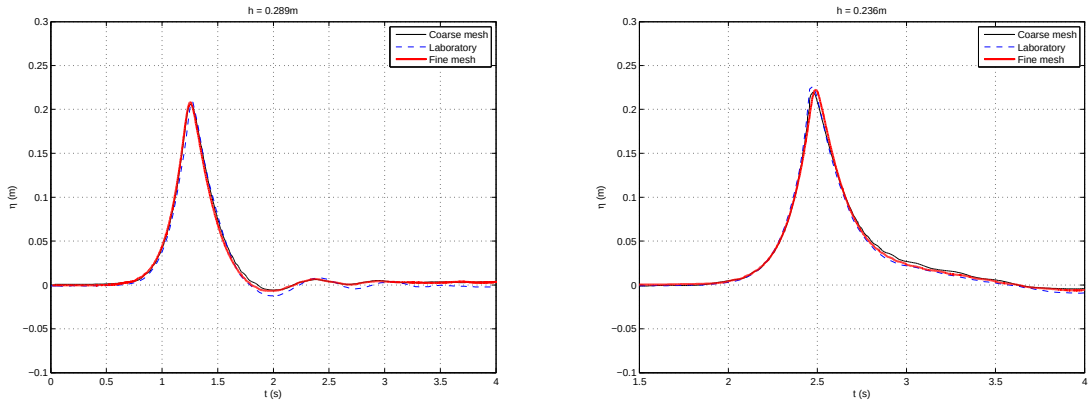

(a) (b)

Figure 5.8: Numerical results on coarse and fine meshes. Black: coarse mesh; red: fine mesh; dash: laboratory.

ure 5.8 presents the numerical results of free surface for coarse and fine mesh calculations, and it shows that the numerical results converge.

5.1.6 Energy dissipation

As discussed in Chapter 3, the energy is conserved as the numerical solitary wave of $H/h = 0.3$ propagates in a constant water depth, which means that the numerical dissipation is small in the simulation.

From the filtered momentum equation, we can derive the kinetic energy transport equation:

$$\frac{DE_f}{Dt} - \frac{\partial T_i}{\partial x_i} = -\varepsilon_f - Pr + g_j U_j \tag{5.6}$$

where $E_f = \bar{U}_i \bar{U}_i/2$ is the kinetic energy of the filtered velocity field; T_i is the energy flux; $\varepsilon_f = 2\nu \bar{S}_{ij} \bar{S}_{ij}$ the viscous dissipation directly from the filtered velocity field; $Pr = -\tau_{ij} \bar{S}_{ij}$ the rate of production of residual kinetic energy; g_j is the gravitational acceleration.

Integrate eq 5.6 over the whole domain:

$$\frac{D}{Dt}\int_{\Omega} E_f d\Omega - \int_A T_i \cdot n_i dA = -\int_{\Omega}(\varepsilon_f + Pr)d\Omega - \int_{\Omega} g\frac{dz}{dt}d\Omega \tag{5.7}$$

The first term is the rate of change of the total kinetic energy ($E_k = \int_{\Omega} u^2/2 d\Omega$), $\frac{D}{Dt}\int_{\Omega} E_f d\Omega = dE_k/dt$; the second term $\int_A T_i \cdot n_i dA$ is zero since there is no energy flux across the domain boundaries in our problem; the third term is the rate of total energy dissipation, $-\int_{\Omega}(\varepsilon_f + Pr)d\Omega = -\frac{dE_B}{dt}$; the fourth term is the rate of change of the total potential energy ($E_p = \int_{\Omega} gz d\Omega$), $-\int_{\Omega} g\frac{dz}{dt}d\Omega = -\frac{dE_p}{dt}$.

Using the new notations, eq 5.7 can be re-expressed as:

$$\frac{DE_k}{Dt} = -\frac{dE_B}{dt} - \frac{dE_p}{dt} \tag{5.8}$$

Integrate eq 5.8 over time:

$$E_k - E_{k0} = -\int_{t_0}^{t} \frac{dE_B}{dt}dt - (E_p - E_{p0}) \tag{5.9}$$

or

$$E_{k0} + E_{p0} = \int_{t_0}^{t} \frac{dE_B}{dt}dt + E_p + E_k \tag{5.10}$$

Eq 5.10 establishes the energy relationship in the ideal numerical simulation (i.e. no numerical error). If numerical error is present, its effect can be modeled as a dissipation term E_n, and eq 5.10 becomes:

$$E_{k0} + E_{p0} = \int_{t_0}^{t} \frac{dE_B}{dt}dt + \int_{t_0}^{t} \frac{dE_n}{dt}dt + E_p + E_k \tag{5.11}$$

Figure 5.9 shows the energy history of three types of numerical simulations: LES, DNS and inviscid calculation. DNS means solving the Navier-Stokes equation on a coarse mesh. After the wave breaks, the wave decays very quickly, producing a quick drop of potential energy. As the breaking wave moves towards

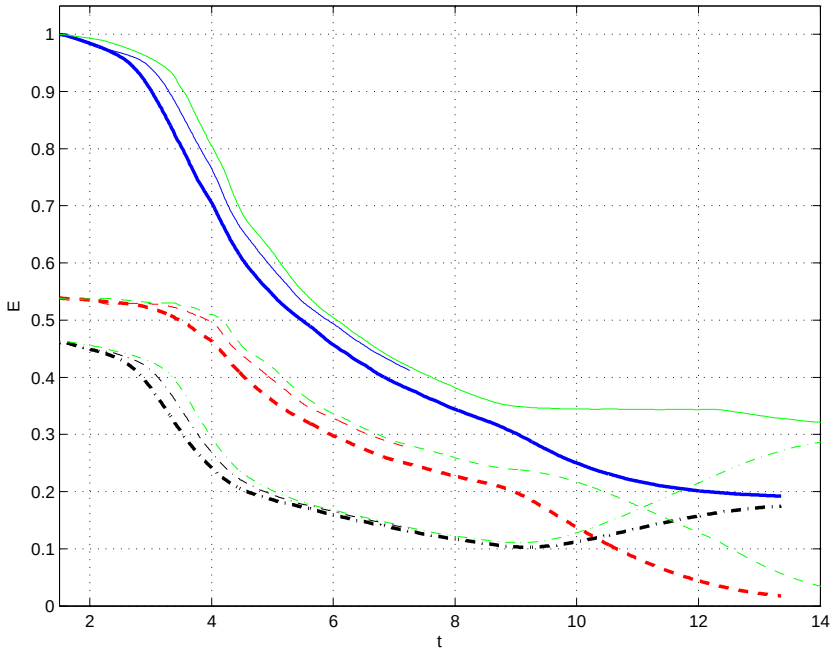

Figure 5.9: Energy history. Thick blue line: LES; thin blue line: DNS; green line: Inviscid. Solid: total energy E_t; dash: kinetic energy E_k; dash-dot: potential energy E_p.

the shoreline, the potential energy decreases and converted to kinetic energy. Due to the strong turbulent dissipation. the kinetic energy also decreases, so does the total energy. All three numerical calculations show the similar energy history curves. It should be noted that the energy dissipation in LES simulation is based on physical assumptions and model, while that of inviscid calculation is subject to the dissipative numerical scheme. However, the comparison of inviscid and LES results reveals that the turbulent dissipation is as the magnitude as the numerical dissipation. But the inviscid calculation shows no sign of energy loss in swash zone while the LES calculation still demonstrates the energy dissipation which can be only attributed to turbulent viscosity. The reason could be that the turbulence is not so strong in this type of spilling breaker that the numerical simulation needs time to develop a highly turbulent flow.

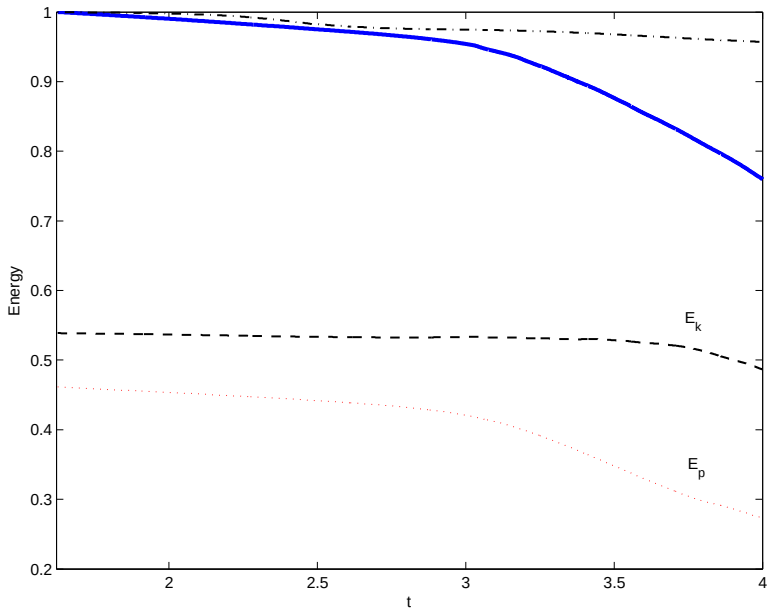

Figure 5.10: Energy history on a fine mesh calculation. Solid: total energy; dash: kinetic energy; dots: potential energy; dash-dot: initial total energy - cumulative energy dissipation due to turbulence.

To further study the effect of numerical dissipation, a large eddy simulation (Smagorinsky $Cs = 0.15$) was performed on the refined mesh as described in section 5.1.5. Figure 5.10 shows that the kinetic energy gained the loss of potential energy is almost dissipated by the turbulent diffusion before the wave breaks. But as the wave begins to rapidly decay, the turbulent dissipation cannot account for all the energy loss, which implies that a large amount of numerical dissipation happens.

5.2 Plunging Breaker on a Relatively Steep Slope

5.2.1 Laboratory and Numerical Setup

The experiments were conducted in a wave tank at Hydrodynamic Laboratory, University of Oslo. The wave tank is 1m high and 0.5m wide with a sloping beach at one end. The coordinate system is chosen so that $x = 0$ is at the still shoreline and $z = 0$ is at the still water level while the still water depth is $h_0 = 0.205$m. A sloping beach with an inclination $\theta = 5.1°$ is located at a distance of 5.177m from the initial position of wave maker. The sketch of wave tank can be seen in Figure 5.19 except that the cylinder is not present in the experiments. The incident solitary wave is either $H_0/h_0 = 0.33$ or $H_0/h_0 = 0.25$, which are both plunging waves according to equation (5.4):

$$S_0 = \begin{cases} 0.271, & \text{for } H_0/h_0 = 0.25 \\ 0.236, & \text{for } H_0/h_0 = 0.33 \end{cases} \tag{5.12}$$

A resistance-type wave gauge was installed at $x = 4.485$m off the shore to measure the incident solitary wave. PIV was employed with two fields of view (FOVs) near the shoreline region. It is noted that the real still water depth is $h_0 = 0.21$m so that the still water level is at $z = 0.005$m.

In the following section, the $H_0/h_0 = 0.33$ solitary wave case will be presented. The numerical domain is 7.25m long, 0.05m wide and 0.305m high. The toe of sloping beach is located at $x = 3.0$m. The wave is generated by specifying the velocity and surface elevation at the incident boundary $x = 0$ as described in Chapter 3, and approaches perpendicularly to the beach. The upper boundary is pressure Dirichlet boundary $p = 0$, the bottom of the wave tank is no-slip wall

boundary, and the two lateral boundaries are free-slip wall boundaries. The length of the computational domain is long enough so that the run-up tip will not reach its end, thus the boundary at the domain end is a solid wall.

Unstructured mesh is used to discretize the computational domain with smallest volumes at the top and bottom of the numerical wave tank. The grids are uniform in streamwise and spanwise directions, $\Delta x = \Delta y = 6.25$mm, and nonuniform in vertical direction, $\Delta z_{min} = 4$mm and $\Delta z_{max} = 4.5$mm.

5.2.2 Wave Profile and Velocity Field

Figure 5.11 shows the free surface elevation of a plane solitary wave $H/h = 0.33$ at the wave gauge position ($x = 4.485$m in laboratory frame). The numerical solitary wave matches very well with the laboratory wave profile. We then synchronize the numerical and laboratory measurements by the time when the solitary wave crest pass through the wave gauge. In the numerical simulation, the solitary wave crest passes through the gauge at $t_n = 2.06$ second, while the laboratory wave passes at $t_l = 3.2$ second.

Figure 5.12– 5.14 present the wave profile at the symmetric plane of the wave tank and the velocity field at the first PIV field of view (FOV1). In general, the numerical simulations compare well with the laboratory measurements in terms of the free surface profile and velocities. The solitary wave is in its shoaling process, and the numerical wave phase matches quite well with the laboratory one. As shown in Figure 5.15, the local wave height does not change very much as the wave goes up the beach, which agrees with Grilli's observation[22, 23] that wave height does not change much on a relatively steep slope (1 : 8 in Grilli's

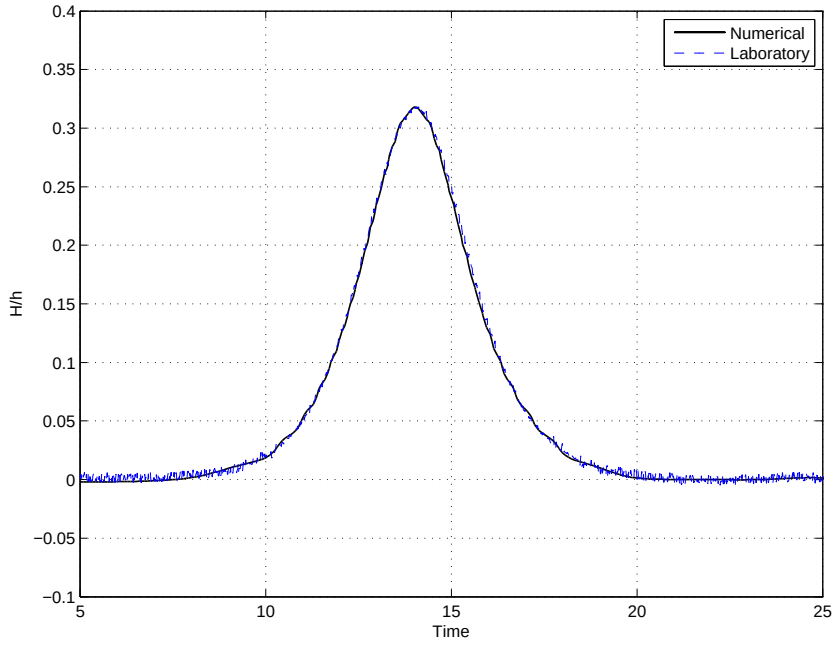

Figure 5.11: History of free surface elevation at the wave gauge position. The elevation is normalized by still water depth h_0, and time is scaled by $\sqrt{h_0/g}$. Solid: numerical; dash: laboratory.

papers). The wave front eventually becomes vertical as it approaches the breaking point. Here we define the breaking point as where the wave front is vertical, and it is $x = 5.11$m in computational domain or $x = 187$mm in laboratory coordinate system. The breaking index H_b/h_b is listed in Table 5.3 and compared with the predicted value of other researchers. Our numerical value is between Grilli's and Camfield's empirical results, but it is closer to Grilli's value, because Camfield's empirical formula considers very mild slopes while Grilli's incorporates data of relatively steep slopes.

Table 5.3: Breaking index

	Our result	Camfield and Street [5]	Grilli et al [23]
H_b/h_b	3.23	2.09	3.82

It should be noted that in 5.12– 5.14, there exist a few velocity vectors outside the free surface in both laboratory and numerical data. However, they are caused by different reasons. In the numerical simulation, the free surface is defined by the VOF function, and is not a sharp interface. It smears over one or two cells instead. The free surface presented in the figures is the contour line of VOF function constant $f = 0.5$, thus velocity may exist where VOF function is not zero value outside the contour line $f = 0.5$. In the laboratory measurements, the velocity outside the free surface is not physical, and it may be caused by the background noises and reflections.

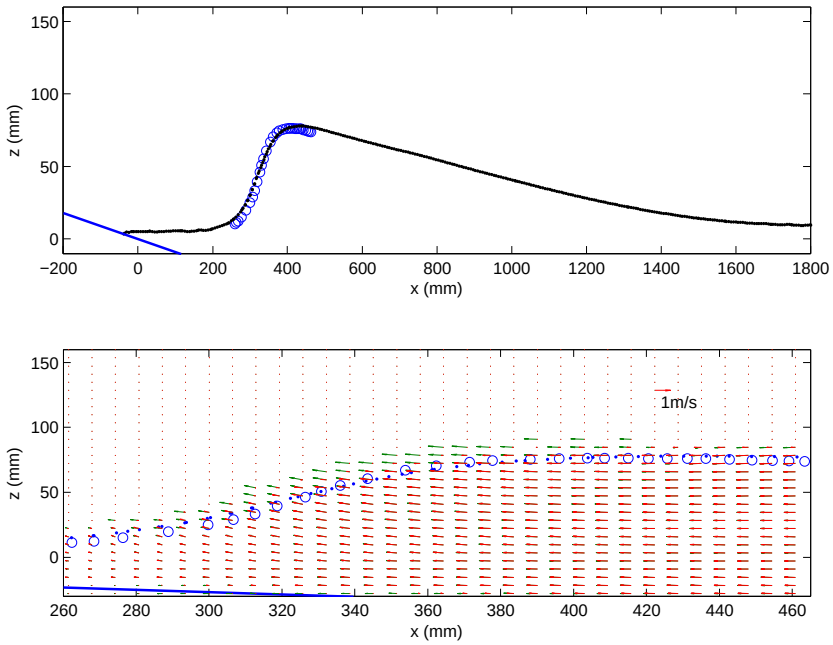

Figure 5.12: Comparisons of numerical and laboratory wave profile and velocity field (FOV1) at $t\sqrt{g/h_0} = 31.35$. Circle: laboratory data; dots (line): numerical result. Red arrow: numerical velocity; green arrow: laboratory velocity. Top: wave profile; bottom: flow field on FOV1.

Figure 5.16 and 5.17 show the wave profiles at the symmetric plane and the velocity fields at the second PIV field of view (FOV2). The back of the wave

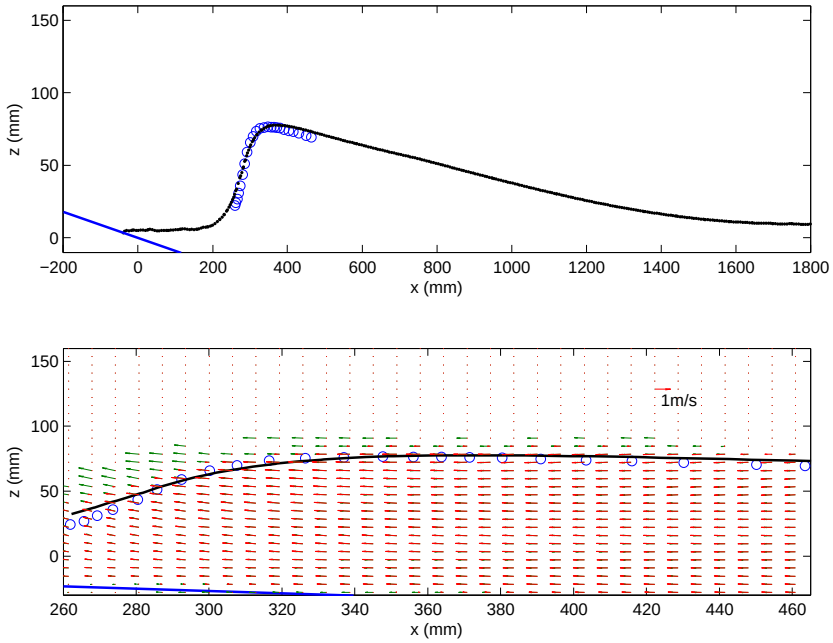

Figure 5.13: Comparisons of numerical and laboratory wave profile and velocity field (FOV1) at $t\sqrt{g/h_0} = 31.63$. Circle: laboratory data; dots (line): numerical result. Red arrow: numerical velocity; green arrow: laboratory velocity. Top: wave profile; bottom: flow field on FOV1.

profile shows excellent agreement, so are the velocity field. But the numerical wave front moves slower than the laboratory wave front. In Figure 5.16, the laboratory wave front steepens and becomes almost vertical, which indicates that the wave is about to break, while the numerical wave is still shoaling. Thus the particle velocity at the numerical wave front is also smaller than the laboratory velocity. In Figure 5.17, the laboratory solitary wave begins to overturn its front. The numerical wave is also overturning but at a smaller degree. The lower part of laboratory wave front indicates that the toe of wave front is beyond the still water shoreline, but it is obviously not true, and the explanation is that the mask technique used to extract the free surface location in the experiments works poorly at the lower part of overturning curve.

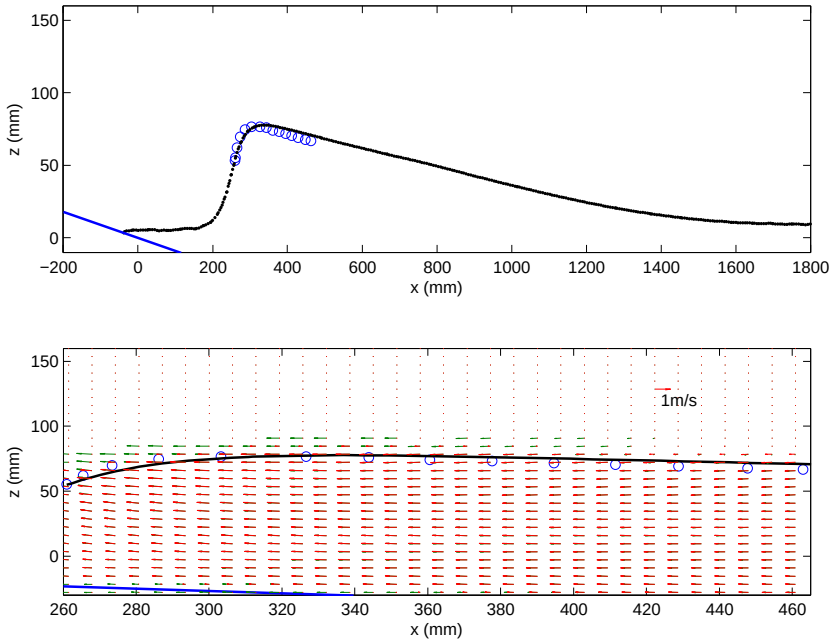

Figure 5.14: Comparisons of numerical and laboratory wave profile and velocity field (FOV1) at $t\sqrt{g/h_0} = 31.77$. Circle: laboratory data; dots (line): numerical result. Red arrow: numerical velocity; green arrow: laboratory velocity. Top: wave profile; bottom: flow field on FOV1.

Although the numerical wave shows a phase difference to the laboratory wave in the overturning stage, the numerical solitary wave evolves in a similar manner to that of laboratory wave. In Figure 5.18, the numerical solitary wave profiles at different time instants are plotted at an interval $\Delta t = 0.01$s, demonstrating the evolution of solitary wave from shoaling to overturning. The laboratory wave profiles are shifted horizontally towards the shoreline by 70mm, represented as square signs in the figure. It is seen that the shifted laboratory wave shapes matches quite well with the numerical wave profiles at some instants.

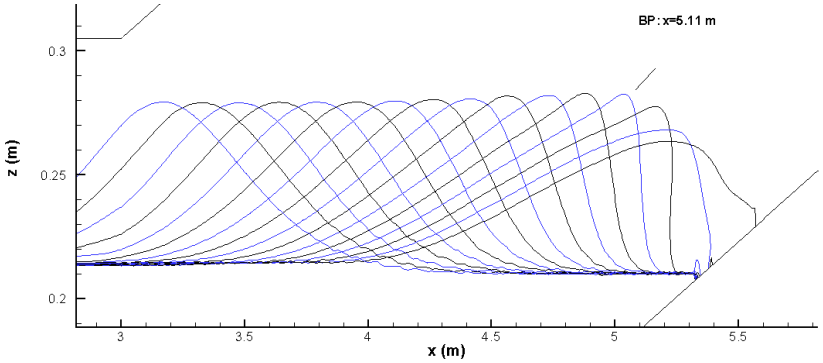

Figure 5.15: Envelop of water surface in the numerical simulation. $x = 0$ is at the incident boundary of computational domain.

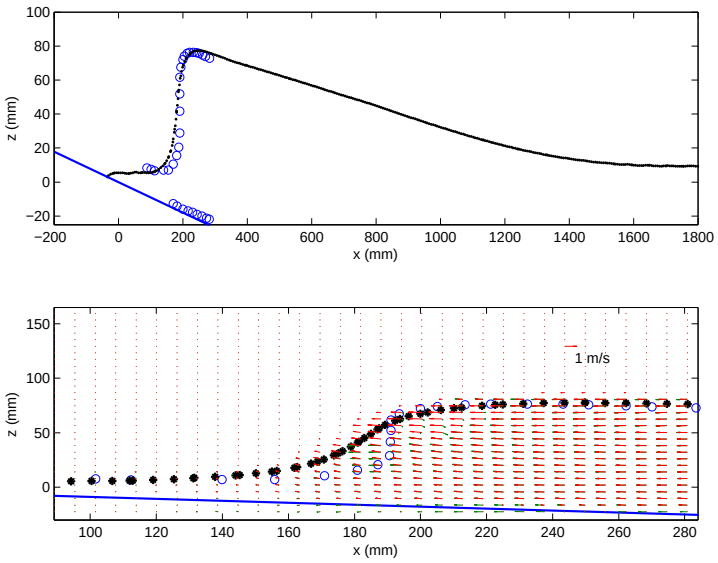

Figure 5.16: Comparisons of numerical and laboratory wave profile and velocity field (FOV2) at $t\sqrt{g/h_0} = 32.18$. Circle: laboratory data; dots (line): numerical result. Red arrow: numerical velocity; green arrow: laboratory velocity. Top: wave profile; bottom: flow field on FOV2.

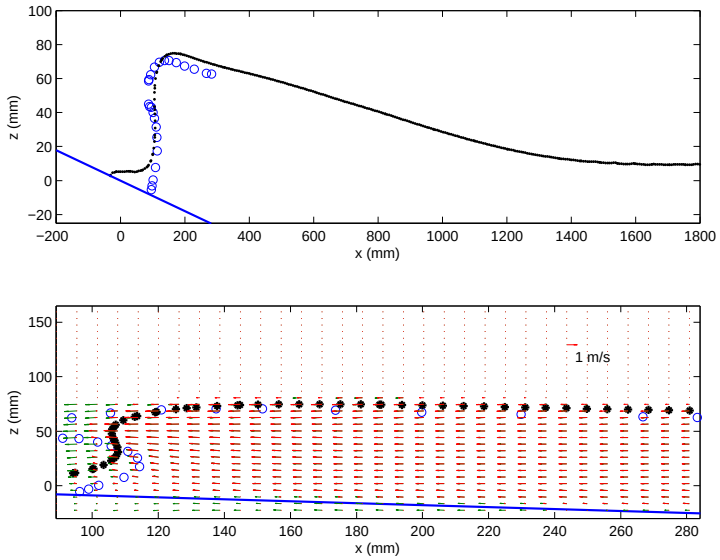

Figure 5.17: Comparisons of numerical and laboratory wave profile and velocity field (FOV2) at $t\sqrt{g/h_0} = 32.59$. Circle: laboratory data; dots (line): numerical result. Red arrow: numerical velocity; green arrow: laboratory velocity. Top: wave profile; bottom: flow field on FOV2.

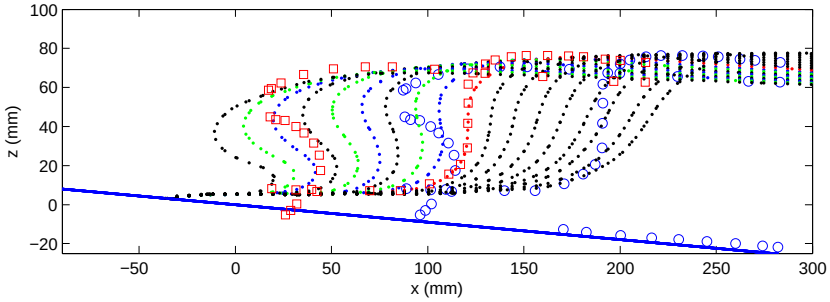

Figure 5.18: Comparison of overturing wave front. Dots: numerical wave profiles at different time instants, and time interval between each curve is $\Delta t = 0.01$s. Circle: laboratory wave profiles. Square: shifted laboratory wave profiles.

5.3 Breaking Solitary Wave Impact on a Cylinder at the Slope

5.3.1 Laboratory and Numerical Setup

The experiment setup is similar to that of the pure breaking wave case. As shown in Figure 5.19, the coordinate system is chosen so that $x = 0$ is at the still shoreline and $z = 0$ is at the still water level while the still water depth is $h_0 = 0.205$m. A sloping beach with an inclination $\theta = 5.1°$ is located at a distance of 5.177m from the initial position of wave maker. And a steel circular cylinder of a diameter of 60mm is rigidly fixed on the beach with its axis at $x = 260$mm.

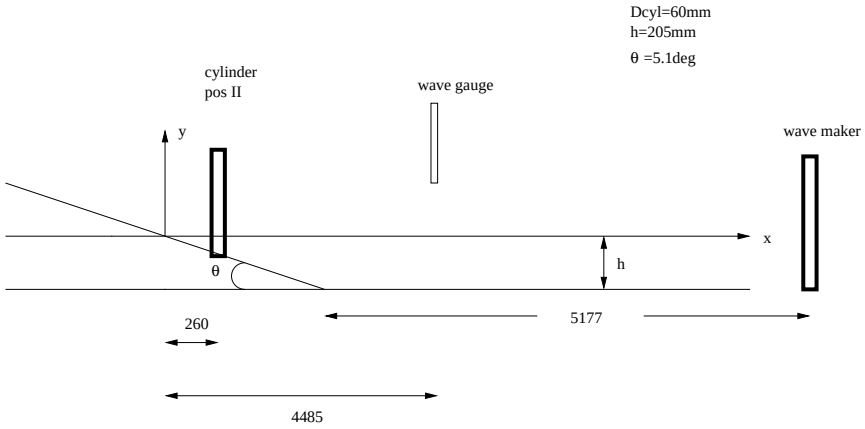

Figure 5.19: Sketch of experiment setup

The $H_0/h_0 = 0.33$ solitary wave case will be discussed here. The simulation is a half domain calculation due to the symmetry of the problem. The numerical domain is 7.25m long, 0.25m wide and 0.44m high. The toe of beach is at $x = 3.0$m. The wave is generated by specifying the velocity and surface elevation at the incident boundary $x = 0$ as described in Chapter 3, and approaches perpendicularly to the beach and impinges on the cylinder. The upper boundary is pressure Dirichlet boundary $p = 0$, the bottom of the wave tank and the cylinder

face are no-slip wall boundaries, and the two lateral boundaries are free-slip wall boundaries. The length of the computational domain is long enough so that the run-up tip will not reach its end, thus the boundary at the domain end is a solid wall.

Irregular unstructured mesh is used to discretize the computational domain. The grids are finer near the cylinder, the sea bed and the top boundary. In the vertical direction, the smallest grid size is Δz_{min} = 4.5mm and the coarsest one is Δz_{max} = 6.7mm. The cylinder perimeter is discretized by a 22-edge polygon, which gives a grid size of Δ = 8.6mm along the perimeter. And the horizontal grid size gradually increases from Δx = 8.6mm to Δx = 12.6mm in the cylinder neighborhood region. The horizontal and span-wise grid size outside the cylinder neighborhood region is uniform with $\Delta x = \Delta y$ = 12.6mm.

5.3.2 Wave Profile and Velocity Field

Figure 5.20– 5.25 show the numerical and laboratory wave profile and flow field in front of the cylinder (offshore side). The numerical free surface agrees very well with the laboratory data as the wave approaches the cylinder and then runs up the cylinder face. In Figure 5.25, the numerical wave shows an obvious reflection from the cylinder while the reflected wave is not seen in laboratory data. However, the raw PIV image at this moment shows a reflected wave as seen in Figure 5.26, thus the 'missing' wave hump in the laboratory data may be attributed to poor quality of the raw image on the reflected wave part.

The numerical velocity fields also demonstrate excellent agreements in general. Due to the blockage of the cylinder, the velocities near the the cylinder

front face are very small except those near the free surface, therefore the water is pushed upwards and sideways, demonstrating a complex three dimensional flow phenomena.

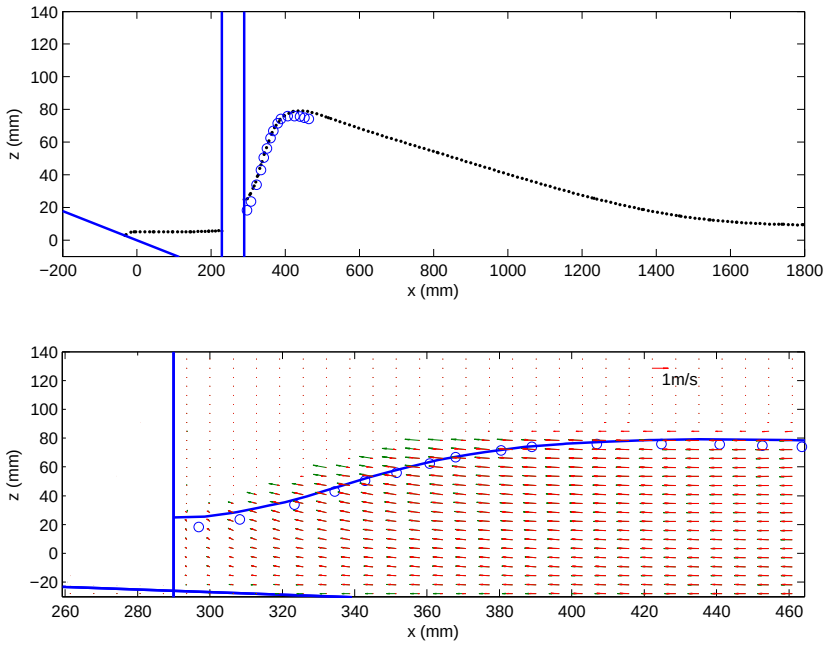

Figure 5.20: Comparisons of numerical and laboratory wave profile and velocity field (FOV1) at $t\sqrt{g/h_0} = 31.70$. Circle: laboratory data; dots (line): numerical results. Red arrow: numerical velocity; green arrow: laboratory velocity. Top: wave shape; bottom: flow field on FOV1.

Figure 5.27 shows the free surface profile during the impact period. Figure 5.27(a) is at $t\sqrt{g/h_0} = 32.1$, and the following sub-figures are at the time interval $\Delta t = 0.02$s. The flow shows a strong three dimensional effect. As the wave front passes through the cylinder, two water sleeves are generated at the cylinder sides, as shown in Figure 5.27(c)–(f). The sleeves move quickly forward and their tips break apart into water droplets. And they then collide with each other at the back of the cylinder (Figure 5.27(f)). Later, the wave front separated by

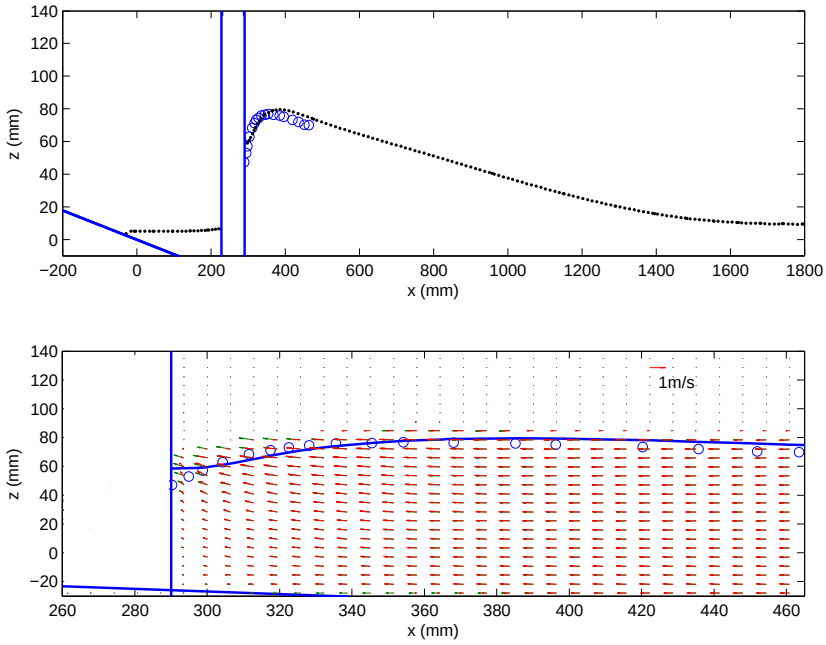

Figure 5.21: Comparisons of numerical and laboratory wave profile and velocity field (FOV1) at $t\sqrt{g/h_0} = 31.97$. Circle: laboratory data; dots (line): numerical results. Red arrow: numerical velocity; green arrow: laboratory velocity. Top: wave shape; bottom: flow field on FOV1.

the cylinder connects itself and collapse onto the water bed, entrapping some air inside(Figure 5.27(h)). The run-down at the cylinder front generates secondary sleeves wrapping around the cylinder.

Compared with the impact on a cylinder on the flat seabed, the flow around the cylinder is more violent. The sleeves around the cylinder and the air entrapment are not present when the solitary wave impinges a cylinder on the flat seabed. And it should be expected that the force history would show quite a difference, which is to be discussed later.

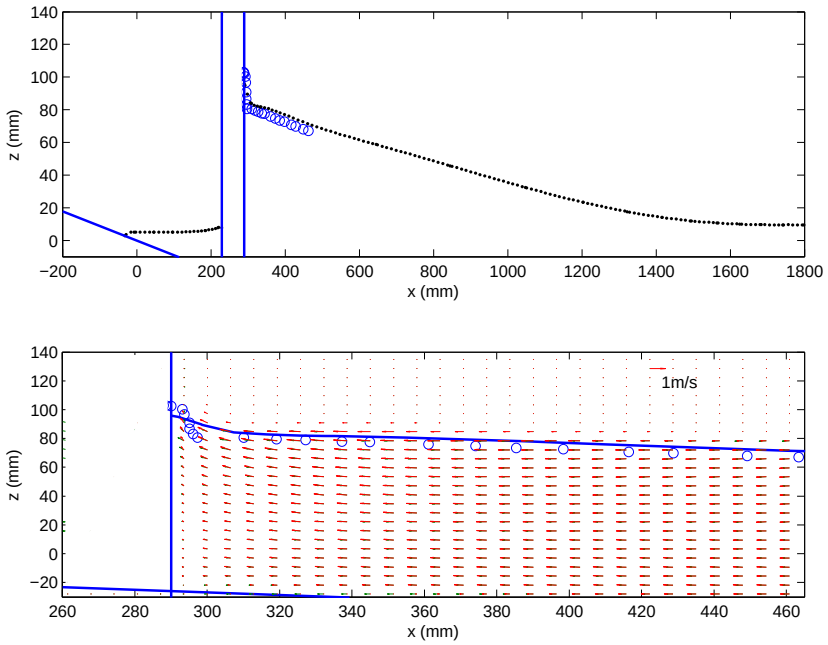

Figure 5.22: Comparisons of numerical and laboratory wave profile and velocity field (FOV1) at $t\sqrt{g/h_0} = 32.18$. Circle: laboratory data; dots (line): numerical results. Red arrow: numerical velocity; green arrow: laboratory velocity. Top: wave shape; bottom: flow field on FOV1.

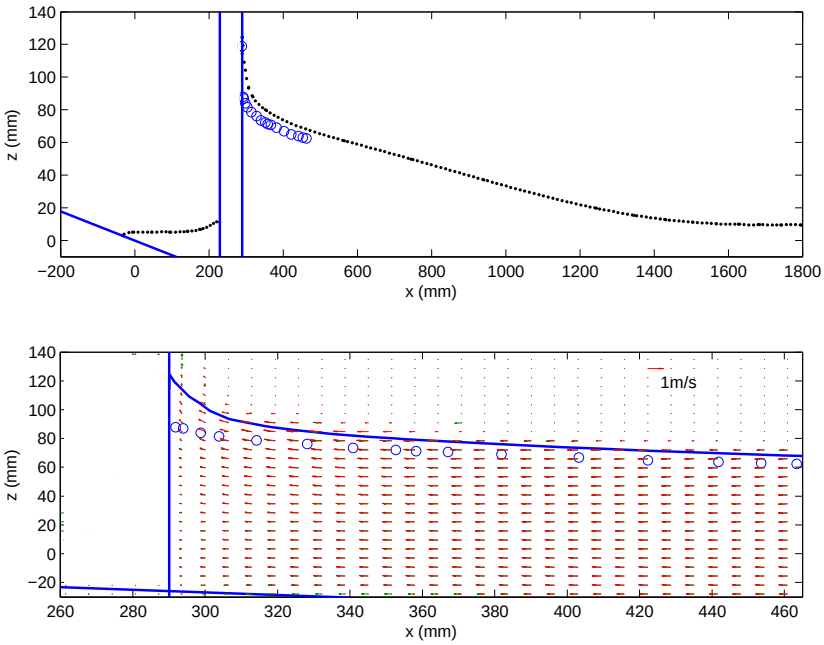

Figure 5.23: Comparisons of numerical and laboratory wave profile and velocity field (FOV1) at $t\sqrt{g/h_0} = 32.38$. Circle: laboratory data; dots (line): numerical results. Red arrow: numerical velocity; green arrow: laboratory velocity. Top: wave shape; bottom: flow field on FOV1.

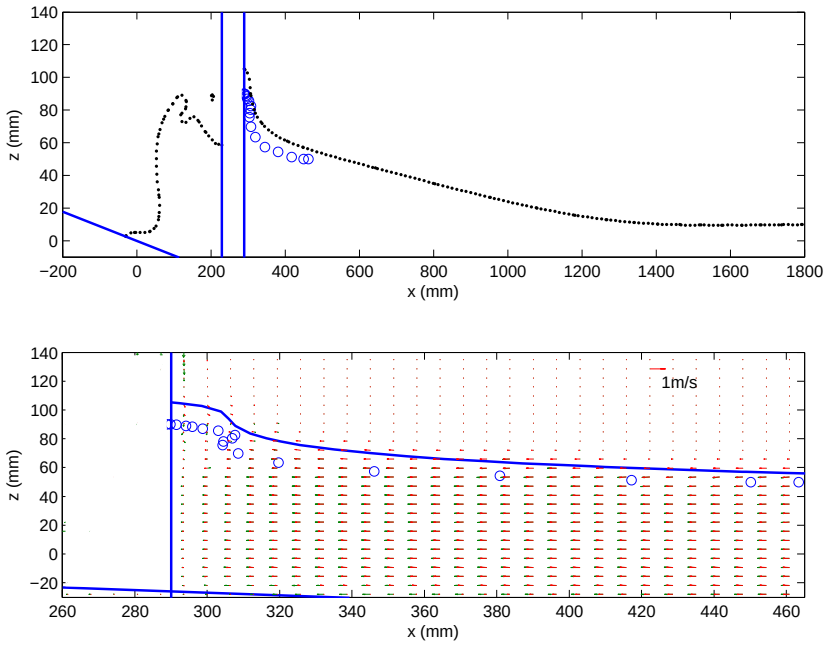

Figure 5.24: Comparisons of numerical and laboratory wave profile and velocity field (FOV1) at $t\sqrt{g/h_0} = 33.47$. Circle: laboratory wave profile; dots or solid line: numerical wave profile. Red arrows are numerical velocity vectors, green ones are the laboratory velocity measurements. The upper shows the wave profile, and the lower shows the flow field in the PIV field of view (FOV1).

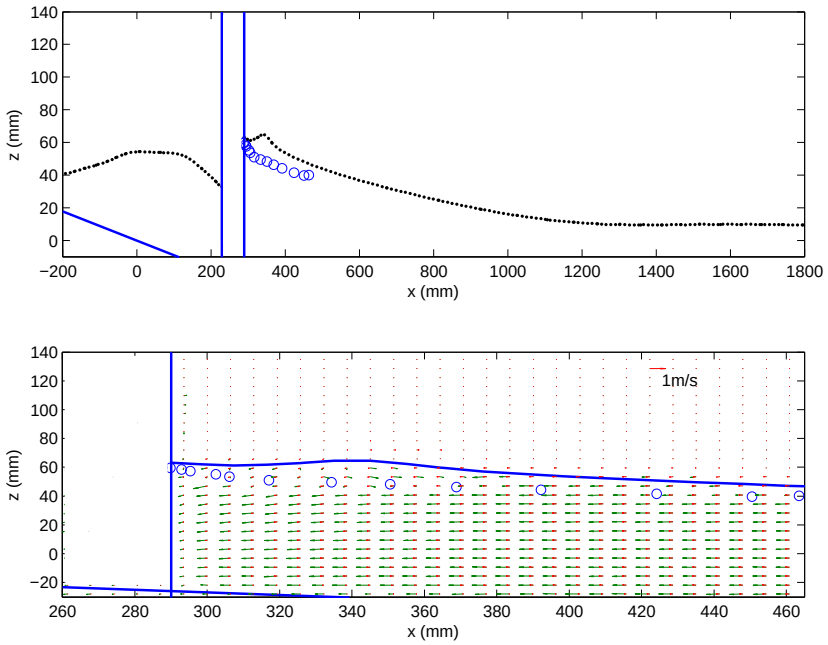

Figure 5.25: Comparisons of numerical and laboratory wave profile and velocity field (FOV1) at $t\sqrt{g/h_0} = 34.91$. Circle: laboratory data; dots (line): numerical results. Red arrow: numerical velocity; green arrow: laboratory velocity. Top: wave shape; bottom: flow field on FOV1.

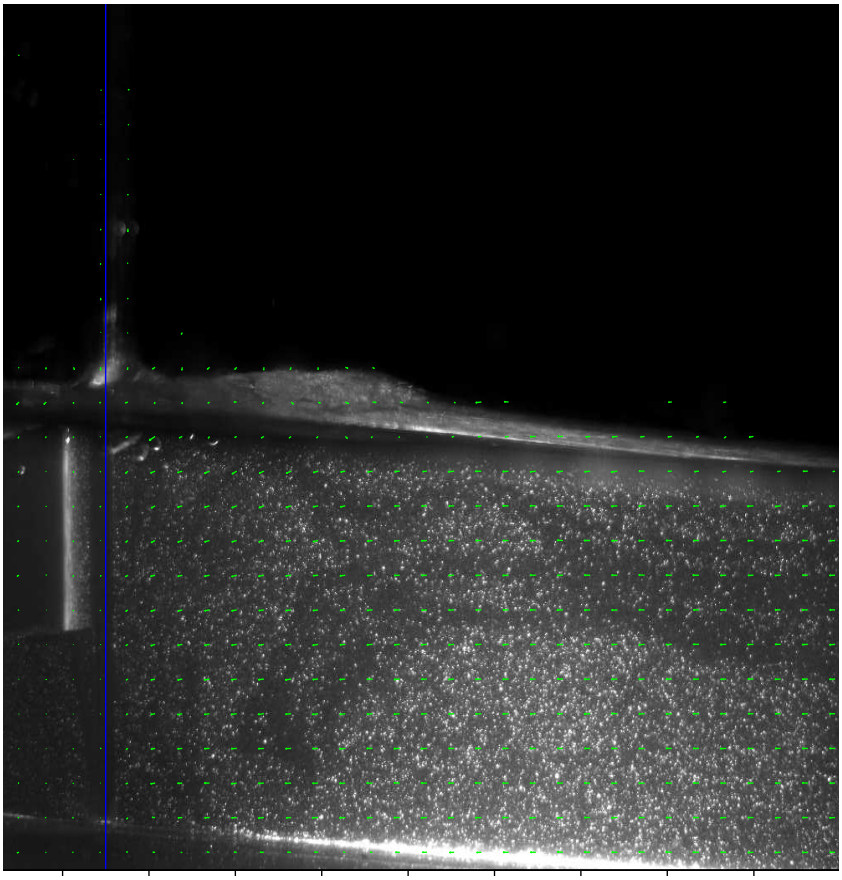

Figure 5.26: Raw PIV image at $t\sqrt{g/h_0} = 34.91$.

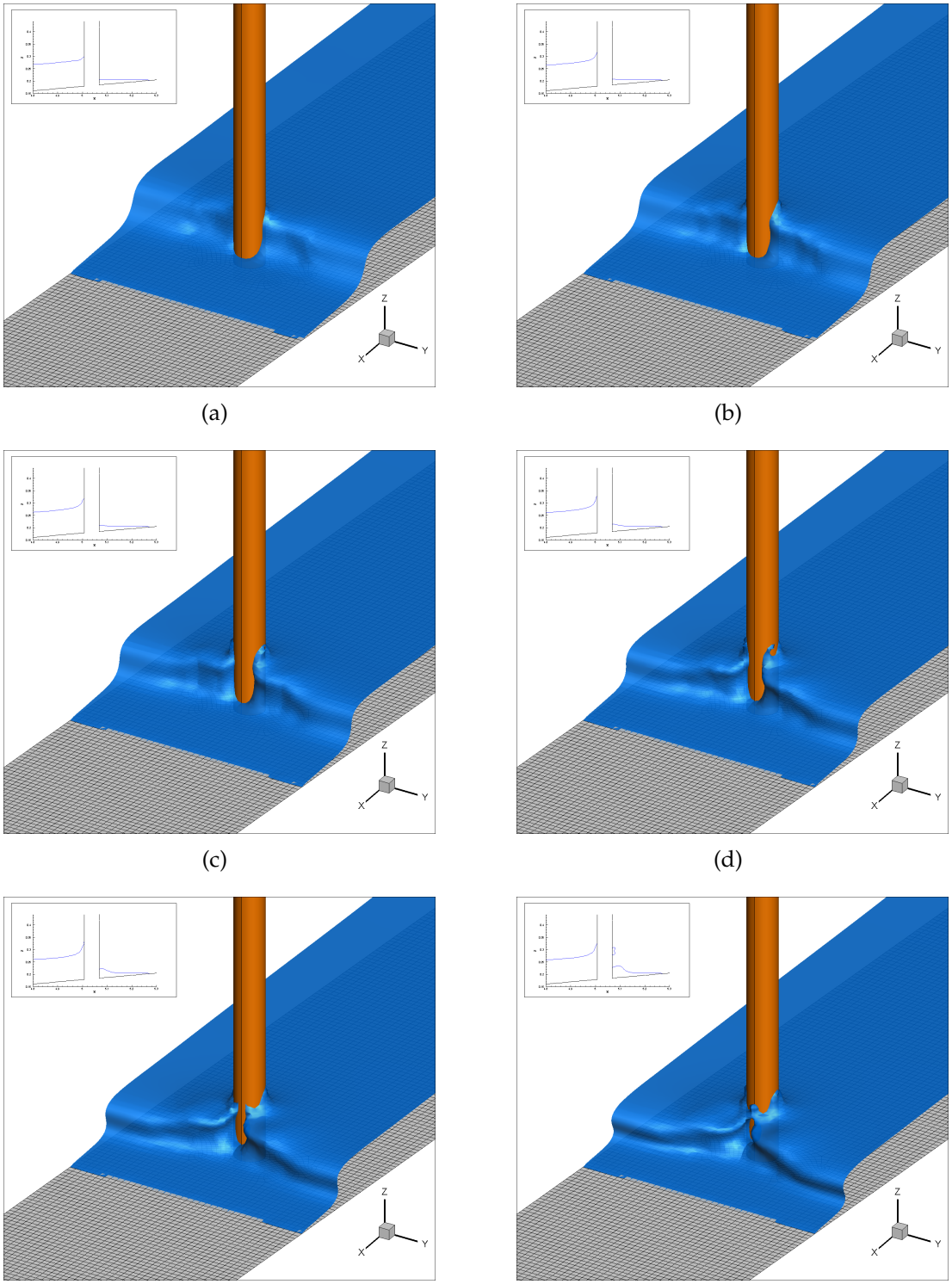

(a) (b) (c) (d) (e) (f)

Figure 5.27: Snapshots of solitary wave impinging a cylinder.

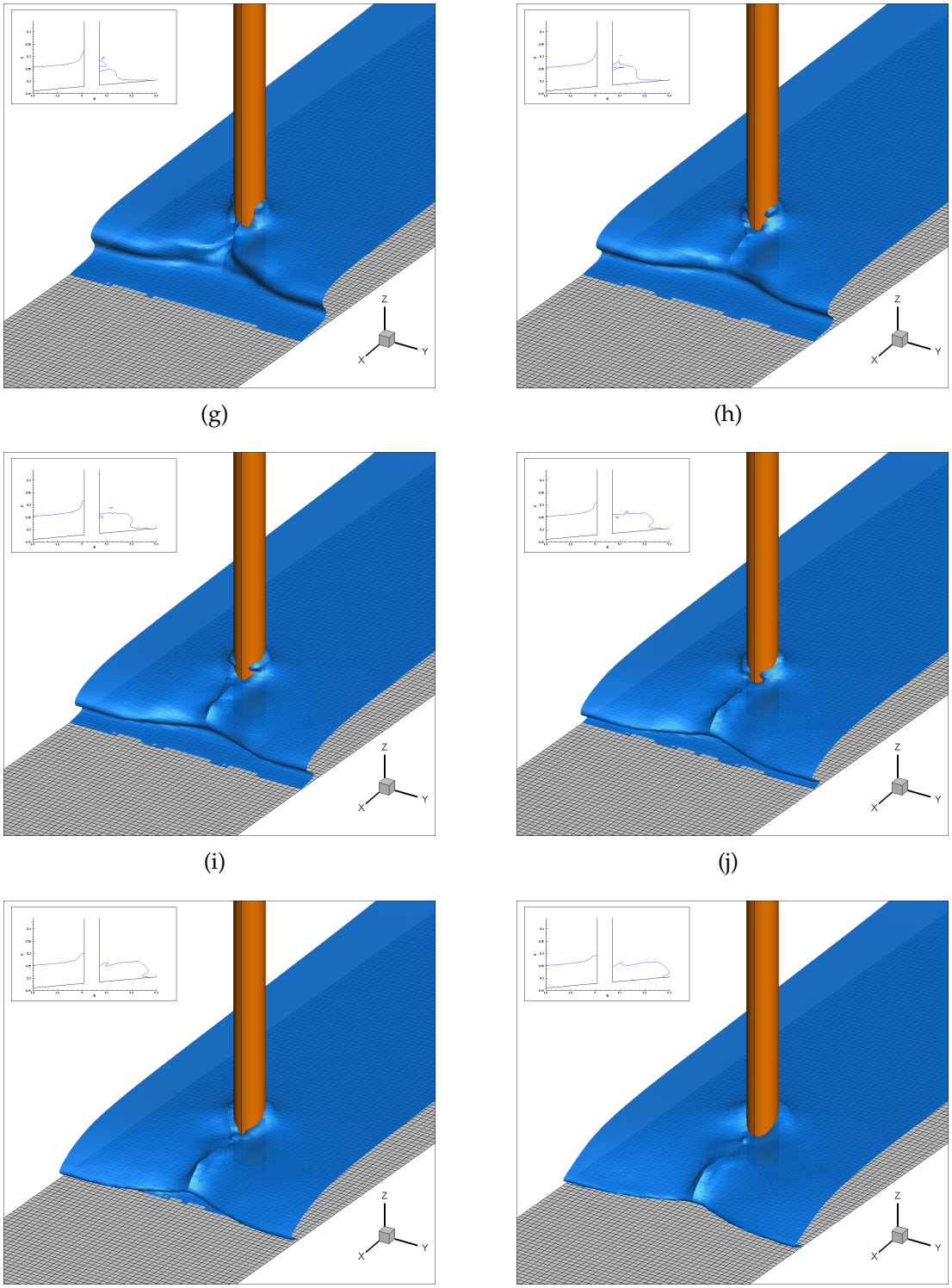

(g) (h)

(i) (j)

(k) (l)

Figure 5.27: Snapshots of solitary wave impinging a cylinder (cont).

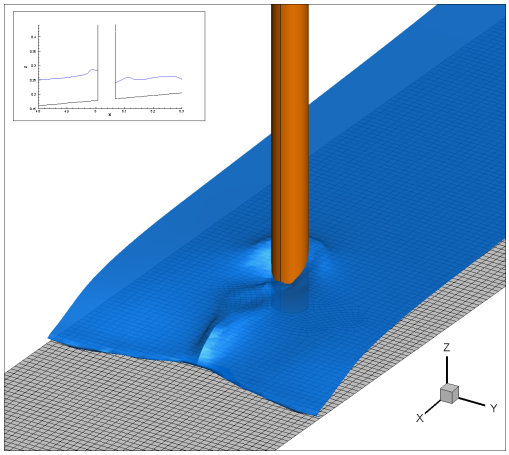

(m)

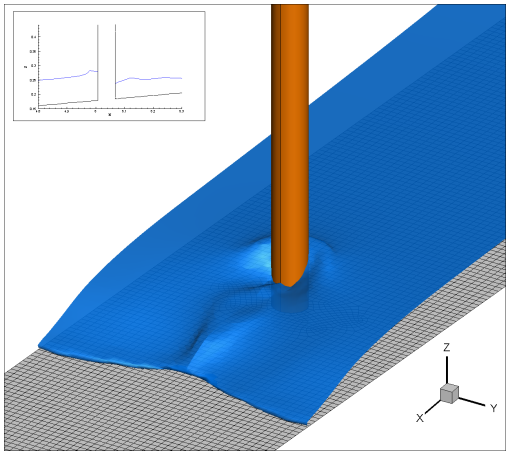

(n)

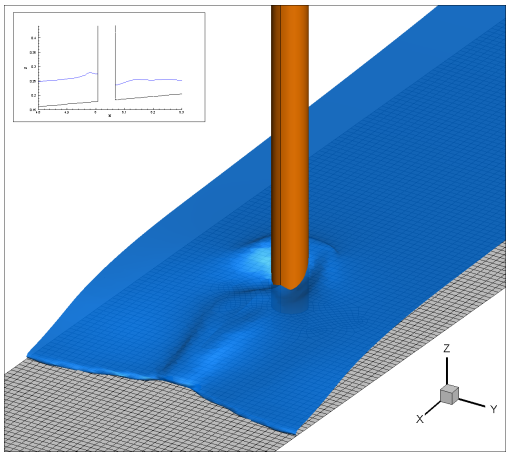

(o)

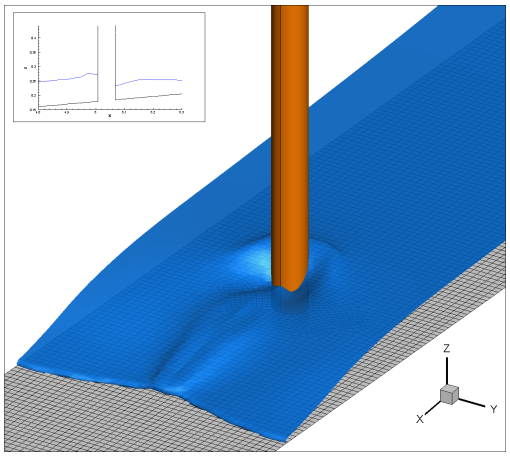

(p)

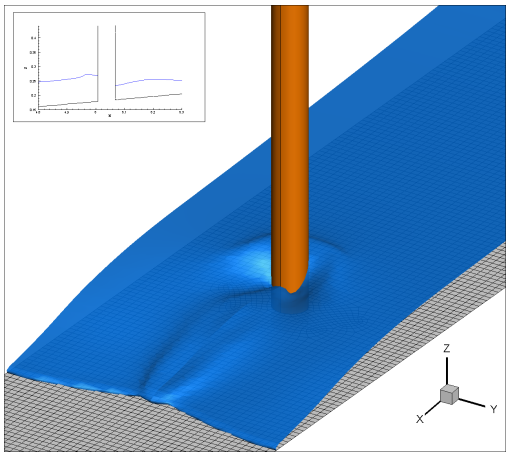

(q)

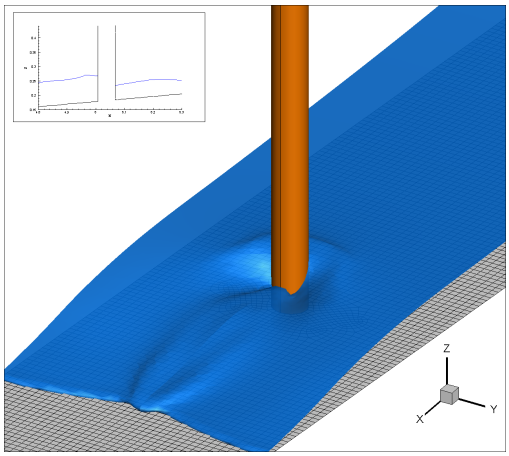

(r)

Figure 5.27: Snapshots of solitary wave impinging a cylinder (cont).

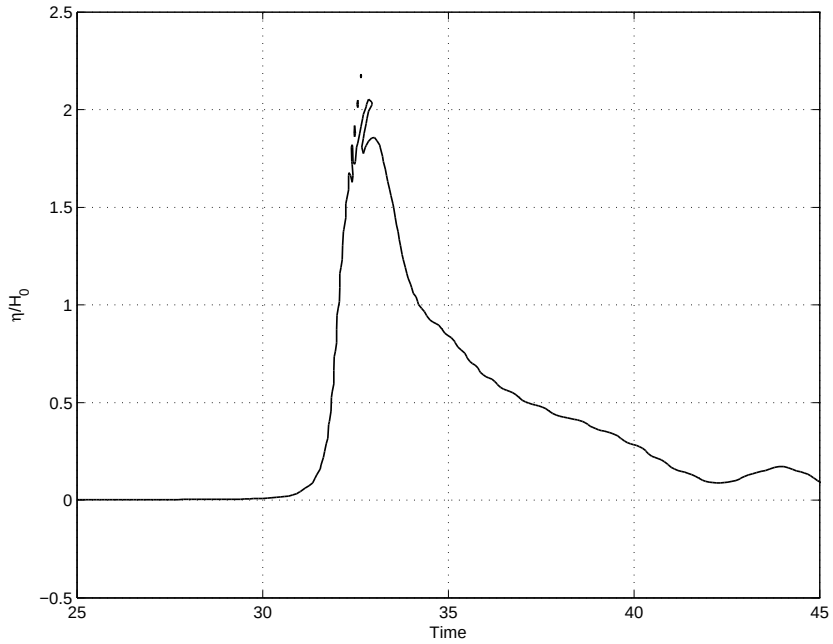

Figure 5.28: Run-up at the front of the cylinder (offshore side).

5.3.3 Wave Force and Run-up

The run-up at the front of the cylinder (offshore side) is shown in Figure 5.28. After $t' = 32.41$, the water surface at the cylinder face shows some discontinuity, i.e. there exists some water droplets at the cylinder face, which should be because the run-up tongue is so thin that the grid resolution there is not fine enough to resolve it. Therefore, we choose the maximum wave height at $t' = 32.41$ as the run-up of solitary wave, and it gives $R_u/H_0 = 1.81$. The run-up tongue does not drop immediately after reaching its highest position, instead it remains there for some time due to the local wave steepening effect.

The history of wave load is shown in Figure 5.29. The dimensionless maximum force is obviously higher than that on the cylinder on a flat seabed. It occurs at $t' = 32.26$ which is before the run-up reaches the highest. And it corresponds to the free surface profile in Figure 5.27(b). As the water wraps around

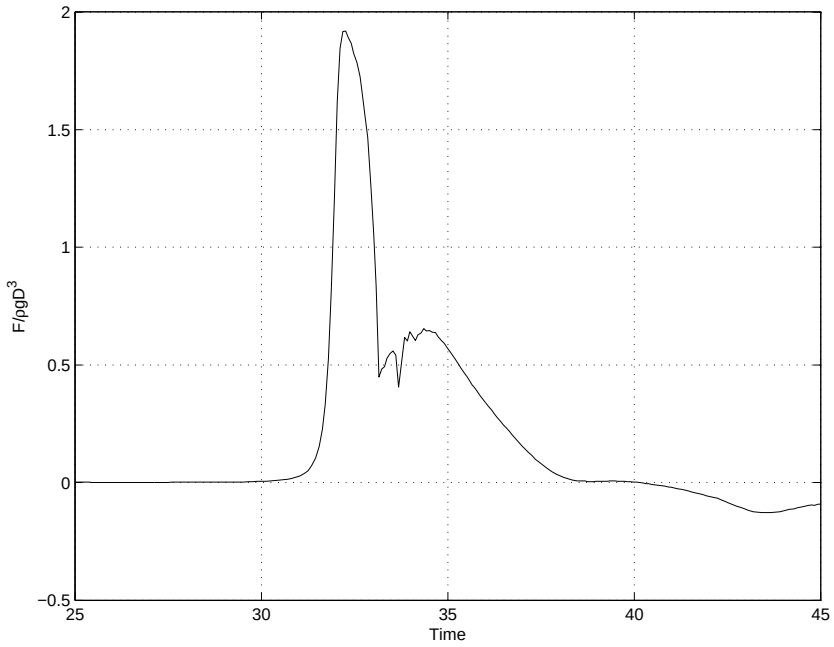

Figure 5.29: Horizontal force history on the cylinder.

the back of the cylinder, the force decreases. But the force history does not present a clear trough as seen in the flat seabed case. At $t' = 33.23$, the separated wave fronts finish their merging and move forward along the beach as a smooth front line, and it drains water out of the back region of the cylinder so that water level decreases there (see Figure 5.27(i)). As a result, the force starts to increase again. But as the secondary sleeves merges (Figure 5.27(k)), the force shows a secondary drop. Then the force increases again.

The maximum wave force and run-up are compared with those of the flatbed case as shown in Table 5.4. The values of the flatbed case are calculated from the fitting formula obtained in Chapter 4 (Table 4.2 and 4.4). It is clear that the maximum wave force and run-up are noticeably larger than those of flatbed case, which indicates that breaking waves may cause more severe design wave

Table 5.4: Comparison of maximum wave force and run-up of flatbed and beach cases.

	Flatbed case	Beach case
$F_m/\rho g D^3$	1.2644	1.918
R_u/D	1.5356	2.04

condition to the coastal structures.

$$\frac{F_m}{\rho g D^3} = 0.1166\left(\frac{h}{D}\right)^{1.94} \tag{5.13}$$

$$\frac{Ru}{D} = 0.4707\left(\frac{h}{D}\right)^{0.9624} \tag{5.14}$$

5.4 Concluding Remarks

In this chapter, the spilling and plunging solitary waves on a sloping beach are studied. Numerical results are compared with the experimental data. We conclude that the numerical code can satisfactory simulate the breaking wave phenomena.

The impact by a plunging solitary wave on a vertical cylinder is studied. Numerical results are compared with the experimental data and show very good agreement. The impact process is quite different from that on the flat bottom. Furthermore, the magnitude of wave load, as well as the maximum run-up, is larger than that on the cylinder on a flat bottom.

CHAPTER 6

CONCLUSIONS AND FUTURE WORK

6.1 Conclusions

In this study, a numerical model is developed to solve the three dimensional wave-structure interaction problem. It is based on the full Navier-Stokes equations or Euler's equation for incompressible flow, thus it is not limited to the irrotational flow as the integral equation methods [81, 45, 25] are. A irregular mesh is employed to partition the computational domain, thus very complex geometries, which are difficult to handle in coordinate transformation method[37] and in Cartesian mesh, can be treated with high accuracy and the application of solid wall boundary condition is easier. Therefore, the current numerical model is more preferable to others.

In our numerical model, the N-S equations are numerically solved by a two-step projection finite volume scheme and the free surface movement is tracked by the piecewise linear volume of fluid (VOF) method. Compared with the original numerical model, the large eddy sub-grid model, either the classical Smagorinsky model or RNG sub-grid model, is used to model the turbulence. And various types of waves, such as high nonlinear solitary wave and Stokes waves, can be successfully generated and propagate into and out of the computational domain.

The model's performance in simulating the wave flow has been evaluated by using non-breaking waves. For a non-breaking solitary wave propagating in a constant water depth, the numerical solution is compared with the analytical

theory. The conservative property of the numerical model is also inspected. For a periodic Stokes wave, the numerical solution is compared with the laboratory measurements. We found that the numerical model gives satisfactory results for the wave kinematics, such as the free surface displacement, phase speed and fluid velocity. Therefore, the numerical model is accurate in simulating non-linear waves.

The numerical model is then used to simulate solitary waves and their interaction with a group of slender vertical piles in a constant water depth. For the tested cases, waves are non-breaking and turbulence is negligible, thus the Euler's equation is numerically solved. The model is validated by comparing numerical results with laboratory data in terms of free surface displacements, fluid particle velocity and wave forces. The relatively less satisfactory agreement is observed in the dynamic pressure on the cylinder, but this could be due to the measurement errors.

We also performed an extensive parameter study for the wave force and run-up on a single cylinder, which is not very often feasible in laboratory experiments and has not been studied by other numerical studies. The relation between the wave force (run-up) and the wave steepness H/h and depth-diameter ratio h/D is given. However, the parameter range is still limited (h/D is up to 10 only) due to the constraint of the computational resources. In addition, the observation is confined to very high Reynolds number. Besides the interaction between wave and single cylinder, numerical simulations of interaction between wave and a group of cylinders are performed and the effect of multiple cylinders are discussed.

Some important characteristics of the wave-structure interaction are summa-

rized below:

- Flows are three dimensional, transient and rotational. Local turbulence may occur in the vicinity of the cylinder and in the scattered wave.
- For the single cylinder case, the total wave force and run-up at the front side of the cylinder can be expressed as a power function of H/h or h/D, and they are essentially non-linear even when the non-linearity of incident solitary wave is small.
- The existence of the cylinders lags the incident wave phase and generates scattered waves. However, it does not disturb the wave very much, and the solitary wave reverts back to its original shape after its crest passes the cylinder over a distance of about 4 times the cylinder radius.
- Two scattered waves are generated in the wave-structure interaction process. One is due to the reflection from the front side of cylinder, and the other is generated by the water column trapped behind the cylinder and propagates along the cylinder circumference and to the sides. This feature is observed in both single cylinder and multiple cylinder cases.
- For the single cylinder case, the adverse dynamic pressure gradient appears at the back side of the cylinder because of the local free surface difference there which is caused by the free surface detachment.
- For the single cylinder case, a vortex is first generated at the lee side of the cylinder and evolves eventually to the bottom. A second vortex is triggered by the secondary scattered wave at the location behind the middle of the cylinder.
- Similar physics for pressure and velocity field is also observed for the instrumented cylinder in multiple cylinder case, but the flow inside the

cylinder grid is more complex.

- In the multiple cylinder case, the impact wave shape is locally deformed because of the scattering by the front two dummy cylinders, and its leading wave has a smaller wave height and a shorter wave length than those of single cylinder case.
- The total wave force is smaller in the multiple cylinder case than that of single cylinder case because of the wave scattering by the front dummy cylinders. Significant phase difference also appears in the force time history because of the interference effect.

The numerical model is also used to study the breaking solitary waves on a slanted beach. Both spilling and plunging breaker solitary waves are studied, which are the most common breaking waves in coastal region. The spilling breaker occurs on very mild slope with its breaking process confined within a small region near the wave front. The plunging breaker, on the other hand, occurs on relatively steeper slope and is more violent.

For the spilling breaker solitary wave, two LES sub-grid models are used and their performance is studied. The numerical solutions are compared with the laboratory measurements. It shows that both sub-grid LES models can model the shoaling process and the breaking process in the surf zone. Although the RNG sub-grid model behaves like the traditional LES model ($Cs = 0.15$), it gives better results during the shoaling process and describes better the transition from laminar to turbulent flow than the traditional LES model does. The numerical results also show that the LES model is not very sensitive to the choice of Cs value as long as the turbulence effect is triggered.

For the plunging breaker solitary wave, the RNG sub-grid model is used for

the turbulence field. The free surface profiles and velocity fields are compared with laboratory measurements. The numerical model successfully simulates the wave shoaling, overturning and reconnecting of free surface.

So far, few numerical simulations have been done for the interaction between the breaking wave and cylinders on a slanted slope. Since our numerical model can simulate the breaking wave on a slanted beach quite well, it is then used to simulate a plunging solitary wave impinging on a vertical cylinder at a slanted beach. The numerical results are compared with the laboratory data in terms of free surface displacements and velocity field in front of the cylinder (offshore direction). The simulations show that the numerical model successfully predicts the flow field in the region near the cylinder. Nevertheless, only two sets of wave conditions are studied due to time constraint, and more wave conditions and cylinder configurations could be explored in the future. Some important characteristics are summarized as follows:

- Due to the blockage of the cylinder, the incident wave is pushed upwards and sideways along the cylinder face, demonstrating a violent, transitional, and three dimensional flow phenomena.
- As the wave front passes through the cylinder, two water sleeves are generated at the cylinder sides. They move quickly forward and then collide with each other at the back of the cylinder. Later, the wave front separated by the cylinder reconnects itself and collapse onto the water bed.
- The run-down at the cylinder front generates secondary sleeves wrapping around the cylinder.
- The flow field at the back of the cylinder is very complex and three dimensional because of the reconnecting of free surface and the air entrainment.

- The wave force history is quite different from that of flat bottom cases. It does not present a clear trough as seen in the flat bottom cases. Instead, it shows several local extrema of force magnitude because of the complex flow field around the cylinder as the wave impinges the cylinder. Then the force smoothly decreases when the whole wave starts to run up along the beach.
- Breaking wave may cause higher wave impact force and run-up than non-breaking wave does.

6.2 Future work

The numerical model in this study has been demonstrated to be an accurate three dimensional hydrodynamic model for nonlinear wave problems. A few examples of future model extension and applications are summarized as follows:

- A higher-order upwind scheme. In this study, a first-order upwind scheme is used to discretize the advection term in N-S equations. This scheme has been proved to generate good results of free surface, velocity and pressure etc on reasonably fine mesh. However, the numerical dissipation is in suspicion of contaminating the turbulence model. To solve this problem, we can either further refine the mesh or implement a higher-order upwind scheme since it is the main source of numerical dissipation. The refinement of the mesh may not be a feasible solution because of the large geometry scales in our coastal problems and the constraints of the computational resources. Therefore, the adoption of the higher-order upwind

scheme will be an ideal solution.

- Focused breaking solitary wave and its interaction with cylinders. In this study, the solitary wave is either non-breaking (flat bottom case) or breaking behind the cylinder (beach case). H. Oumeraci et al [28, 77] found that impact force by the waves which break in front of or right at the cylinder may be quite different from that of non-breaking waves because of the duration of the impact. For instance, for the wave breaking far in front of the cylinder, the impact force history shows double peaks: first peak is due to the breaker tongue, and the second one is due to the wave front. The focused breaking wave has the advantage of accurately controlling the breaking location, and thus is widely used in the experiments.

BIBLIOGRAPHY

[1] J. B. Bell and D. L. Marcus. A second-order projection method for variable-density flows. *Journal of Computational Physics*, 101:334–348, 1992.

[2] J. B. Bell, P. Colella, and H. M. Glaz. A second-order projection method of the incompressible navier-stokes equations. *Journal of Computational Physics*, 85:257–283, 1989.

[3] S. F. Bradford. Numerical simulation of surf zone dynamics. *Journal of Waterway, Port, Coastal, and Ocean Engineering*, 126(1):1–13, 2000.

[4] W. Cabot and P. Moin. Approximate wall boundary conditions in the large-eddy simulation of high reynolds number flow. *Flow Turb. Combust.*, 63: 269–291, 2000.

[5] F. E. Camfield and S. R. L. Shoaling of solitary waves on small slopes. *Journal of Waterway, Port, Coastal, and Ocean Engineering*, 95(1):1–22, 1969.

[6] J. Charney, R. Fjortoft, and J. von Neumann. Numerical integration of the barotropic vorticity equation. *Tellus*, 2:237–254, 1950.

[7] A. J. Chorin. A numerical method for solving incompressible viscous flow problems. *Journal of Computational Physics*, 62:83–110, 1967.

[8] A. J. Chorin. Numerical solution of the navier-stokes equations. *Mathematics of Computation*, 22:745–762, 1968.

[9] E. D. Christensen and R. Deigaard. Large eddy simulation of breaking waves. *Coastal Engineering*, 42(1):53–86, Jan. 2001.

[10] R. Courant, K. Friedrichs, and H. Lewy. On the partial difference equations of mathematical physics. *IBM Journal*, pages 215–234, March 1967.

[11] B. J. Daly. Numerical study of two fluid rayleigh-taylor instability. *Phys. Fluids*, 132:346–361, 1967.

[12] R. G. Dean and R. A. Dalrymple. *Water Wave Mechanics for Engineers and Scientists*. Prentice-Hall, Inc, 1984.

[13] J. Deardorff. A numerical study of 3 dimensional turbulent channel flow at large reynolds numbers. *Journal of Fluid Mechanics*, 41:453, 1970.

[14] J. Deardorff. The use of subgrid transport equations in a third dimensional model of atmospheric turbulence. *Trans. A.S.M.E.*, 95(3):429–38, 1973.

[15] J. D. Fenton. The numerial solution of steady water wave problems. *Comput. Geosci.*, 14(3):357–368, 1988. ISSN 0098-3004.

[16] J. D. Fenton. Nonliear wave theories. In B. L. Mehaute and D. M. Hanes, editors, *Ocean Engineering Science*, pages 3–25. Wiley, New York, 1990.

[17] J. H. Ferziger and M. Peric. *Computational methods for fluid dynamics*. Springer, 1996.

[18] C. J. Galvin. Breaker type classification on three laboratory beaches. *J. Geophys. Res.*, 73:3651–3659, 1968.

[19] G. H. Golub and C. F. V. Loan. *Matrix Computations*. Johns Hopkins University Press, 1989.

[20] D. Gottlieb and S. A. Orzag. *Numerical Analysis of Spectral Methods: Theory and Applications*. SIAM, Philadelphia, 1977.

[21] S. T. Grilli, R. Subramanya, I. A. Svendsen, and J. Veeramony. Shoaling of solitary waves on plane beaches. *Journal of Waterway, Port, Coastal and Ocean Engineering*, 120(6):609–628, 1994.

[22] S. T. Grilli, R. Subramanya, I. A. Svendsen, and J. Veeramony. Shoaling of solitary waves on plane beaches. *Journal of Waterway, Port, Coastal, and Ocean Engineering*, 120(6):609–628, 1994.

[23] S. T. Grilli, I. A. Svendsen, and R. Subramanya. Breaking criterion and characteristics for solitary waves on slopes. *Journal of Waterway, Port, Coastal, and Ocean Engineering*, 123(3):102–112, 1997.

[24] R. Grimshaw. The solitary wave in water of variable depth. *Journal of Fluid Mechanics*, 46(2):611–622, 1971.

[25] P. Guyenne and S. T. Grillli. Numerical study of three-dimensional overturning waves in shallow water. *J. Fluid Mech.*, ?:?, 2006.

[26] F. H. Harlow and J. E. Welch. Numerical calculation of time-dependent viscous incompressible flow of fluid with free surface. *Phys. Fluids*, 8(12): 2182–2189, Dec. 1965.

[27] C. W. Hirt and B. D. Nichols. Volume of fluid (vof) method for the dynamics of free boundaries. *Journal of Computational Physics*, 39(1):201–225, Jan. 1981.

[28] K. Irschik, U. Sparboom, and H. Oumeraci. Breaking wave characteristics for the loading of a slender pile. In *Proceedings of the 28th International Conference on Coastal Engineering*, 2002.

[29] Y. Jaluria and K. E. Torrence. *Computational Heat Transfer*. Hemisphere, Washinton, D. C., 1986.

[30] J. Kim, P. Moin, and R. Moser. Turbulence statistics in fully developed channel flow at low reynolds number. *Journal of Fluid Mechanics*, 177:133–166, Apr. 1987.

[31] D. B. Kothe. Perspective on eulerian finite volume methods for incompressible interfacial flows. In H. C. Kuhlmann and H. J. Rath, editors, *Free surface flows*. Springer, New York, 1998.

[32] D. B. Kothe, W. J. Rider, S. J. Mosso, J. S. Brock, and J. I. Hochstein. Volume tracking of interfaces having surface tension in two and three dimensions. In *Proceedings of the 34th Aerospace Sciences Meeting and Exhibit*, 1996.

[33] D. B. Kothe, M. W. Williams, K. L. Lam, D. R. Korzekwa, and P. K. Tubesing. A second-order accurate, linearity-preserving volume tracking algorithm for free surface flows on 3-d unstructured meshes. In *In Proceedings of the 3rd ASME/JSME*, pages 99–7109, 1999.

[34] J. Larsen and H. Dancy. Open boundaries in short wave simulations – a new approach. *Coastal Engineering*, 7(3):285 – 297, 1983. ISSN 0378-3839.

[35] J. Lee, J. Skjelbreia, and F. Raichlen. Measurement velocities in solitary waves. *J. Waterway Port Coastal & Ocean Div.: Proc. ASCE*, 108(WW2):200–218, 1982.

[36] A. Leonard. Energy cascade in large-eddy simulation of turbulent flows. *Adv. in Geophys. A*, 18:237–248, 1974.

[37] C.-W. Li and P. Lin. A numerical study of three-dimensional wave interaction with a square cylinder. *Ocean Engineering*, 28(12):1545–1555, Dec. 2001.

[38] P. Lin and C. W. Li. A σ-coordinate three-dimensional numerical model for surface wave propagation. *Int. J. Numer. Meth. Fluids*, 38:1048–1068, 2002.

[39] P. Lin and P. L.-F. Liu. Numerical study of breaking waves in the surf zone. *Journal of Fluid Mechanics*, 359:239–264, Mar. 1998.

[40] P. Lin and P. L.-F. Liu. Turbulence transport, vortices dynamics, and solute mixing under plunging breaking waves in surf zone. *J. Geophys. Res.*, 103: 15677–15694, 1998.

[41] P. Lin, K.-A. Chang, and P. L.-F. Liu. Runup and rundown of solitary waves on sloping beaches. *J. Wtrwy., Port, Coast., and Oc. Engrg.*, 125(5):247–255, Sept. 1999.

[42] P. L.-F. Liu, C. E. Synolakis, and H. H. Yeh. Report on the international workshop on long-wave run-up. *Journal of Fluid Mechanics Digital Archive*, 229(-1):675–688, 1991.

[43] P. L.-F. Liu, P. Lin, K.-A. Chang, and T. Sakakiyama. Numerical modeling of wave interaction with porous structures. *J. Wtrwy., Port, Coast., and Oc. Engrg.*, 125(6):322–330, Nov. 1999.

[44] P. L.-F. Liu, T.-R. Wu, F. Raichlen, S. C. E., and J. C. Borrero. Runup and rundown generated by three-dimensional sliding masses. *Journal of Fluid Mechanics*, 536:107–144, 2005.

[45] Y. Liu, M. Xue, and D. K. P. Yue. Computations of fully nonlinear three-dimensional wave-wave and wave-body interactions. part 2. nonlinear waves and forces on a body. *J. Fluid Mech.*, 438:41–65, July 2001.

[46] Q. W. Ma, G. X. Wu, and R. E. Taylor. Finite element simulation of fully non-linear interaction between vertical cylinders and steep waves. *International Journal for Numerical Methods in Fluids*, 36:265–285, 2001.

[47] J. McCowan. On the highest wave of permanent type. *Phil. Mag.*, 39:351–359, 1894.

[48] U. Mehta. Guide to credible computer simulations of fluid flows. *AIAA Journal of Propulsion and Power*, 12(5):940–948, 1996.

[49] U. Mehta. Credible computational fluid dynamics simulations. *AIAA Journal*, 36(5):665–667, 1998.

[50] C. C. Mei, M. Stiassnie, and D. K.-P. Yue. *Theory and Applications of Ocean Surface Waves*. World Scientific Publishing, 2005.

[51] W. Mo, K. Irschik, H. Oumeraci, and P. L.-F. Liu. A 3d numerical model for computing non-breaking wave forces on slender piles. *J. Engrg. Math.*, 58: 19–30, 2007.

[52] J. Morison, M. O'Brien, J. Johnson, and S. Schaaf. The forces exerted by surface waves on piles. *J. Petroleum Technology, Petroleum Transactions, AIME*, 189:149–154, 1950.

[53] S. J. Mosso, B. K. Swartz, D. B. Kothe, and R. C. Ferrell. A parallel, volume-tracking algorithm for unstructured meshes. In *Parallel Computational Fluid Dynamics: Algorithm and Results Using Advanced Computer*, pages 368–375. Elsevier Science, 1997.

[54] B. D. Nichols and C. W. Hirt. Improved free surface boundary conditions for numerical incompressible-flow calculations. *J. Comp. Phys.*, 8:434–448, 1971.

[55] S. Osher and J. A. Sethian. Fronts propagating with curvature-dependent speed: Algorithms based on hamilton-jacobi formulation. *Journal of Computational Physics*, 79:12–49, 1988.

[56] S. Pope. *Turbulent Flows*. Cambridge University Press, Aug. 2000.

[57] S. B. Pope. Ten questions concerning the large-eddy simulation of turbulent flows. *New J. Phys.*, 6:35, 2004.

[58] W. H. Press, S. A. Teukolsky, W. T. Vetterling, and B. P. Flannery. *Numerical Recipes in Fortran*. Cambridge University Press, 1986.

[59] R. D. Richtmyer and K. W. Morton. *Difference Methods for Initial Value Problems*. Wiley-Interscience, 1967.

[60] W. J. Rider and D. B. Kothe. Reconstructing volume tracking. *Journal of Computational Physics*, 141(2):112–152, Apr. 1998.

[61] M. Rudman. A volume-tracking method for incompressible multifluid flows with large density variations. *International Journal for Numerical Methods in Fluids*, 28(2):357–378, 1998.

[62] Y. Saad. *Iterative Methods for Sparse Linear Systems*. PWS Publishing Company, 1996.

[63] Y. Saad and M. H. Schultz. Gmres: A generalized minimal residual algorithm for solving non-symetric linear systems. *J. Sci. Stat. Comput.*, 7:856, 1986.

[64] P. Sagaut. *Large Eddy Simulation for Incompressible Flows: An Introduction*. Springer, 2 edition, 2002.

[65] T. Sarpkaya and M. S. Q. Isaacson. *Mechanics of Wave Forces on Offshore Structures*. Van Nostrand Reinold, New York, 1981.

[66] M. Shashkov. *Conservative Finite-Difference Methods on General Grids*. CRC Press, 1996.

[67] J. Smagorinsky. General circulation experiments with the primitive equations: I. the basic equations. *Mon. Weather Rev.*, 91:99–164, 1963.

[68] L. M. Smith and S. L. Woodruff. Renormalization-group analysis of turbulence. *Annual Review of Fluid Mechanics*, 30(1):275–310, 1998.

[69] G. Stokes. Considerations relative to the greatest height of oscillatory irrotational waves which can be propagated without change of form. *Mathematical and Physical Papers*, 1:225–228, 1880.

[70] J. C. Strikwerda. *Finite Difference Schemes and Partial Differential Equations*. Wadswork and Brooks/Cole, 1989.

[71] S. Tadepalli and C. E. Synolakis. The run-up of n-waves on sloping beaches. *Proceedings: Mathematical and Physical Sciences*, 445:99–112, April 1994.

[72] P. Troch and J. de Rouck. Development of two-dimensional numerical wave flume for wave interaction with rubble mound breakwaters. In *Proceedings of the 26th International Conference of Coastal Engineering*, pages 1638–1649. ASCE, 1998.

[73] J. A. Turner, R. C.Ferrell, and D. B. Kothe. Jtpack90: A parallel, object-based, fortran 90 linear algebra package. In *Proceedings of the 8th SIAM Conference on Parallel Processing for Scientific Computing*, 1997.

[74] M. Vinokur. An analysis of finite-difference and finite-volume formulations of conservation laws. *Journal of Computational Physics*, 81(1):1–52, Mar. 1989.

[75] Y. Watanabe and H. Saeki. Three-dimensional large eddy simulation of breaking waves. *Coastal Engineering Journal*, 41(3–4):281–301, 1999. yasunori@eng.hokudai.ac.jp.

[76] Y. Watanabe and H. Saeki. Velocity field after wave breaking. *International Journal for Numerical Methods in Fluids*, 39(7):607–637, 2002.

[77] J. Wienke and H. Oumeraci. Breaking wave impact force on a vertical and inclined slender pile–theoretical and large-scale model investigations. *Coastal Engineering*, 52(5):435–462, May 2005.

[78] T.-R. Wu. *A numerical study of three dimensional breaking waves and turbulence effects*. PhD thesis, Cornell University, 2004.

[79] T.-R. Wu and P. L.-F. Liu. A large eddy simulation model for tsunami and runup generated by landslides. In P. L.-F. Liu, H. Yeh, and C. Synolakis, editors, *Advances in Coastal and Ocean Engineering*, volume 10. World Scientific Publishing, 2009.

[80] T.-R. Wu and P. L.-F. Liu. Numerical study on the three-dimensional dam-break bore interacting with a square cylinder. In P. Lynett, editor, *Nonlinear Wave Dynamics*. World Scientific Publishing, 2009.

[81] M. Xue, H. Xu, Y. Liu, and D. K. P. Yue. Computations of fully nonlinear three dimensional wave-wave and wave-body interaction. part 1. dynamics of steep three-dimensional waves. *J. Fluid Mech.*, 438:11–39, July 2001.

[82] V. Yakhot and S. A. Orszag. Renormalization group analysis of turbulence (i. basic theory). *J. Sci. Comp.*, 1:3–51, 1991.

[83] Q. Zhang. *A hybrid model for incompressible free-surface flows*. PhD thesis, Cornell University, 2008.

[84] Q. Zhang and P. L.-F. Liu. A new interface tracking method: the polygonal area mapping method. *J. Comput. Phys.*, 227(8):4063–4088, 2008.

[85] W. Zhang. An experimental study and a three-dimensional numerical wave basin model of solitary wave impact on a vertical cylinder. Thesis, Oregon State University, 2009.

[86] O. C. Zienkiewicz. *The Finite Element Method*. McGraw-Hill, New York, NY, 1977.